Improvements to orbit determination for cislunar space objects

Marceau Jeanjean

Delft University of Technology

TU Delft

Improvements to orbit determination for cislunar space objects

by

Marceau Jeanjean

to obtain the degree of Master of Science
at the Delft University of Technology,
to be defended publicly on Friday August 22, 2025 at 09:00 AM.

Student number:	6079431	
Project duration:	September 2024 – July 2025	
Thesis committee:	Ir. K.J. Cowan MBA,	Committee chair
	Dr. ir. D. Dirkx,	Supervisor
	Dr. S. Gehly,	External examiner
	Dr. M. Langbroek,	Additional examiner

Cover: AI generated using ChatGPT
Style: TU Delft Report Style, with modifications by Daan Zwaneveld

An electronic version of this thesis is available at http://repository.tudelft.nl/.

TU Delft

Preface

Writing this master thesis brings an end not only to my studies in Delft, but also to my life as a student in general, and I am happy to say that I do not regret going through this journey at all.

Studying Aerospace Engineering has been on my mind for almost ten years now, and I am incredibly grateful to all the people that have made it possible for me to learn all those magical things.

I would like to thank Dominic and Marco for allowing me to take a deeper dive into a real astrodynamics project, for their guidance throughout those 11 months, and for helping me see the positive when nothing was working and my concerns were growing. You made this thesis not only an assignment to complete for a degree, but an incredible learning experience for me, and I will always be thankful for that.

I also want to express my thanks to everyone that has supported me this year. My family, my friends, both in Delft and in Paris, and my roommates. Without all of you this project would have been much harder, and your company helped me a lot when my motivation was wavering.

Marceau Jeanjean
Delft, August 2025

Abstract

As several countries are once again turning their attention to the Moon, projects requiring several missions to establish long-term human presence on the Moon are being planned. In order to enable those missions in the safest way possible, this raises the need of a cislunar space situational awareness. For this purpose, the capabilities of tracking and determining the orbit of space debris have to be expanded beyond their current implementation, into the cislunar space. This context adds complexity compared to orbits located closer to Earth because of several factors, among which the highly non-linear dynamics, the format of the observations, and the need to modify the dynamical models to take more forces into account.

This research aims to build on the work described in [Witte 2024] by improving the performance of the orbit determination process. The present work has kept the focus on the Chang'e 2 and 3 lunar mission upper stages, both presenting ~10 years of optical observations including close lunar approaches. A new bootstrapping method is implemented to extend the period over which an estimation is possible to the full extent of the observation window, while reducing the number of external guesses needed to obtain those results. An indicator for the true error resulting from the orbit estimation process is then analysed to determine the behaviour of the error, and the most likely causes. The observations and residuals are then analysed and different processes are applied to investigate their effects on the quality of the orbit estimation. Those processes are adjusting the observation weights, including the ground station biases in the estimation, and filtering outlying observations. Finally, the 3-constant model is implemented in place of the cannonball model for the radiation pressure. The residuals are analysed both in-sample and out-of-sample for the different radiation pressure models, and the indicator of the true error is recomputed using this new configuration.

This leads to several interesting findings. A time offset is identified as the main cause for the error in the estimation, and the causes of this time offset can come either from the observations or from the dynamical model. The refined processing of the observations and the residuals confirms the fact that the largest uncertainty due to the observations is along the trajectory. However, the methods tried to remediate this prove to be inconclusive, indicating that the dominant effect for the error is more likely not the observation quality or processing. The implementation of a new solar radiation pressure model confirms this, by showing that the 3-constant model is able to outperform the cannonball model by all the metrics considered.

Contents

List of Figures

Nomenclature

Abbreviations

Abbreviation	Definition
CCD	Charge-Coupled Device
CROC	CROss-section of Complex bodies
DEC	Declination
DoF	Degree(s) of Freedom
DRAMA	Debris Risk And Mitigation Analysis
ESA	European Space Agency
GEO	Geostationary orbit
GPS	Global Positioning System
GVM	Gauss von Mises
GNSS	Global Navigation Satellite System
IOD	Initial Orbit Determination
IS	In Sample
ISS	International Space Station
LEO	Low Earth Orbit
LOS	Law on Space Operations
MC	Monte-Carlo
MPC	Minor Planet Center
NASA	National Aeronautics and Space Administration
NEO	Near-Earth Objects
OOS	Out of Sample
PSA	Period of Sufficient Accuracy
RA	Right Ascension
RF	Radio Frequency
RKF	Runge-Kunta-Fehlberg
RMS	Root-Mean-Square
(S)RP	(Solar) Radiation Pressure
SSA	Space Situational Awareness
SSO	Sun-Synchronous Orbit
TCM	Three-Constant Model
Tudat	TU Delft Astrodynamics Toolbox
WLS	Weighed Least-Squares

Symbols

Symbol	Definition	Unit
A	Area	[m^2]
$\mathbf{B}^{j,j+1}$	Jacobian of the jump between arcs j and $j+1$	[-]
$\mathbf{C}^{j,j+1}$	Weight matrix associated to the jump between arcs j and $j+1$	[-]
C_{nm}	Spherical harmonics coefficient of degree n and order m	[-]
C_r	Radiation pressure coefficient	[-]
$\mathbf{d}^{j,j+1}$	Jump between arcs j and $j+1$	[-]
e	Eccentricity	[-]
$\mathbf{F}$	Force	[N]
$\mathbf{h}$	Modelled observations	[rad]
$\mathbf{H}$	Jacobian	[-]
J	Cost function in the Least Squares method	[-]
k	True-to-formal error ratio	[-]
$\mathbf{L}$	Angular momentum	[kg·m^2/s^2]
m	Mass	[kg]
$\mathbf{M}$	Torque	[N·m]
$\mathbf{p}$	Momentum	[kg·m/s]
P	Power of the radiating body	[W]
P_{nm}	Legendre polynomial of degree n and order m	[-]
$\mathbf{P}$	Covariance matrix	[-]
$\mathbf{P}_0^{\text{apr}}$	A priori covariance matrix	[-]
r	Distance	[m]
$\mathbf{r}$	Position vector	[m]
$\dot{\mathbf{r}}$	Velocity vector	[m/s]
$\ddot{\mathbf{r}}$	Acceleration vector	[m/s^2]
$\hat{\mathbf{r}}$	Unit vector in the direction of $\mathbf{r}$	[-]
R_B	Radius of body B	[m]
S_{nm}	Spherical harmonics coefficient of degree n and order m	[-]
t	Time	[s]
$\mathbf{v}$	Velocity	[m/s]
$\mathbf{W}$	Weight matrix	[-]
$\mathbf{x_0}$	Initial state and parameter vector	[-]
$\mathbf{z}$	Observations vector	[rad]
α	Right ascension	[rad]
γ	Flight path angle	[rad]
δ	Declination	[rad]
θ	True anomaly	[rad]
λ	Longitude	[rad]
μ	Penalty parameter	[-]
μ_B	Gravitational parameter of body B	[m^3 / s^2]
σ	Observation weight	[-]
ϕ	Latitude	[rad]
$\mathbf{\Phi}$	State transition matrix	[-]

1

Introduction

1.1. Background and motivation

The phenomenon known as Kessler syndrome first described in [Kessler et al. 2010], depicts the scenario in which so many spacecrafts, debris and other objects are orbiting the Earth at the same time that a single collision would trigger a chain reaction that, although not instantaneous as the popular understanding of this term may deem it, could considerably increase the risk to space missions. Even with the current population, the risk is non negligible and the International Space Station (ISS) had to perform 32 collision avoidance manoeuvres between 1999 and 2022 [Cannelli et al. 2023]. This situation is getting worse as the access to space is getting cheaper [Dural et al. 2021], and as more and more actors want to launch (super) constellations of satellites, as for instance the SpaceX Starlink constellation [McDowell 2020b].

In the past years, the situation of space debris in the ”classical” Earth orbits, from LEO to GEO, has thus attracted more and more attention. In the geostationary orbit, the main issue is the fact that there is only one orbit that is rigorously geostationary. This causes the space on this specific orbit to be limited, meaning that every satellite that reaches the end of its mission should free its spot on the orbit. Moreover, the presence of debris on this orbit, or any orbit that intersects with it, would lead to dire consequences, and thus every precaution is taken to avoid having a collision between two of the GEO satellites. Such a collision would indeed lead to the creation of an immense amount of debris, as has already been seen in the case of the Iridium-Cosmos collision in LEO [Braun et al. 2017].

In the Low-Earth orbital region, there is not one single specific orbit that plays such a crucial role as the GEO orbit. Even though the sharing of a singular orbit is not an issue, some regions are subject to more interest, such as the Sun-Synchronous Orbits (SSO), and could lead to a similar situation in the future. In addition, access to LEO has been made easier over the recent years, namely with the emergence of the ”new space” sector in Europe, following the example of SpaceX in the United States [Denis et al. 2020]. This renewed interest in the aerospace sector has led to the deployment (or planned deployment) of many satellite constellations, or even mega-constellations in the case of Starlink [McDowell 2020b]. In this context, the low orbits are beginning to become very crowded, with the need for avoidance manoeuvres increasing each year [Cannelli et al. 2023]. A major cause of this problem is the fact that many satellites, despite reaching their end-of-life, have not been conceived with a decommissioning plan in mind. After the end of their mission they thus become dead weights orbiting the Earth, without any manoeuvring capability, leaving the task of preventing the collision to the active satellites they might encounter. The prevention of the collisions in this region has now become routine operation [Hobbs et al. 2019], [Bonnal et al. 2020], with a well-established process of collision detection, warning, and if need be avoidance. This process relies heavily on tracking all of the objects whose size is larger than 10 cm, and estimating their future trajectory to find the risk of a collision with other objects. This way of operating, despite being mostly successful in preventing major collisions over the past years, is not deemed to be sustainable as the number of objects and debris orbiting the Earth grows. For this reason, the international consensus has shifted towards preventing the creation

of inactive space objects (or debris) altogether. This is for instance the case in France, which has adopted the Law on Space Operations (LOS) [Achilleas 2010]. This text namely states that every satellite launched from the French territory shall have an end-of-life disposal plan to have the satellite either de-orbit, or move to a graveyard orbit in the 25 years following its end of operations. Unfortunately, this is coming late as there are already many debris orbiting the Earth.

All of this attention, studies and processes are comprised in the scope of Space Situational Awareness (SSA). This field has then logically been growing with the years [Gasparini and Miranda 2010]. Deemed the main concern for the short-term future by the ESA [ESA 2019], the efforts of SSA have been mostly focused on the Near Earth Objects (NEO), and more precisely on objects in ”crowded” or ”useful” orbits, such as the GEO or some low-earth orbits, while letting some other orbits with less spotlight.

However, the topic of space debris mitigation is now expanding beyond GEO. Indeed, lunar spaceflight, and establishing a more long-term human presence on the Moon is a major topic in the agendas of many major space agencies. The most famous program is NASA's Artemis program, aiming to install a human base on the Moon [Creech et al. 2022]. But other agencies also have their own missions planned, such as the Indian Chandrayaan missions [Goswami 2010], or the Chinese Chang'e missions [C. Li et al. 2015]. Moreover, cislunar space is also of interest in a military context [Byers and Boley 2022]. As part of those programs, multiple flights have already happened and many more are planned. These flights will go beyond the areas covered by the collision prevention process already in place. Since there are still no mitigation solution planned for safely disposing of the expendable parts of the rockets, this means that the increase in the number of flights will lead to an increase in the amount of inert objects, such as rocket upper stages. Those objects will pose a collision threat to the future lunar missions, and avoidance manoeuvres are significantly more expensive when being performed on the way to the Moon than when staying in orbit around the Earth [Barakat and Kezirian 2024]. Despite the need for an increase in cislunar SSA underlined in [Baker-McEvilly et al. 2024], not many studies have been performed on cislunar space objects.

There are multiple reasons for this, and the first is that these objects represent only a very small fraction of the space debris [Frueh et al. 2021]. Since their trajectories are highly elliptical the probability of them posing a risk to orbiting objects is extremely small. But another reason that makes their study and surveillance less common is the difficulties that are posed by such objects. Indeed, their trajectories are highly influenced by the Moon's gravitational attraction, which can lead to the trajectory considerably changing its Keplerian elements from one orbit to the next, thus rendering the term ”periodic” obsolete: the differences between one orbit and the following are too big to be considered a repetition of the same trajectory with a small variation. The Moon presence also renders the system highly non-linear, making it harder to predict what consequences a small variation of the initial conditions can have. In other words, the cislunar region is chaotic, and predictions in a chaotic environment prove to be a challenge [Frueh et al. 2021].

The collision assessment methods used for objects that are below GEO are, moreover, not adequate for the objects in the cislunar space as the force models are not taking all the relevant forces into account, and the observations used are different in the two situations. For those reasons, there is a need to investigate the process of orbit determination and propagation of debris in cislunar space, and to do it as accurately as possible to limit the number of false alarms.

Such a study has been started by [Witte 2024], which determined a generic framework, comprising the dynamical models and estimation settings best suited for orbit determination in cislunar space. There are however some issues that remain open. First, the use cases are quite limited, with only a few periods of the available data being covered. Then, the uncertainty investigation is still at a preliminary stage, using a linear propagation in a highly non-linear environment, and with an empirical process for determining the initial covariance matrix. The dynamical model can also be refined, as no alternative options to the cannonball model were considered for the solar radiation pressure. Finally, little insight has been gained on the main source(s) of error in the result of the estimation. The present work aims to improve and refine the framework developed, by identifying the source and type of the estimation errors, implementing a more accurate force model and extending the scope of the study to use more or all of the available data.

1.2. Report structure

This report is structured as follows. The background information related to the current work is presented in chapter 2. The implementation of the analyses that were conducted is described in chapter 3, and the results of those analyses are presented in chapter 4. Finally, the conclusions and recommendations that followed from the results are given in chapter 5. In addition to those chapters, some appendices are provided to elaborate on the methods and intermediate results obtained throughout this thesis. In Appendix A, additional analyses and results of the arc overlap study are provided. Then more explanation on the residuals treatment is discussed in Appendix B, and finally Appendix C details the use of the 3-constant model.

2

Background

2.1. Cislunar SSA

Although it has been seen that the need for cislunar SSA is growing, and has been acknowledged as such by several sources, the majority of the articles that investigated the topic are not providing actual concrete solutions to this issue, but rather giving standards and requirements [Barakat and Kezirian 2024], restricting their analysis to simpler cases such as periodic cislunar orbits [Wilmer et al. 2022], or studying the processes that produce debris without investigating the future of those debris [Guardabasso et al. 2023]. Since the trajectories to reach the Moon can not be designed to avoid all the cases that are not comprised in the existing literature, there is a knowledge gap when it comes to estimating and propagating the trajectory of non-special objects in the cislunar region, and this with a high accuracy that allows the classical collision detection and prevention processes to be applied to future cislunar missions. [Witte 2024] has started to study this gap, and the present study aims at further improving the general framework that was developed.

It is also important to note that one of the major difference with traditional LEO objects is the difficulty and the type of the measurements. Indeed, for an object in LEO it is theoretically possible, with enough ground stations (and funds to operate them) to have a full coverage of the orbit of a spacecraft, using for instance radar measurements that are not impacted by the day-night cycle. However, such measurements require to be close to the target and become less relevant as the object is further away from Earth, already being almost completely unused in GEO [Guo et al. 2010]. Because of that the only source of measurements possible for cislunar debris is optical measurements. Such a means of obtaining information is less convenient because it is heavily dependent on the weather conditions, the day-night cycle and the presence of a bright object (e.g. the Moon) in the background. As such, even with as many ground stations and observation quality as possible, the observations by themselves would still not provide an unambiguous position, and therefore trajectory, of the space object. The only way to obtain them is to make use of the dynamics of the system, finding the trajectory that matches best with the observations. This requires the development and verification of an accurate physical modelling of the environment in order to be able to precisely match the measurements and to subsequently predict the movement as close to the reality as possible.

2.2. Dynamical modelling

In this section, the fundamental equations describing the dynamics of the system are first introduced. Then, the mathematical expressions for the different forces taken into account in this study are presented, and finally the equations for the rotational dynamics are shown, along with a discussion about their relevance to this work.

2.2.1. Overview

As previously stated, the need for prediction of the movement of the objects in the cislunar space creates the need for an adequate physical modelling of the environment. Indeed, the movement of a

space object (or of any physical object in the classical mechanics description), is entirely decided by the set of forces that are acting upon it. The choice that has to be made for an adequate modelling of the trajectory is therefore which forces to include in the model, and which formulation to use (when multiple formulations exist).

First of all, the mathematical expression describing the motion of an object in an inertial frame at time t is [Wakker 2015]:

$$\sum_i \mathbf{F}_i(t) = \frac{\mathrm{d}\mathbf{p}}{\mathrm{d}t}(t) \tag{2.1}$$

Here, $\mathbf{F}_i$ is the i-th force acting on the object, and $\mathbf{p}$ is the momentum of the object, defined as the product of the mass m and the velocity $\mathbf{v}$:

$$\mathbf{p}(t) = m(t)\mathbf{v}(t) \tag{2.2}$$

If the mass of the object considered is constant (e.g. a space debris, or a satellite without a propulsion system), the mass can be taken out of the derivative and Equation 2.1 becomes:

$$\sum_i \mathbf{F}_i(t) = m\frac{\mathrm{d}\mathbf{v}}{\mathrm{d}t}(t) = m\frac{\mathrm{d}^2\mathbf{r}}{\mathrm{d}t^2}(t) \tag{2.3}$$

From this equation the movement of the object can be integrated knowing only its initial state (position and velocity) and the expressions of the forces acting upon it. Moreover, this equation allows to write the acceleration of the object studied as:

$$\ddot{\mathbf{r}}(t) = \frac{\mathrm{d}^2\mathbf{r}}{\mathrm{d}t^2}(t) = \frac{1}{m}\sum_i \mathbf{F}_i(t) = \sum_i \frac{\mathbf{F}_i(t)}{m} \tag{2.4}$$

Based on this way of writing the equation of motion, the forces applied to the object are referred to as ”accelerations”, and they are formally defined as

$$\ddot{\mathbf{r}}_i(t) = \frac{\mathbf{F}_i(t)}{m} \tag{2.5}$$

As stated above, Equation 2.1 is only valid for reference frames with an inertial origin and orientation and classical (Newtonian) mechanics. This means that if the frame used is not inertial, some additional forces must be added in Equation 2.3 to take the movement of the frame into account [Montenbruck and Gill 2013]. A different way to account for the movement of the frame (but mathematically equivalent) is to modify the expression of the accelerations to include the effect of some accelerations on the origin of the (non-inertial) frame. For instance, considering three bodies:

- Body A is the body undergoing the acceleration
- Body B is the body exerting the acceleration
- Body C is the body to which the origin of the reference frame is tied

In this case, the expression of the acceleration of A with respect to C, denoted $\ddot{\mathbf{r}}_{A/C}$ is given by:

$$\ddot{\mathbf{r}}_{A/C} = \ddot{\mathbf{r}}_A - \ddot{\mathbf{r}}_C = \frac{\mathbf{F}_{B/A}}{m_A} - \frac{\mathbf{F}_{B/C}}{m_C} \tag{2.6}$$

Where $\ddot{\mathbf{r}}_A$ (resp. $\ddot{\mathbf{r}}_C$) is the inertial acceleration of body A (resp. C), $\mathbf{F}_{B/A}$ (resp. $\mathbf{F}_{B/A}$) is the force exerted by body B on body A (resp. C) and m_A (resp. m_C) is the mass of body A (resp. C). In the following, the acceleration expressions will be given in the inertial frame, and the correction for the non-inertial frame are handled by the propagation software Tudat (presented in section 3.1).

In this study, the preferred reference frame will be a frame whose orientation is considered inertial as it is defined by the position of distant stars whose movement is negligible over the time scales of this study [Wakker 2015]. The origin of the reference frame, however, is going to be the centre of mass of the Earth, which can not be considered inertial as it is moving through the solar system in a trajectory

that is not a straight line, and this motion is happening on the same time scale as the phenomenon studied. Therefore, when computing the accelerations of the various forces on the space objects it will be important to keep in mind that some of the forces also apply on the origin of the reference frame.

The main forces that are of interest in the cislunar space are the gravitational forces, especially the ones exerted by the Earth, Moon and Sun [Baker-McEvilly et al. 2024]. The most basic expression of the gravitational force exerted by a body B is the point-mass gravity. in this model, the acceleration $\ddot{\mathbf{r}}_{B,pm}$ can be written as [Wakker 2015]:

$$\ddot{\mathbf{r}}_{B,pm} = -\frac{\mu_B}{r^3}\mathbf{r} \tag{2.7}$$

Where μ_B is the gravitational parameter of body B, $\mathbf{r}$ is the vector going from body B to the object undergoing the acceleration, and r is the norm of $\mathbf{r}$. This expression makes the assumption that all the mass of the body is concentrated in one point (its centre of mass), and thus neglects the mass distribution. It is used for forces (also called perturbations) that have a small magnitude compared to the other forces in play, and for cases where the exerting body is far enough from the object that the specific distribution of its mass is not significant.

In case the massive body is both close and exerts a strong force (e.g. the Earth), then the point-mass assumption can become insufficiently accurate and the need arises to take into account the mass distribution of the body. To this end, the gravitational force is computed as the gradient of the gravitational potential created by the massive body, thus leading to the expression [Montenbruck and Gill 2013]:

$$\ddot{\mathbf{r}}_{B,sh} = \nabla\left(\frac{\mu_B}{r}\sum_{n=0}^{\infty}\sum_{m=0}^{n}\frac{R_B^n}{r^n}P_{nm}(\sin(\phi))\left(C_{nm}\cos(m\lambda)+S_{nm}\sin(m\lambda)\right)\right) \tag{2.8}$$

Here, $\ddot{\mathbf{r}}_{B,sh}$ is the gravitational acceleration exerted by body B, R_B is the radius of body B, P_{nm} is the Legendre polynomial of degree n and order m, C_{nm} and Snm are the spherical harmonics coefficients of degree n and order m, ϕ is the geocentric latitude and λ the geocentric longitude. The first noticeable thing is that this equation contains an infinite number of terms, making it highly impractical for real uses. However, since the coefficients P_{nm}, C_{nm} and S_{nm} are decreasing with n and due to the fact that this expression is only valid for $r > R_B$, the terms of the sum become smaller as n increases, thus allowing for a simplification by truncating the sum to a certain n (the degree) and a certain m (the order).

The second thing to notice, that applies to both this formulation and the point-mass approximation given in Equation 2.7 is that those accelerations do not depend on the mass of the object undergoing the acceleration, meaning that those forces will have a similar influence on the origin of the frame and on the object. The second term in Equation 2.6 can therefore not be neglected for gravitational accelerations.

The last gravitational correction that can be taken into account is the time variation of the gravitational field of the main attracting body, i.e. the oceanic and solid tides of the Earth. Under those effects, the spherical harmonics coefficients used in Equation 2.8 are no longer constant but their values are changing in time. Their expression can be found in [Montenbruck and Gill 2013], but they are not expected to be relevant in this study.

Although gravitational forces are the main contributors to the movement of the space object, some other forces are to be considered. This is namely the case for the radiation pressure and the atmospheric drag. First, the atmospheric drag is expected to be almost always negligible, as the orbits considered in this study are highly elliptical and do not typically come close enough to the Earth to enter the atmosphere (2000 km) [Celletti et al. 2017]. Therefore, it is found that the atmospheric drag can be neglected in this study.

As for the Solar Radiation Pressure (SRP), since its role is much more relevant it requires a more in-depth study, that is developed in subsection 2.2.2.

2.2.2. Solar radiation pressure

The radiation pressure is the force applied to any object that receives light, as the photons impacting the object carry some momentum that is then transferred to the object. Although each individual photon

has a very small momentum, the effect can add up to significant amounts over time [Casanova et al. 2015]. In the case of a space object, the major cause of this effect is the Sun, and the force that comes from it is called the Solar Radiation Pressure (SRP). Other bodies can also exert a radiation pressure on the object, such as the Moon or the Earth. However, those effects have a significantly lower amplitude than the SRP as discussed in [Stiller 2023] and [Montenbruck and Gill 2013], and are not considered in this study.

Given the importance of the SRP for the trajectories studied in this work, a specific study has been conducted to investigate the best mean to model it. Indeed, whereas gravitational accelerations have an exact expression whose coefficients only depend on the exerting body, the SRP requires knowledge of many parameters that are specific to the object being under investigation. Moreover, a fully accurate expression would have to include a perfect simulation of the surface of the space object in order to compute the angle of incidence of each photon, along with a perfectly accurate reflection law. This is already very computationally expensive even in the ideal case where the object is perfectly characterised, and gets even more complex in most use cases where the object is an unknown space debris whose parameters can at best be estimated [Jah and Madler 2007]. For those reasons, there is a need for a simplified approach to this force.

The two most commonly used methods are the cannonball method, and a panelled radiation method. In the cannonball model, the space object is represented by a perfect sphere, with a fixed radius and a known reflectivity parameter. Due to the spherical symmetry of the sphere and the fact that the solar flux is constant over the dimensions of the spacecraft, the need for the computation of each individual photon disappears and the force will always result in a component aligned with the Sun-object direction, pointing away from the star. This description is very easy to compute, requiring only the direction of the Sun and the two parameters (sphere radius and reflectivity coefficient) of the space object. The resulting expression for the acceleration $\ddot{\mathbf{r}}_{SRP}$ is [McMahon and Scheeres 2015]:

$$\ddot{\mathbf{r}}_{SRP} = C_r \frac{P}{4\pi r^2} \frac{A}{m} \hat{\mathbf{r}}_{S,o} \tag{2.9}$$

With C_r being the dimensionless radiation pressure coefficient comprised between 1 and 2, P the solar radiation constant, equal to 1×10^{17} kg·m/s^2, r the distance between the two objects, A the projected area of the sphere, m the mass of the object, and $\hat{\mathbf{r}}_{S,o}$ the unit vector going from the Sun to the object.

Here, the order of magnitude of the acceleration is decreasing as the inverse of the radius of the object, due to the $\frac{A}{m}$ term. This means that for larger objects such as the Earth, the acceleration due to the SRP is considerably lower than for the spacecraft and thus this acceleration is not considered to have an influence on the motion of the origin of the reference frame. The $\frac{\mathbf{F}_{B/C}}{m_C}$ term in Equation 2.6 is thus ignored for this acceleration.

The cannonball expression is a rough estimate of the force and is not able to predict accurately the long-term dynamics of the space object. The specific inaccuracies encountered in the cislunar space are presented in [Witte 2024]. Namely, the fact that the objects are tumbling and not perfectly facing the Sun may cause some effects in a direction slightly different from the Sun-object line. The cannonball expression is not able to model those effects and thus it can lead to errors and absurd values such as a $C_r > 2$.

A panelled radiation method on the other hand takes as an input a model of the space object which consists of different panels that can each have their own reflectivity coefficient. The force is then computed by computing the force on each panel and then summing them together, as described in [Stiller 2023]. Such a method allows to have a more accurate description of the force, leading to better results in the propagation. However, in order to know the orientation of the force the orientation of each panel must be known. This in turn raises the need for a detailed model of the object, which is not always available; and the need for the orientation of the spacecraft. This orientation is also typically very difficult to obtain, as is explained in subsection 2.2.3.

In order to provide an accurate estimation of the force without requiring more information than is possible to acquire, an intermediate solution is investigated. The chosen method is the Three-Constant Model (TCM) that is depicted in [McMahon and Scheeres 2015]. In order to express the new acceleration, three base vectors $\hat{\mathbf{u}}, \hat{\mathbf{v}}, \hat{\mathbf{w}}$ are first defined as follows:

$$\hat{\mathbf{u}} = -\frac{\mathbf{R}_E}{R_E} \tag{2.10}$$

$$\hat{\mathbf{w}} = \cos(\phi)\hat{\mathbf{Z}}_I - \sin(\phi)\left(\hat{\mathbf{Z}}_I \times \hat{\mathbf{u}}\right) \tag{2.11}$$

$$\hat{\mathbf{v}} = \hat{\mathbf{w}} \times \hat{\mathbf{u}} \tag{2.12}$$

Where $\mathbf{R}_E$ is the Earth position vector relative to the Sun and R_E its magnitude, ϕ the obliquity of the spin axis of the Earth (taken as 23.4° in this study), and $\hat{\mathbf{Z}}_I$ is the unit vector in the direction of the Earth's heliocentric orbit angular momentum vector.

The expression for the acceleration is then:

$$\ddot{\mathbf{r}}_{SRP} = \frac{P}{mr^2}\left(A_1\hat{\mathbf{u}} + A_2\hat{\mathbf{v}} + A_3\hat{\mathbf{w}}\right) \tag{2.13}$$

With P, m and r representing the same quantities as in the cannonball model. A_1, A_2 and A_3 are the three coefficients that replace C_r. They are expressed in m^2 and it can be noticed that the TCM can be used to "simulate" the cannonball model by taking $A_1 = -C_r A$ and $A_2 = A_3 = 0$. Note the negative sign, due to the fact $\hat{\mathbf{u}}$ is pointing towards the Sun, as opposed to $\hat{\mathbf{r}}_{S,o}$

In this model, the force applied on the object is allowed to have three components, expressed in a rotating frame tied to the Earth's heliocentric orbit. As such, it requires two additional parameters to estimate, but the orientation of the object is not needed. This seems to indicate a promising possibility of balancing the number of parameters that have to be known or estimated, and the level of accuracy that is possible to achieve in the results. Such a model could improve the accuracy of the orbit determination process because it is able to capture some effects that are not exclusively in the direction from the Sun to the space object. Those effects, although non-negligible as [Witte 2024] discussed, are expected to be less important than the in-line acceleration, and thus it is expected that the values for A_2 and A_3 will be lower than the value for A_1.

2.2.3. Rotational motion

In addition to the motion of the centre of gravity that is described by Equation 2.1, the attitude of the space object is also described by a similar equations, with forces being replaced by torques $\mathbf{M}_i$ and momentum by angular momentum $\mathbf{L}$ [Montenbruck and Gill 2013]:

$$\sum_i \mathbf{M}_i(t) = \frac{\mathrm{d}\mathbf{L}}{\mathrm{d}t}(t) \tag{2.14}$$

Using this equation and simulating the evolution of the rotational state of the object could lead to a better model, especially for forces that depend on the orientation of the object, e.g. the SRP (for some expressions of this force).

The numerical simulation of rotational dynamics, however, requires much more effort and time to reach results of a comparable accuracy. The first reason of this is the format of the observations. Indeed, for objects that are far away from the Earth, e.g. the ones in cislunar space, the most common measurements are simply a pair of angles: the right ascension (RA) and declination (DEC), as shown in Figure 2.1. They are, additionally, obtained from optical detection [Frueh et al. 2021]. In such measurements, the object appears as a dot (or a spot) on the detector, and the level of precision does not allow for specific identification of the orientation of the object. The best information that can be obtained is gained through the variation of the brightness of the object, and it only relates to the tumbling rate rather than the absolute orientation. Unfortunately, even such a brightness curve cannot allow to properly measure the tumbling rate, because depending on the shape of the object, different tumbling rates could yield the same brightness curve [Balster et al. 2023].

The second reason that explains the difficulty to run a full 6-Degrees of Freedom (6DoF) simulation is the need for a complete characterisation of the space object under study. Indeed, its angular momentum needs to be known around the three axes, but also its specific shape is required in order to know how the forces are spread and to compute the value of the various torques. Such information is hard to

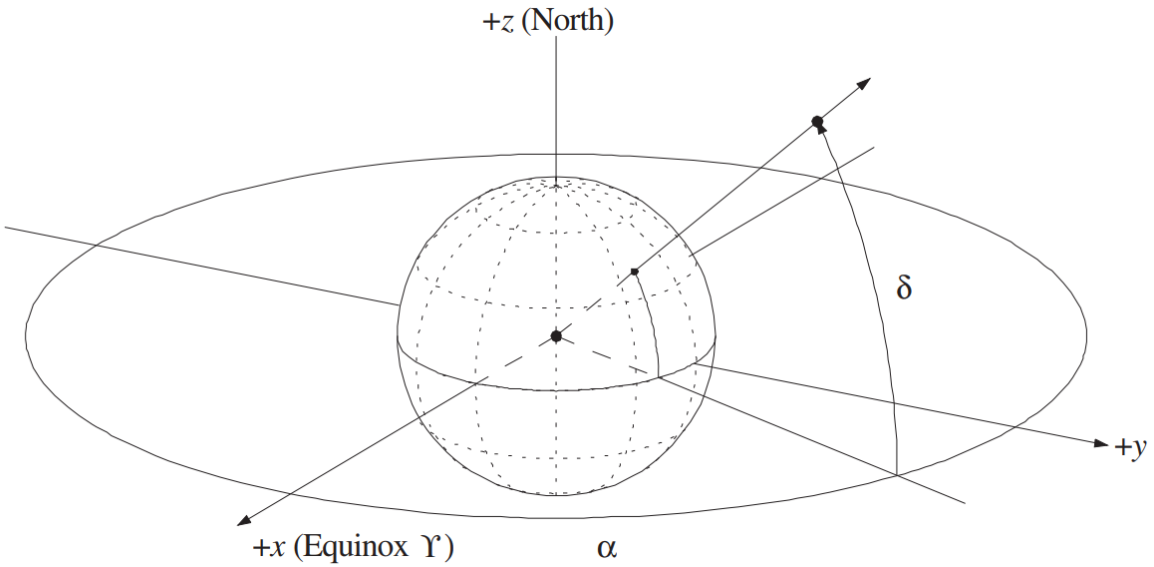

Figure 2.1: Right ascension (α) and declination (δ) [Montenbruck and Gill 2013]

come by because of the confidentiality of the companies or agencies that develop space equipment, but can also be completely impossible to obtain, for instance in the case of space debris resulting from a collision. In such a situation, the fragments can be too far from Earth to be properly imaged and characterised. Finally, even if the object is perfectly known, in some circumstances it can prove too difficult to completely model, as is the case for the upper stage of rockets with remaining fuel: in order to be accurate, a simulation could need to simulate the sloshing, which requires an extended fluid dynamics model and would considerably increase the runtime.

Indeed, the runtime of individual propagations is an additional concern even if enough information was known to run the adequate simulations. This is important because in order to perform a trajectory estimation, the software requires a large numbers of those propagations to be ran, and therefore reducing the computing time of an individual simulation can lead to significant improvements of the software's efficiency. However, running a simulation with 6 degrees of freedom is considerably longer than one with only 3 degrees of freedom, and can lead to practical problems when applied to real life situations.

Due to these three reasons, the rotational dynamics are neglected in this study, and the object is considered to be represented by its centre of mass.

2.3. Orbit determination

In this section, the data used in this study is first presented. Then, the orbit determination itself is introduced, both the general method and the multi-arc method. Finally, the numerical integration process that allows to apply those methods is described.

2.3.1. Data

The objects considered in this study are the upper stages of the Chang'e 2 and Chang'e 3 rockets (identified respectively by the codes 2010-050B and 2013-070B). Those rockets were launched in the context of the Chinese Lunar Exploration Program [Xu and Ouyang 2014], and their upper stages have orbited the Earth in cislunar space for an extended period of time. Those objects are the same that were used in the analysis conducted in [Witte 2024], where their mass and maximum surface area had been estimated to be respectively 5000kg and 37.14m^2.

It has been found using the Cross-section of complex bodies (CROC) tool from the ESA Debris Risk And Mitigation Analysis (DRAMA) software that the maximal cross-section was 37.906m^2 instead. In addition to this, the two models used for the SRP are based on the assumption that the objects are tumbling [McMahon and Scheeres 2015], and thus the average cross-section is deemed more relevant.

Its value is found to be 32.57m^2. Finally, no sources were found for the dry mass of 5000kg given in [Witte 2024], but [McDowell 2020a] gives an estimated value of 2800kg. Those values only impact the estimation process through the $\frac{A}{m}$ ratio in the expression of the cannonball model, and the $\frac{1}{m}$ fraction in the TCM. Therefore, in order to allow for a better comparison to the results of [Witte 2024], the values of 37.14m^2 and 5000kg are used. The impact of using potentially wrong estimates is discussed in section 4.4

The observation data for those objects was collected by the Minor Planet Center (MPC) and can be found through the Project Pluto databases. Observations for the upper stage from the Chang'e 2 mission span from the launch year 2010 until 2021 when the object left the Earth orbit. As for the Chang'e 3 upper stage, the data is available from its launch in 2013 until today, but the post-processing of the raw data has been done specifically for [Witte 2024] until the 31/12/2023, and thus the observations taken later than this date have not been included in the present study. The data points are coming from 52 different observatories, with 36 of them providing data for the Chang'e 2 upper stage, and 34 for the Chang'e 3 upper stage. There are 1560 (resp. 881) observations in the time interval considered for the Chang'e 2 (resp. Chang'e 3) upper stage.

Moreover, the Find_Orb software [Gray 2022] has been used for external inputs (initial guesses) in the orbit determination process. This software performs Initial Orbit Determination (IOD), and provides a rough estimate for the trajectory.

The acquisition method for the observations used in this study is optical imaging through the use of Charge-Coupled Devices (CCD) cameras [Klinkrad 2006]. The observations are performed in the inertially staring mode, which means that the stars in the background are fixed and the object appears as a streak of light on this background. The observations are then stored in the MPC format, which comprises the right ascension and the declination in the topocentric J2000 reference frame. In addition to this data, the observation includes the time of the observation, along with other information such as the ground station code (needed to know the location of the ground station).

An important aspect of the observations that needs to be taken into account is the errors that affect them, and their various sources. Those errors can typically be sorted in three different categories as discussed below [Kjeldsen and Frandsen 1992]

- **Random errors**: Those are the same errors that are present in every kind of physical measurement. They are by default assumed to follow a Gaussian distribution.
- **Observation biases**: Due to using a specific instrument in specific conditions, a bias is always introduced in the observation data. The causes for this bias can be various, and include resolution effects, inaccurate or outdated star catalog etc.
- **Timing errors**: As the time of the observation is also registered, any error on the time will impact the data. The effects of a timing error are different from an observation bias because they vary with the characteristics of the object observed. Indeed, an error of 1s will represent a larger difference in angular position if the object is closer to periapsis (where its angular velocity is the largest) than if it is at apoapsis.

In the context of CCD right ascension/declination observations, one particular source of timing error is important to mention: the streak effect. An example of an optical observation can be found in Figure 2.2.

On this image, a stack of 15 optical observations in a row can be seen. For each of those observations, a pair (α, δ) was acquired, along with the time of the observation. Each of the observations thus corresponds to a spot on the picture, and the spots are not restricted to a single point (or pixel) on the detector. One single observation thus consists of a small streak on the detector, and in order to return a singular value for the right ascension and declination the middle of this streak is taken as the observation. This can, however, lead to an issue when the object is tumbling. This is the case of the Chang'e 3 upper stage, and that is why its luminosity is varying along the observation time. The problem that can arise is that along this rotation there is an angle in which the light reflected is not intense enough to be distinguished from the background. When the transition from not visible to visible happens in the middle of the exposure time, this leads to an error in the observation time.

For example, in the simple situation where the exposure time is one second and the observation is

Figure 2.2: Stack of 15 images taken with the 0.51-m telescope of MPC Q65 Warrumbungle, Australia, on 11 September 2015. Note the the slow brightness variation with periodic specular peaks in brightness. Image courtesy M. Langbroek

performed from $t_i = 0.0s$ to $t_f = 1.0s$. If the object is visible throughout the entirety of the exposure time, then the spot will represent its path from t_i to t_f, and taking the middle point of the streak (or spot) will yield the position at $t_1 = \frac{t_i+t_f}{2} = 0.5s$. In this situation, attributing the observation to the time t_1 is therefore correct, and there is no error introduced.
If the object is tumbling and was not visible during the first half of the exposure time the situation is very different. Indeed, the streak will represent its path from t_1 to t_f, and taking the middle point will thus give the position at $t_2 = \frac{t_1+t_f}{2} = 0.75s$. This time, attributing the observation to the time t_1 is not correct and results in an error of $0.25s$. This error is much harder to correct than the light-time effect, mainly because detecting when it happens is not easy, and its effects, while mostly time-related, are not necessarily restricted to the along-track direction. Moreover, the magnitude of this effect is random and cannot be determined simply from those observations.

2.3.2. General orbit determination

The process of orbit determination is aimed at two main objectives: the first is to be able to know the position of the object under investigation during the period of observation; and the second is to be able to predict its motion in the future, for instance in order to predict potential collisions. In cases where it is relevant, in addition to the position, estimating the parameters influencing the dynamics of the object is also part of the first goal.

Although it is clear why a dynamical simulation is necessary in the second case, the position determination also requires such a simulation. Indeed, for objects in cislunar space, there was no way to obtain the position of the object through the available measurements. This argument is no longer true for objects between LEO and GEO, mainly because with the addition of a GPS receiver the position of a satellite can be obtained very rapidly and accurately. However, the Global Navigation Satellite System (GNSS) networks do not reach far enough in the cislunar space and although concepts have been elaborated for a cislunar GNSS constellation, none is currently under investigation, let alone already flying. In addition to this limitation, GNSS positioning can only be used by active satellite, whereas the current study also aims at determining the orbit of space debris that are by definition passive objects and cannot communicate with GNSS satellites.

Therefore, since the only measurements available do not give a position, but constraints about the position, the most common way of estimating the position is to make use of the other information that is known. This complementary information takes the form of the dynamics of the system. Indeed, even though a series of observations points could correspond to an infinite number of successive positions, there usually is at most one of those that complies with the equations of motion described in section 2.2. Using this information thus allows to eliminate everything that is dynamically impossible and find the

trajectory of the space object.

In addition to the above, it should be mentioned that every measurement is affected by errors and uncertainties, which often lead to the result that no trajectory is a perfect fit for every observation, and therefore a metric has to be computed to evaluate how well a given trajectory explains the observations, and the ”real” trajectory is the one that gives the best result for this metric.

There are different possibilities to evaluate the fit, but the most common one when all the data is already available (i.e. the orbit is determined a posteriori and not on the fly) is to use the Least-Squares method. In this method a trajectory is defined by a set of parameters $\mathbf{x_0}$ typically containing the initial state, but it can also include some other values, such as the reflectivity or the drag coefficients. The trajectory is computed using a dynamical model and then its ”score” is evaluated by simulating the measurements that were performed. The differences between the actual measurements and the simulated ones are called the residuals, and the computed metric is the sum of the squares of the residuals. The objective is to minimise this metric, as lower residuals mean that the trajectory gives observations closer to the actual ones. This is the base principle of the Least-Squares method, which can then be adapted to take into account the different accuracies of the measurements, by introducing a weighting matrix $\mathbf{W}$, thus giving the Weighted Least-Squares (WLS) method. In this method, the error to minimise $J(\mathbf{x_0})$ is given by [Montenbruck and Gill 2013]:

$$J(\mathbf{x_0}) = (\mathbf{z} - \mathbf{h}(\mathbf{x_0}))^T \mathbf{W} (\mathbf{z} - \mathbf{h}(\mathbf{x_0})) \tag{2.15}$$

Where $\mathbf{z}$ are the observations, $\mathbf{h}(\mathbf{x_0})$ are the observations simulated when using $\mathbf{x_0}$ as a set of parameter. It is then possible to linearise this expression, and find the correction $\Delta\mathbf{x_0}^{\text{lsq}}$ that leads to a minimum for J:

$$\Delta\mathbf{x_0}^{\text{lsq}} = (\mathbf{H}^T\mathbf{W}\mathbf{H})^{-1}\mathbf{H}^T\mathbf{W}\Delta\mathbf{z} \tag{2.16}$$

Where $\mathbf{H} = \frac{\partial \mathbf{h}}{\partial \mathbf{x_0}}$

Using this equation, it is thus possible through an iterative process to find successive sets of parameters that give lower residuals, until an ending criterion is reached. Such a criterion is usually chosen to be that the results improve less than a chosen threshold between two iterations, but it could also be that the ”score” of a set of parameters is lower than a certain value.

It is important to note that due to the linearisation step, an initial guess that is too far from the truth will lead to a potentially non-converging process, thus failing to give a resulting trajectory. The initial guess should therefore be as accurate as possible. This initial guess does not however bear any weight in the orbit determination process as described above. Therefore, in addition to using weights to favour observations that are more accurate, it is possible to add an a priori covariance matrix that penalises large deviations from the initial guess. This is useful when the initial guess can be trusted to be a good indicator and should not be discarded altogether.

Another phenomenon, over-fitting the data, can also be prevented using this a priori covariance matrix. Indeed, if the software has a lot of parameters to adjust, it is sometimes possible to find a set of parameters that fit the data very well, but when matched with observations outside the training dataset lead to highly inaccurate results. A very simplified example of over-fitting can be seen in Figure 2.3. Here, the data consists of 5 data points taken as $y = x$, with some random noise added. When using the linear fit, the proper behaviour is estimated and the predictions made by the model outside of the training set would be correct. When using 5 coefficients for the fitting polynomial expression the fit is much better on the training set, as it passes exactly through the points. Outside the range of the data however, the 4th order fit diverges very quickly and would give worse predictions than the linear model. In this example, over-fitting is caused by using too many parameters compared to the real behaviour of the data.

In the context of orbit determination, over-fitting can happen even when using only parameters that are relevant to the real behaviour of the data. The issue is then caused by a lack of data, and thus the estimator finds a solution that allows for a better in-sample fit, by changing the values of the parameters to absurd values. The a priori covariance matrix, by forcing the parameters to remain in the

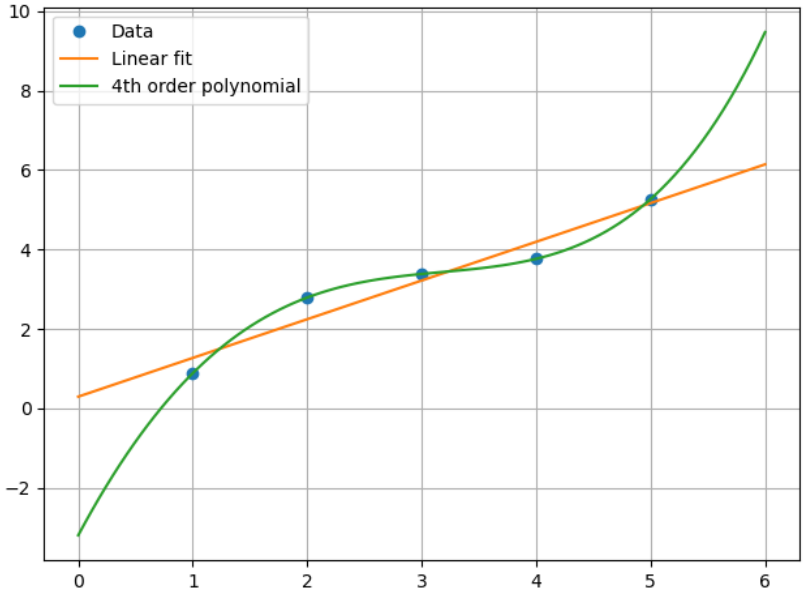

Figure 2.3: Over-fitting example

neighbourhood of the initial guess, mitigates this issue. When using an a priori covariance matrix $\mathbf{P}_0^{\text{apr}}$, the expression for $\Delta\mathbf{x_0}^{\text{lsq}}$ becomes:

$$\Delta\mathbf{x_0}^{\text{lsq}} = ((\mathbf{P}_0^{\text{apr}})^{-1} + \mathbf{H}^T\mathbf{W}\mathbf{H})^{-1}((\mathbf{P}_0^{\text{apr}})^{-1}\Delta\mathbf{x_0}^{\text{apr}} + \mathbf{H}^T\mathbf{W}\Delta\mathbf{z}) \tag{2.17}$$

2.3.3. Multi-arc orbit determination

Generic

When performing an orbit determination over long periods of time, the imperfections of the dynamical model make it harder to converge to a trajectory that fits the observation data. Moreover, the matrices involved in the process become larger, which in turn leads to increased computational loads [Godard et al. 2017]. Therefore, estimating all of the observations as a whole can become inefficient. An alternative solution is to estimate the trajectory of the space object by arcs.

In such a method, the observations dataset is divided into a number of arcs. The length of the arcs needs to be long enough to include enough data, but not too long to run into the issues described above [Godard et al. 2017]. Once such a division has been performed, the estimation algorithm is run on each arc separately and the results are in the form of a set of parameters (initial state + potential complementary parameters) for each arc, and the final state of one arc can be used as an initial guess for the next arc. This method allows for a better fit to the data and a faster computation time. The main downside to this is that the trajectory no longer follows the dynamical equations, as there is the possibility that discontinuities are present in between the arcs. For this reason, the prediction of the future behaviour can be made more difficult. The choice of which state to use as a reference is quite straightforward: the one at the last epoch is the best option. The question of which value to select for the other parameters is however more tricky. Indeed, if the cannonball model is used for SRP, the reflectivity coefficient C_r is not usually known, and thus is one of the estimated parameters. As such, it can have different estimated values across the successive arcs. However, the value of C_r is not supposed to change and there is no specific reason that the last value would be more accurate than the previous ones.

One way to mitigate this issue is to implement some so-called ”global” parameters [Parisi et al. 2012]. Such parameters are set to have the same value in all the arcs. With this type of parameters, there is more control over which parameters are allowed to exhibit discontinuities between the arcs and which ones should remain fixed.

Constrained

In order to limit the size of the ”jumps” in position between two successive arcs, it is possible to implement a constrained version of the multi-arc orbit determination method. Such an implementation has been described in [Lari and Milani 2019], in the context of the JUICE mission. In such a method, an additional term is added to the loss function so that it becomes:

$$J(\mathbf{x_0}) = (\mathbf{z} - \mathbf{h}(\mathbf{x_0}))^T \mathbf{W} (\mathbf{z} - \mathbf{h}(\mathbf{x_0})) + \frac{1}{\mu} \sum_{j=1}^{n-1} \mathbf{d}^{j,j+1} \cdot \mathbf{C}^{j,j+1} \mathbf{d}^{j,j+1} \tag{2.18}$$

with μ the penalty parameter, that allows to adjust how to balance between the observations and the jumps, $\mathbf{d}^{j,j+1}$ the state difference between arcs j and $j+1$, and $\mathbf{C}^{j,j+1}$ the weighting matrix for the jumps.

With this new expression, after linearisation and derivation to find the minimum, it is possible to find:

$$\Delta \mathbf{x_0}^{\text{lsq}} = (\mathbf{H}^T \mathbf{W} \mathbf{H})^{-1} \mathbf{H}^T \mathbf{W} \Delta \mathbf{z} - \frac{1}{\mu} (\mathbf{H}^T \mathbf{W} \mathbf{H})^{-1} \sum_{j=1}^{n-1} \mathbf{B}^{j,j+1} \mathbf{C}^{j,j+1} \mathbf{d}^{j,j+1} \tag{2.19}$$

Where $\mathbf{B}^{j,j+1} = \frac{\partial \mathbf{d}^{j,j+1}}{\partial \mathbf{x_0}}$

In order to compute the $\mathbf{B}^{j,j+1}$ matrices, the process should be very similar to computing the state transition matrix that is already used to compute the $\mathbf{H}$ matrix. Indeed, the values can be easily initialised, by observing that a variation of the initial state affects the discrepancy at the initial position if and only if this variation is on one of the position or velocity parameters. The propagation then obeys some differential equations that can be solved for each integration step.

However, due to the internal functioning of Tudat (presented later in section 3.1), it is possible that such an addition would prove very difficult to implement, and could cost a lot of time. Therefore three options are considered. The first one is to use Tudat to propagate the differential equations and use the formula for the iteration step as written above; the second option is to compute $\mathbf{B}^{j,j+1}$ using finite differences and then use the formula for the iteration step; the third option is to consider the problem as a constrained optimisation problem and use a standard algorithm for finding the minimum. The second option is much easier to implement but requires additional propagation compared to the first one, leading to an increase in the computer time required. The third option is less predictable, because depending on the algorithm and the situation, it could lead to more evaluations than the iterative step described by the formula. The second option is then the one deemed more suitable for a first approach.

2.3.4. Numerical integration

In order to perform the orbit determination, it has been explained in the above parts that a dynamical propagation of the initial state has to be performed. This process is indeed needed to compute the simulated observations and their discrepancies w.r.t. the actual data. Knowing the differential equations that describe the motion, depicted in section 2.2, it is sufficient to find the solution to those equations to obtain the trajectory of the object. However, the equations of motion only have an analytical solution in the case of simple orbits, with no perturbation or small ones [Montenbruck and Gill 2013]. In almost all real-life applications, the analytical solutions obtained through approximations of the perturbations are not accurate enough, and thus the equations of motion are solved numerically.

A numerical integration of the equations of motion relies on two main components:

- the **propagator**, or the formulation of the equations of motion. It is possible to express the state of an object in different ways (Cartesian coordinates, Keplerian elements etc.), and those different representations give rise to different formulations of the equations of motion. Although mathematically equivalent, in the context of numerical integration those different formulations can lead to different behaviours. In this study, the Cartesian formulation of the equations of motion (Cowell propagator) is used. The advantage of using such a propagator is the fact that it does not rely on any assumption regarding the behaviour of the space objects, and is a robust integrator (meaning that it does not have singularities that could lead to inaccurate results).

- the **integrator**, or the integration scheme. This describes the process to solve the equations of motion, and has a direct impact on the quality of the results. Indeed, the choice of the integrator can also involve the temporal resolution of the integration, which directly impacts the accuracy of the integration. Many integrators exist, and a trade-off analysis has been conducted in [Witte 2024] in the same context as the present study. The integrator that was found most suited is a member of the Runge-Kunta-Fehlberg (RKF) family, a variable step size RKF7(8) integrator with a tolerance of 10^{-10}, as described in [Fehlberg 1968]. The key characteristics of this integrator is the fact that its step size is adapted for each step, in order to match the rate of evolution of the dynamics. This feature allows to reduce the step in the parts where the dynamics change rapidly (e.g. in a lunar close approach), while letting it take larger values in situations where a small step is not required, thus reducing the amount of unnecessary calculations and the time taken by an estimation.

An important aspect of numerical integration is that it leads to some errors compared to an actual trajectory that would follow the dynamical model implemented. Those errors are typically increasing as the time of the simulation gets longer. For this reason, it is preferable to use the middle point of the estimation window as the initial state [Hwang et al. 2019]. Indeed, assuming that the errors are increasing with time, the total amount of error is smaller when propagating two half-windows than one full window. This can be seen mathematically from the derivation:

$$\int_0^{T/2} \epsilon(t)dt \leq \int_{T/2}^{T} \epsilon(t)dt \tag{2.20}$$

$$2\int_0^{T/2} \epsilon(t)dt \leq \int_0^{T} \epsilon(t)dt \tag{2.21}$$

$$\int_{-T/2}^{T/2} \epsilon(t)dt \leq \int_0^{T} \epsilon(t)dt \tag{2.22}$$

Here $\epsilon(t)$ is a positive, even and increasing function that models in a very simplified way the error caused by using numerical integration. T is the length of the propagation window, and thus $\int_{-T/2}^{T/2} \epsilon(t)dt$ is the total error made when estimating from the middle of the interval, while $\int_0^T \epsilon(t)dt$ is the total error made when estimating from the beginning of the interval.

2.4. Uncertainty

In this section, the principles of calculating the uncertainty associated to a trajectory are presented. First, the covariance matrix is described, and then different ways to propagate it (linear and non-linear) are explained.

2.4.1. Covariance analysis

In the orbit determination process, the result is not only a state vector, but also a covariance matrix that provides information on the uncertainty associated with the resulting trajectory. In the WLS method, the expression of the covariance $\mathbf{P_0}$ is given by:

$$\mathbf{P}_0 = (\mathbf{H}^T\mathbf{W}\mathbf{H})^{-1} \tag{2.23}$$

Moreover, in the case where an a priori covariance matrix $\mathbf{P}_0^{\text{apr}}$ is used, the final covariance matrix can be obtained from the expression [Montenbruck and Gill 2013]:

$$(\mathbf{P}_0)^{-1} = (\mathbf{P}_0^{\text{apr}})^{-1} + (\mathbf{H}^T\mathbf{W}\mathbf{H}) \tag{2.24}$$

Given these equations, it appears that in order to obtain a proper covariance matrix as a result of the WLS process, it is crucial that the weights matrix $\mathbf{W}$ and the a priori covariance matrix, when used, are properly chosen.

The weights matrix is used to convey the trust level in each observation. The values on the diagonal are called the weights, and the higher the ith coefficient is the more the cost function is penalising

having a large residual for observation i. Therefore, observations that are more trusted should be associated to larger weights. As such, it would ideally be constructed by investigating each individual observation and computing its noise based on the observing station, the illumination at that time, the age of the hardware etc. However, such information are very rarely available, and performing such an investigation for each observation could take a very long time. The solution that is commonly used is to attribute a noise level to each observatory, and to consider that all the observations made from this observatory will have the same noise level. This is an approximation, as discussed in [Luo and Yang 2017], because the changes in observing equipment or star catalogue can cause variations in the noise level. The process of estimating the noise level for various observatories, star catalogues etc. is beyond the scope of the present study, and the noise levels for the observations will be taken from existing papers that conducted such analyses [Vereš et al. 2017].

It is, however, possible to modify the weights of the observations based on other parameters than just the ground station they resulted from. A first correction that can be applied to the weights is to take into account the fact that observations from the same station on the same night are correlated with each other as shown in [Baer et al. 2011]. In order to mitigate the effects of this correlation, [Farnocchia et al. 2015] introduces the concept of a batch of observations. A batch is defined as "a sequence of observations from the same station with a time gap smaller than 8h between two consecutive observations". In a batch consisting of N observations the weight of each observation is then divided by a factor $\sqrt{N}$:

$$\sigma_{\text{new}} = \frac{\sigma_{\text{old}}}{\sqrt{N}} \tag{2.25}$$

It should be noted that a case has been made by [Vereš et al. 2017] for replacing the $\sqrt{N}$ factor by a constant weight up to 4 observations, and then use a de-weighting factor of $\sqrt{N/4}$. The present study has focused on testing the effect of the $\sqrt{N}$, but future developments could compare the effects of those two weighting methods.

In addition to that weighting scheme, another phenomenon can be taken into account, namely the fact that at higher declinations a seemingly large absolute difference in right ascension translates into a small true angular error in reality. As a consequence of this, the right ascension observations at high declination provide less information than the ones near the celestial equator. In order to mitigate this a different weight reduction is possible. For this one, the weights of the right ascensions observations are multiplied by the cosine squared of the declination of the same observation [Dirkx 2025].

$$\sigma_{\alpha,\text{new}} = \cos^2(\delta)\sigma_{\alpha,\text{old}} \tag{2.26}$$

The estimated covariance matrix, obtained as a result of the WLS process, tends to be an underestimation of the true covariance matrix. Indeed, the estimated matrix assumes that all the uncertainty on the estimated state originates from the uncertainty in the observations, and that those uncertainties are all Gaussian and uncorrelated. In reality the inaccuracies of the dynamical model and the systematic noise still present in the observations can not be neglected, and the behaviour of the uncertainties is not always the ideal Gaussian uncorrelated model. Therefore, a method is used in [Witte 2024] to compute the average ratio k_{avg} between the "true" errors (assimilated to the residuals) and the formal errors (obtained from the estimated covariance matrix). This ratio is then used to obtain the "true" covariance matrix:

$$\mathbf{P}_{\text{true}} = k_{avg}^2 \cdot \mathbf{P}_{\text{estimated}} \tag{2.27}$$

As for the a priori covariance matrix, its values are based more on a tuning decision and confidence on the existing knowledge than on a physical phenomenon. Indeed, the initial guess for the state has no physical meaning, it is merely an artifact used for the calculations, and the level of trust towards this artifact does not depend on the physics of the problem. An interpretation of the a priori covariance matrix is that the values on the diagonal are the order of magnitude of the amount by which the estimation result can differ from the initial guess. This amount can then be tuned depending on the confidence in the initial guess. As a good indication of the values for the case at hand, [Witte 2024] used 0.1 as a value for the a priori uncertainty on the radiation pressure coefficient, and 10^{-5} to 10^{-6} rad for

the observations. It is theoretically also possible for the a priori covariance matrix to have some non-diagonal non-zero values (for example to indicate that the initial guess is deemed accurate except in a direction pointing between two base vectors), but such cases require an in-depth knowledge of the initial guess, how it was obtained and where it is less trustworthy. Such an advanced insight in the initial guess is not included in the scope of this study, which aims to conduct these operations on a large scale rather than diving into the specifics of each orbit determination process.

2.4.2. Linear propagation

As a result of the orbit determination process, values for the initial state and estimated parameters are obtained, alongside with a covariance matrix that represents the uncertainty, under the assumption that the distribution is Gaussian. The purpose of this study is not however to solely perform orbit determination, but also to propagate the resulting trajectory in the future in order to anticipate potential encounters. In such a context, it is therefore necessary to propagate the uncertainty on the state as well, in order to know the confidence level of the propagation, and later to compute the risk of collision with the other objects.

The first method for propagating the uncertainty is to assume that the initial Gaussian distribution will remain Gaussian over time, and that its evolution happens in a regime where the dynamics are appropriately described using linear equations. In this context, the state transition matrix $\mathbf{\Phi}(t, t_0)$ is introduced. It is defined as:

$$\mathbf{\Phi}(t, t_0) = \frac{\partial \mathbf{y}(t)}{\partial \mathbf{y}(t_0)} \tag{2.28}$$

Where $\mathbf{y}(t)$ is the estimated state (position and velocity) of the object considered, and t_0 is the initial time. The evolution of the state transition matrix is governed by a differential equation [Montenbruck and Gill 2013]:

$$\frac{d}{dt}\mathbf{\Phi}(t, t_0) = \begin{pmatrix} \mathbf{0}_{3\times3} & \mathbf{1}_{3\times3} \\ \frac{\partial \mathbf{a}(\mathbf{r},\mathbf{v},t)}{\partial \mathbf{r}(t)} & \frac{\partial \mathbf{a}(\mathbf{r},\mathbf{v},t)}{\partial \mathbf{v}(t)} \end{pmatrix} \cdot \mathbf{\Phi}(t, t_0) \tag{2.29}$$

and its initial value is $\mathbf{\Phi}(t_0, t_0) = \mathbf{1}_{6\times6}$.

Then, the propagation of the covariance matrix $\mathbf{P}_0$ is done using the state transition matrix as described in [Fayolle et al. 2022]:

$$\mathbf{P}(t) = \mathbf{\Phi}(t, t_0)\mathbf{P}_0\mathbf{\Phi}(t, t_0)^T \tag{2.30}$$

This method is called the linear propagation, as the resulting covariance matrix is obtained through linear operations from the initial one. Such a propagation is very straightforward to implement and once the trajectory is propagated and the variational equations solved, the state transition matrix is available at every time. The major drawback is that it relies entirely on the assumption that the uncertainties propagate linearly, which is generally valid only for short periods of time. In the case of cislunar dynamics such an assumption can become completely inaccurate in the event that a close approach of the Moon happens during the time interval between t_0 and t. Therefore, other methods are also investigated in order to provide better results, or to determine the domain of validity of the linear assumption.

2.4.3. Non-linear propagation

Overview

Having in mind the objective of reaching a more accurate depiction of the uncertainty over the propagated trajectory, the linear assumption has to be abandoned, and other uncertainty propagation methods are considered.

The first uncertainty propagation method that does not require this assumption is the Monte-Carlo (MC) method. In this method, the uncertainty is assumed to remain Gaussian, but the propagation itself is performed using the dynamical propagator. Using the initial state and covariance, a sample of points is drawn at random, following a normal distribution. Each of these points is then propagated to the time of interest and the final distribution of the errors, still assumed to be Gaussian, should have a zero mean, and its covariance matrix is obtained by computing the difference between each propagated point and the nominal trajectory, and taking the covariance of those differences.

Using the MC method allows to have a better representation of the dynamics of the system, that is no longer limited by the linear domain but only by the accuracy of the dynamical model chosen for the propagator. However, the point cloud that is obtained after the propagation can not lead to an interpretation by itself. This is why, under the Gaussian assumption, the covariance matrix is computed and used to quantify the uncertainty. However, as is shown in [Horwood and Poore 2014], even when the samples are drawn according to a Gaussian distribution, the distribution can completely change its shape, for instance by stretching along the trajectory, leading to a ”banana-shape” cloud of points. Using a Gaussian distribution is thus a poor representation of the uncertainty, and other methods can prove more useful.

Gauss von Mises distribution

Based on the same principle as the MC method, [Horwood and Poore 2014] investigated the possibility of propagating a sample of points to better model the uncertainty, but instead of extracting only the covariance of the propagated points, they assumed that the final distribution was a Gauss von Mises (GVM) distribution instead of a Gaussian one. Such a distribution has more describing parameters, which allow it to fit more accurately to the data. Moreover, in the algorithm they provide, the selection of the initial data points to be propagated is not done at random, but in a way that ensures that the initial distribution is properly captured by the data points, thus avoiding the possibility that all the points are ”on the same side” of the trajectory, which could lead to skewed results in a classic MC method.

In the current study, the initial distribution is still assumed to be Gaussian, for the lack of more information on the multiple error sources. Therefore the first step to apply the GVM method is to convert the Gaussian distribution to a GVM one, which is explained in [Horwood and Poore 2014]. Afterwards, the algorithm used is the same as shown in the paper.

2.5. Broader scope

2.5.1. Other potential study objects

In order to simplify the work, the present study, following the example of [Witte 2024], is using the Chang’e 2 and 3 upper stages as the main study cases. However, a proper framework for orbit determination in the cislunar space domain would preferably be usable with a broader range of objects, instead of requiring several weeks to tune the model to each specific space object. As such, it is useful to study how the framework that has been designed for the two initial objects can be extended to other cases.

There are two options for such an extension of the study. The first one is to study how small variations of the characteristics of the object impact the results of the process. For such an investigation, using objects that are similar but not exactly the same is the most relevant, and other upper stages of similar missions that also have reported a significant amount of tracking data are considered: the Chang’e 4 and 5 upper stages.

The other possibility for studying the effect of using different objects with the same process is to push it to the limits and see what the consequences are. In such a case the objective would not be to study other cylindrical shape man-made objects, but rather asteroids that can have very different characteristics and to see whether the model is usable as is, or if some parameters require some adjustments. Since the position of the asteroids is often known with more precision than that of all the man-made objects, such a study would also allow for a better distinction between the observation errors and the dynamics modelling ones. However, asteroids do not move in geocentric orbits and only occasionally briefly enter cislunar space. They also have a much different area-to-mass ratio. This means that the behaviour for asteroids is quite different and thus if the same model is able to perform well on asteroids it would indicate a very broad range of capabilities.

2.6. Research objectives

Based on the preliminary research and the existing work, this study will be focused on *improving the existing framework for orbit determination of cislunar space objects*. In order to do so the following research objectives are formulated:

- **Expanding the scope of the orbit estimation capabilities**: The previous studies have all been

concentrating their efforts to subcases of the cislunar space, be it by restricting the analysis to certain types of orbit, of to certain estimation windows. In order to improve the process of orbit determination, this work aims to increase the number of situations where orbit determination is possible.

- **Identifying the main weak points of the current work**: In order to improve the orbit determination process, a key element is to investigate the current solutions to characterise the error that is made, and look for the possible explanations and sources for this error.
- **Improve the modelling of the observation and residuals**: The orbit determination process relies on observations, and the residuals are used to assess the adequateness of the estimation. Through an in-depth analysis of the observations and residuals, this study will aim to improve the performance of the orbit determination software.
- **Improve the modelling of the solar radiation pressure**: Although the gravitational forces are very accurately described, the model used for the solar radiation pressure is very simplified, and the present study will aim to investigate the consequences of using a more refined model on the quality of the estimation.

Formulation of the research questions

1. How much can the scope be extended, and what external inputs are required for the estimation to be performed?
2. What is the main source of error in the estimated trajectories?
3. What is the impact of refined treatment of the observations and residuals on the performance of the estimation?
4. How does a new solar radiation pressure model impact the quality of the orbit determination process?

2.7. Thesis plan

This section presents the initial research plan, established prior to starting the work. As such, some of the elements mentioned were not analysed, while new directions that were initially not considered have led to unplanned analyses.

2.7.1. Familiarisation

3 weeks

In this first part of the thesis, the existing code from [Witte 2024] will be read and understood. Then, it will be adapted to perform orbit estimations on one object and one window at a time. The inputs are as follows:

- time window
- object to estimate, chosen among the Chang'e 2 and 3 upper stages
- turn on the radiation coefficient estimation
- turn on the observation bias estimation
- dynamical model to use, chosen among the ones studied in [Witte 2024]
- initial guess of the state

The model then performs the estimation using the WLS algorithm (see subsection 2.3.2), and gives as an output the (refined) estimation of the initial state and the covariance matrix associated with this estimation. Finally, a subdivision of the time frames into individual arcs will be performed in order to cover the whole period.

The objective is to be able to perform an orbit estimation with control over the inputs, but still using the dynamical model deemed best by [Witte 2024]. The time windows selected in this stage should cover the whole time period for each object, and stable initial guesses should be found for each time window.

2.7.2. SRP study
3 weeks

In this part, a new model for the SRP (3-constant model, described in subsection 2.2.2) will be added to the propagator, and then it will be used in the orbit determination process. This will require the implementation (in Python or C++) of both a new acceleration model and an acceleration partial model. The estimation results (estimated orbit, residuals, post-fit radiation pressure acceleration) will be compared to the classical cannonball model. In order to evaluate the performance, two options are considered. The first option, which will be implemented initially, is to use the real tracking data from Project Pluto and compare the behaviour of the residuals for each time window with and without the new model. The second option, used if no clear trend can be observed in the residuals evolution, is to use simulated data and compare the results of using the 3-constant model versus the cannonball one. The observation data would be simulated using the same dynamical model as used in the estimation process, with some random noise added. Using this setup allows one to eliminate the uncertainty due to the dynamical modelling and observation errors, therefore giving a more refined insight of the effect of the new model. In this scenario, it is possible to simulate the data either using the 3-constant model for the SRP, thus checking if the code is able to retrieve the correct parameters, or using a fully panelled model, thus testing the accuracy of the 3-constant model in a more realistic scenario. In the latter case, assumptions need to be made on the panel model and body rotation.

The objective is to have run the orbit estimation process with and without this new model and to have drawn conclusions regarding its performance, measured by the evolution of the residuals, and (if applicable) the best settings to be used.

2.7.3. Uncertainty study
Observation uncertainty
2 weeks

The first aspect of uncertainty that will be investigated is the uncertainty in the observations and how to properly model it. Since a least-squares estimation model is used, random noise can only be assumed as Gaussian. For biases, both direct observation biases and time biases will be considered (see subsection 2.3.1). Currently, [Witte 2024] models the random noise as Gaussian and the systematic noise as a constant offset, assimilated to a time bias. Then, the initial covariance matrix is obtained as a result of the WLS method and ”inflated” using a so-called k-factor, as described in subsection 2.4.1. Such a method is highly empirical and does not rely on any physical origin for the resulting uncertainty. Therefore this phase will focus on studying the time and observation biases, with the objective to be able to decouple them and provide a better estimate of the initial covariance matrix. In order to do so, advantage will be taken of the fact that the time bias leads to an influence that is almost exclusively seen along-track, whereas the observation bias impacts both the right ascension and declination. Therefore, the residual and the spacecraft velocity will be computed in the (α, δ) plane, and the dot product of the two vectors will be calculated, giving insight on the magnitude of the along-track residual and its influence on the overall residual. Due to the difficulty to automate this process and the absence of knowledge of the expected results, this analysis will be performed ”manually” for a few sets of observations, and depending on the results an automated mean of performing this analysis may be implemented.

Uncertainty propagation
3 weeks

After improving the initial value of the covariance, the propagation process will be investigated. Here, the Monte-Carlo method (used in [Witte 2024]) will be replaced by the Gauss-von-Mises method described in subsection 2.4.3. The results will then be compared and the settings will be adjusted.

The objective is to have a GVM uncertainty propagation process running, and to know how it compares to the previous uncertainty propagation method.

PSA update
2.5 weeks

The Period of Sufficient Accuracy (PSA) is defined in [Witte 2024] as the time after which the uncertainty reaches more than the field of view of a typical observation telescope. This metric is fully deterministic which may not be the best way to describe an uncertain situation. Therefore a revised version of the PSA taking the probabilistic nature of the problem into account will be developed and compared to the ”classic” PSA.

The objective is to find a theoretical description of the new PSA, implement it and compare the results with the previous version.

2.7.4. Multi-arc orbit determination

Classical

2 weeks

In this part, the ”classical” multi-arc process described in subsection 2.3.3 will be used to perform the orbit determination. The different possibilities for the arc lengths, separation points and globally estimated parameters will be investigated and the accuracy of the results will be compared to the typical process, using amongst others the newly redefined PSA.

The objective is to determine the best settings for a classical multi-arc process, and how it compares to a single arc orbit determination.

Constrained

3 weeks

In this part, the settings from the classic multi-arc process are used, and a constraint is added at the separation points to limit the size of the jumps in the state, as described in subsection 2.3.3. The orbit determination process has first to be adapted to take this constraint into account, then the weight of the constraint is adjusted and the effects on the orbit determination accuracy are studied.

The objective is to be able to perform a constrained multi-arc orbit determination, to find the best settings and to evaluate how well they perform on the real data.

2.7.5. Additional objects

This part of the study aims to determine how applicable this work is to other objects, as explained in subsection 2.5.1

Preliminary study

1 week

This first part is to be done early enough to decide whether the follow-up is worth doing.

In this preliminary study, first runs of the process are performed with the Chang’e 4 and 5 upper stages, in order to determine if they give similar results to the previously studied objects (case 1) or if they lead to unexpected, complex behaviour (case 2).

In the first case, the follow-up study can be deemed feasible, whereas the second option would require a long investigation to find out both the reasons for big discrepancies and the solution for adapting the settings. Such a task would be outside the scope of this study.

In-depth study

2 weeks

This part is done only is the time remaining is sufficient and if the preliminary study has resulted in case 1.

In this part, the framework is applied to the Chang’e 4 and 5 upper stages, and the differences in performance w.r.t. the original objects are studied. If possible, explanations to those differences are sought, and if the previous settings do not yield optimal results in this case, new ones are investigated and the causes for the use of different settings is also investigated.

3

Methodology

3.1. Estimation setup

As described in subsection 2.3.4, and based on the analysis performed in [Witte 2024], the numerical integration setup used in this study uses the Cowell propagator with a RKF7(8) integration scheme. Using those settings allows for the orbit estimation process to reach an accuracy of less than 900" for more than 6 months in the context of [Witte 2024]. Given the high similarities with the present study, a similar accuracy is expected.

Finally, the dynamical model selected in [Witte 2024] is also kept almost identical for this study, as its goal is to study new information rather than performing an investigation that has already been done. The only exception to this is the modification of the SRP model that is described in section 3.6. The selected dynamical model is therefore the one shown in Table 3.1, with only one of the two SRP models being used at a time.

In the estimation process, the initial state is always estimated, and it is also possible to estimate the parameter(s) of the SRP model used (e.g. C_r for the cannonball model). This leads to two different settings for each SRP model. In addition to those four settings, it is also possible to include in the estimated parameters the observation biases described in subsection 2.3.1. Those biases are estimated per ground station, with one bias computed for the right ascension and the other for the declination. When estimating the biases, the same settings can be considered. However, when their parameters are not estimated but kept to the default values both SRP models have the same theoretical behaviour, and this will be verified in section 4.4. Therefore, only the cannonball model is kept for the settings with the observation biases included in the estimated parameters. This leads to a total of seven settings used in this study, that are summed up in Table 3.2.

The method used for the estimation is the Weighed Least Squares algorithm described in subsection 2.3.2. It is implemented using the open-source C++ package TU Delft astrodynamics toolbox (Tudat) and its Python port TudatPy [Dirkx, Mooij, and Root 2019].

In the WLS method, some weights are attributed to the observations as explained in subsection 2.3.2

Table 3.1: Dynamical models used in the study

Acceleration type	Source	Implementation
Gravity	Earth	Spherical harmonics [5,5]
Gravity	Sun	Point mass
Gravity	Moon	Point mass
Gravity	Jupiter	Point mass
Radiation Pressure	Sun	Cannonball model
Radiation Pressure	Sun	Three-constant model

Table 3.2: Estimation settings used

Settings n°	SRP model	SRP parameter(s) estimated	Observation biases estimated
1	Cannonball	No	No
2	Cannonball	Yes	No
3	Three-constant	No	No
4	Three-constant	Yes	No
5	Cannonball	No	Yes
6	Cannonball	Yes	Yes
7	Three-constant	Yes	Yes

Table 3.3: A priori covariance inputs

Parameter	Source	A priori input
C_r	Cannonball SRP	$\sigma_{C_r} = 0.1$
A_1	TCM SRP	$\sigma_{A_1} = 10$ m^2
A_2, A_3	TCM SRP	$\sigma_{A_{2,3}} = 1$ m^2
ϵ_{obs}	Observations	$\sigma_{\epsilon_{\text{obs}}} = 10^{-5}$ rad

and subsection 2.4.1. In the baseline estimation process, the weights are initially considered identical for all the observations, with a weight of 1.5 arcsecond. This value has been selected in the continuation of [Witte 2024], and according to the recommendations of [Vereš et al. 2017]. This weighting scheme will be refined as described in section 3.5.

This method also allows to introduce an a priori covariance matrix, whose role is explained in subsection 2.3.2 and subsection 2.4.1. The inputs for this covariance matrix are given in Table 3.3. The values for the cannonball radiation parameter and the observation biases are taken from [Witte 2024], while the values for the parameters introduced in the three-constant model are elaborated upon in Appendix C.

3.2. Data presentation

The observation data described in subsection 2.3.1 used in this study is presented more in-depth in this section. First, an overview of the Keplerian elements of both objects under consideration is plotted, along with the times of the observations, in Figure 3.1 and Figure 3.2.

In those figures, it is possible to identify several key features of the orbits considered. Beginning with Chang'e 2, it can be noted that the data is significantly more sparse until the end of 2014. After this the data looks rather homogeneous, until the end of 2016/beginning of 2017 where there is a jump in the eccentricity and semi-major axis plots followed by a short period with no observations. Two additional combinations of a sudden jump in the orbital elements with a gap in the observation data can be seen in 2019 and at the end of 2020.

As for the Chang'e 3 upper stage, it appears that the beginning (until 2016) of the observation period is quite chaotic, while having a dense set of observations. At the end of 2016, there is a sudden jump in all the orbital elements, and following this their behaviours seem to be more smooth (although not flat as a perfectly Keplerian orbit would be). Over a ~2-year period following the jump in 2016 the data becomes much more sparse, before progressively getting more dense at the beginning of 2019.

In addition to the Keplerian elements, the distance to the Moon is plotted in Figure 3.3. In this figure, a threshold of 50.000km is selected to detect a "close approach". This value has been empirically chosen with the objective to correlate the close approaches to the jumps seen in the Keplerian elements evolution, rather than from a dynamical perspective. Indeed, it can be observed that all of the times where the distance to the Moon crosses the threshold correspond to a jump in at least one of the orbital elements in Figure 3.1 and Figure 3.2. This leads to the identification of 4 close approaches for the Chang'e 2 upper stage: on 23/09/2011, 27/10/2016, 19/04/2019 and 12/06/2019. For the Chang'e 3 upper stage, only two close approaches are obtained with this process: on 16/07/2014 and 16/09/2016. This method, however, does not explain the last jump in the semi-major axis of the Chang'e 2 upper

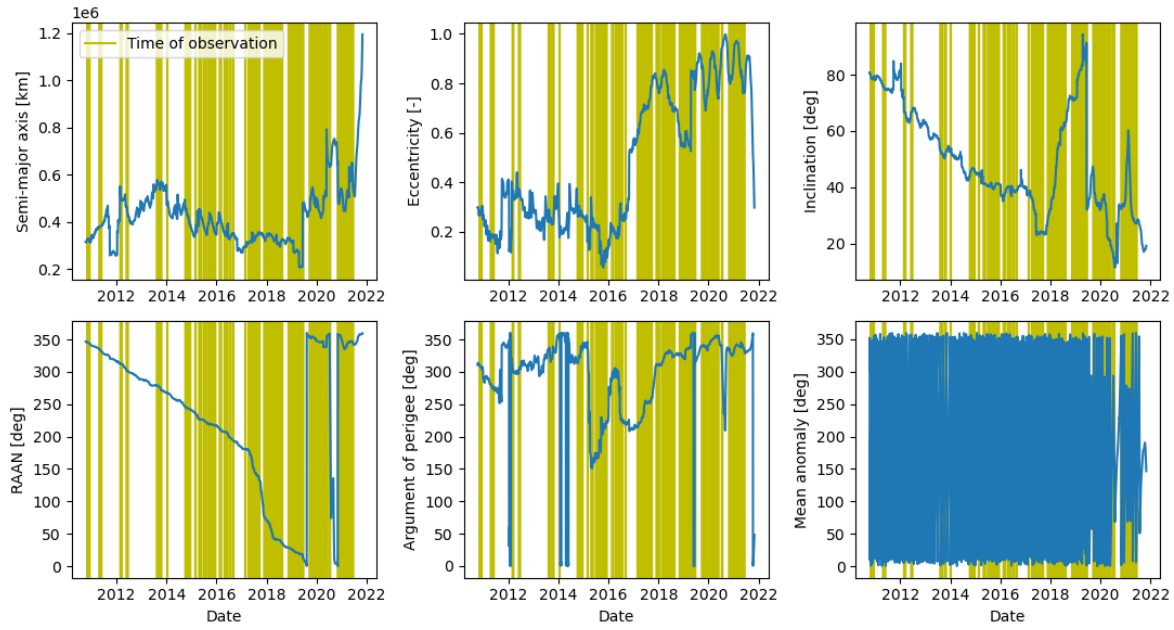

Figure 3.1: Keplerian elements of the Chang'e 2 upper stage over the whole observation period

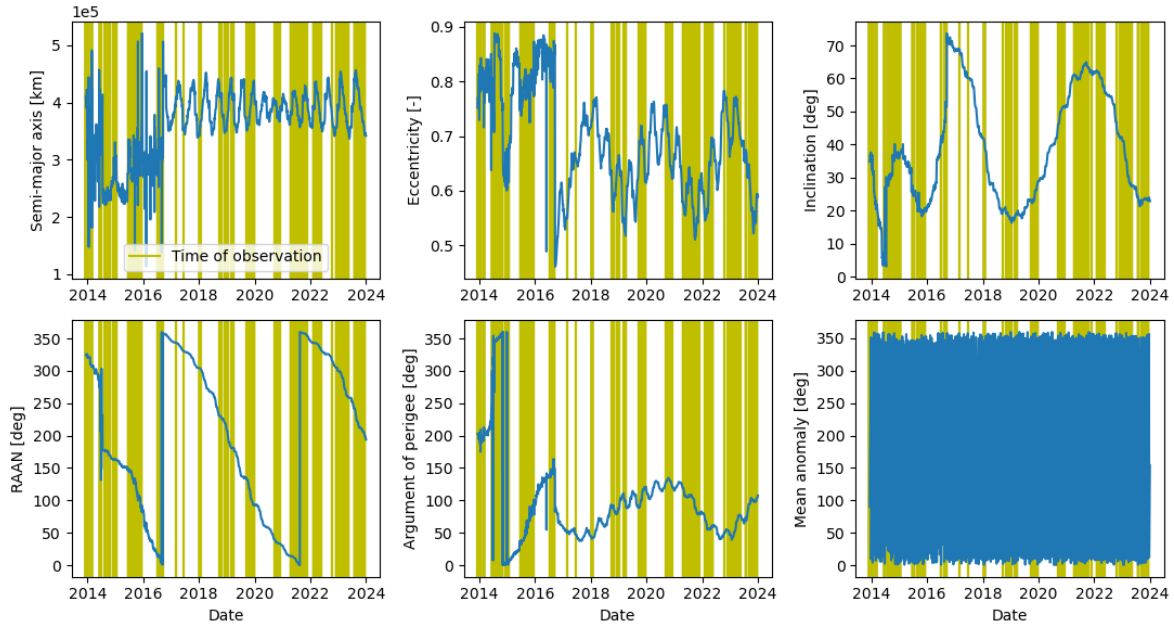

Figure 3.2: Keplerian elements of the Chang'e 3 upper stage over the whole observation period

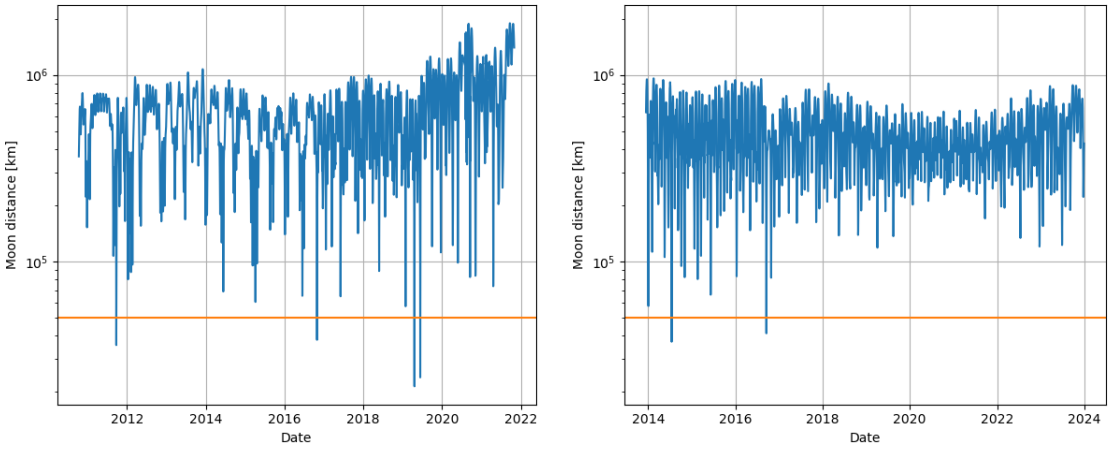

(a) Chang'e 2

(b) Chang'e 3

Figure 3.3: Distance to the Moon over the observation periods, along with the 50.000km threshold for a close approach

stage at the end of 2020.

The presence of the lunar close approaches provides a logical explanation to both the jumps in the orbital elements and the lack of data. Indeed, a close fly-by of the Moon leads to a large perturbation, susceptible to greatly modify the trajectory. This in turn makes the future position of the object harder to predict and it is thus lost for some time.

3.3. Full-window coverage

In [Witte 2024], the estimation process has been performed on a restricted number of samples (windows) from the whole observation period. This choice has been well argued and made sense for a first work on the topic. However, a major reason for having those windows and selecting them was the lack of reliability of the initial guess provided by the MPC data. Indeed, it is explained that for a number of conditions (initial guess time/estimation period), the initial state estimate extracted from the MPC data led the estimation process to not converge, thus being unexploitable.

In order to remediate this issue, the current work implemented a bootstrapping method where an initial external guess is used for the first window (or arc), but for every following window the estimated state from the current one is propagated to the initial guessing time and used as an initial guess.

This requires the estimation windows to not be too distant in time, as a propagation of an imperfect state with an imperfect dynamical model would lead to a very wrong initial state estimate for the next arc. However, this constraint is completely compensated by the fact that bridging long time intervals between two periods of interest can be done by simply adding intermediate windows.

In practice, a close approach of the Moon can often make this process more complex than theory would have it. Indeed, a close approach of the Moon pushes the dynamics of the system in a highly non-linear regime, with small errors in the state before the flyby being amplified by several order of magnitude. This alone can make the estimator struggle to converge after a lunar close approach. Unfortunately, this difficulty to predict the trajectory after a lunar approach also impacts the observations: if the object is not close enough (within the typical telescope field of view) to the estimation, then it will be "lost" and not be observed with the same regularity until it is found again, usually by chance. Putting those two effects together means that a close approach to the Moon makes the dynamics harder to predict, while having less observations to guide the estimator. And thus in such cases even the initial guess provided by the previous window can not always make the estimator converge. This is not an impossible obstacle to overcome, as tuning the window length and the time of the first estimation can allow the estimator to cross this period while still converging.

This bootstrapping method aims at reducing the number of external guesses needed to perform the estimation over the whole observation period. However, as long as they are the only guesses available,

it means that in order to obtain the initial guess for an arc that is located far away from this external guess there is a lot of computation time required, because all the intermediate arcs are needed to reach the selected one.

In order to remediate this situation, the estimation is ran over the full observation period, using the necessary external guesses, and the states are saved through this estimation, to be reused for the following analyses. The interval between two consecutive saves has been chosen as a trade-off between the guarantee of obtaining a guess that leads to a stable estimation process when used, and the amount of information that would be stored. In practice, it has been found that storing the estimated state every month was too scarce, as it would often result in being unable to reach convergence for the estimation process, especially when near a close approach of the Moon. On the other hand, reducing this interval to one week leads to the disappearance of almost all convergence issues.

A useful consequence of being able to perform the estimation in such a self-sustained manner is that this makes the work done in this study more applicable to real-life situations. Indeed, in the previous situation where the initial guess is provided by an external source (which could be different from the MPC data), the estimation process that is described can only be applied once some other process has already estimated the position of the space object to a satisfying point. This means that the framework described would, in the best case scenario, serve as an improvement over the initial guess, and in the worst case scenario be as accurate as the provided initial guess, and therefore become redundant. However with this method, the new framework can use new data to estimate the position of the space object as long as it has an initial guess from sometime in the past, which is much closer to a real-life estimation situation.

In addition to this bootstrapping method, the stability of the initial guess has been increased (for estimation windows with the same length) by moving the time of the initial guess from the beginning of the window to the midpoint of the window as described in subsection 2.3.4. This ensures that the differences between the true trajectory and the estimated one that are due to improper modelling of the environment have less time to grow, thus making the convergence of the Least Squares algorithm simpler.

Finally, in order to reduce the computation time required for performing orbit estimation over all the arcs, a parallel computation framework has been setup. This method requires an initial guess for each of the arcs, and then performs the orbit estimation in parallel for all the inputs it has been provided, and returns the estimated parameters along with the residuals. The initial guesses for all the arcs are retrieved from the states saved during the initial estimation that was performed using the bootstrapping process described above. This configuration allows to cut the runtime of a full estimation by an order of magnitude, with the potential of even further reduction when more cores are available on the computer running the estimation.

3.4. Arc overlap

As the true trajectory is always unknown, it is not possible to know the exact value of the error. Moreover, the observation residuals, while providing useful information regarding the error, do not guarantee that all the error comes from mismodelling the trajectory. Indeed, the residuals that are neither flat nor random after the estimation process can come from:

- an improper value of the postfit initial state or parameters
- an inaccurate modelling of the environment
- unresolved errors in the observations themselves (biases)

The first source is usually considered to be the least impactful one, as the Least Squares algorithm is specifically designed to find the initial state that minimizes the residuals. This is however not foolproof, as it relies on linearising the problem and could find a value that is not the ideal one if the initial guess is in the wrong region of the design space.

The second source is significantly more important, as its consequences have an impact on several key parts of the estimation process. First, having inaccurate dynamics leads the modelled trajectory to diverge from the real one, even with exactly the right initial conditions. Such a divergence will cause

residuals to increase as the simulation gets further from the initial time. But improper physical modelling, along with any error not parametrised in the estimation, also impacts the initial state estimation. Indeed, the Least Squares method uses the linearized partials of the forces considered in order to perform its steps. As such, the estimated initial guess will also be impacted by a flawed acceleration modelling.

Finally, the observation biases are the errors introduced before any estimation process is even considered: at the time of the observation. They can have various sources but they are less representative of the quality of the estimation process (unless they are themselves estimated). The relative contribution of those biases to the error is not yet known as it is one goal of this study to analyse the different contributions to the error. However, such observation biases are taken into account in astrometric observations of near-Earth asteroids, such as in [Vereš et al. 2017]. The present study is focusing on objects closer to Earth whose angular velocity (as seen from the station) is larger, and thus time biases for instance can be expected to pay a more prominent role, as a similar time difference will lead to a higher error in the estimated position.

Overall, the residuals while providing good information for the quality of the estimation (and of the prediction if additional residuals are used outside of the estimation window) do not give a complete and direct information regarding the absolute error of the trajectory of the space object.

In [Witte 2024], the analysis of the performance of the estimation was in part done by comparing the out-of-sample residuals of windows of different lengths. Because the observation data is not homogeneously spread across the observation period, such comparisons can only be done between windows that end on the same date. In this study, the windows (or arcs) selected all have different ending dates, which renders this method inadequate.

Using overlapping arcs can help remediate this issue by opening up a way to gain information (more specifically a lower bound) of the real error done by the estimator without the need for comparable residuals. The reason this is possible is because when two arcs use a 1 year window for the sampling data but the starting dates are different by 6 months, the initial states estimated for those two arcs will not correspond to the same trajectory (due to the partially different data that is taken into account). This means that during the 6 months of overlap of those two arcs there are two estimations of the trajectory that are available. Computing the difference between those two trajectories then allows to find a lower bound for the absolute error with respect to the true trajectory.

Assuming we have the real trajectory $\mathbf{x}_r$ and the two estimated ones $\mathbf{x}_{e1}$ and $\mathbf{x}_{e2}$, the error that the estimator can make is: max($||\mathbf{x}_r - \mathbf{x}_{e1}||$, $||\mathbf{x}_r - \mathbf{x}_{e2}||$). In the best case scenario, this error is minimised by having $\mathbf{x}_r = \frac{\mathbf{x}_{e1}+\mathbf{x}_{e2}}{2}$, and in this case the error of the estimator becomes

$$\varepsilon = \frac{\mathbf{x}_{e1} - \mathbf{x}_{e2}}{2} \tag{3.1}$$

Therefore, the difference between the trajectories computed from the two overlapping arcs gives twice the lower bound of the true error that results from using this estimation process.

This is already useful as it gives an order of magnitude of the uncertainty that comes with estimating the trajectory, but the results are not only in magnitude of the error, but can also be treated component-wise. In such an analysis, the ε error vector is projected along different reference frames to gain insight on the way the error is tied to the trajectory itself.

Indeed, the internal representation of the state that comes with the Cowell propagator is the Cartesian coordinates. Analysing the error vector in this frame would, however, not give conclusive results, as those coordinates vary over several orders of magnitude, and their correlation to the physical trajectory of the object is not easy to interpret from a graph.

For this reason, different frames are chosen to project the position difference, thus giving a better understanding of the physical reality behind the difference. The two frames chosen for this analysis are the RSW and TNW frames, as described in [Vallado 2001] and illustrated in Figure 3.4. The RSW frame is defined by having the X-axis point from the origin to the object (thus being called Radial), the Y-axis is contained in the orbital plane pointing in the direction of the velocity, but not collinear to it unless the orbit is circular, or at certain points of elliptic orbits (such as the periapsis and the apoapsis), and the Z-axis completes the right-handed coordinate system. The TNW frame on the other hand has its

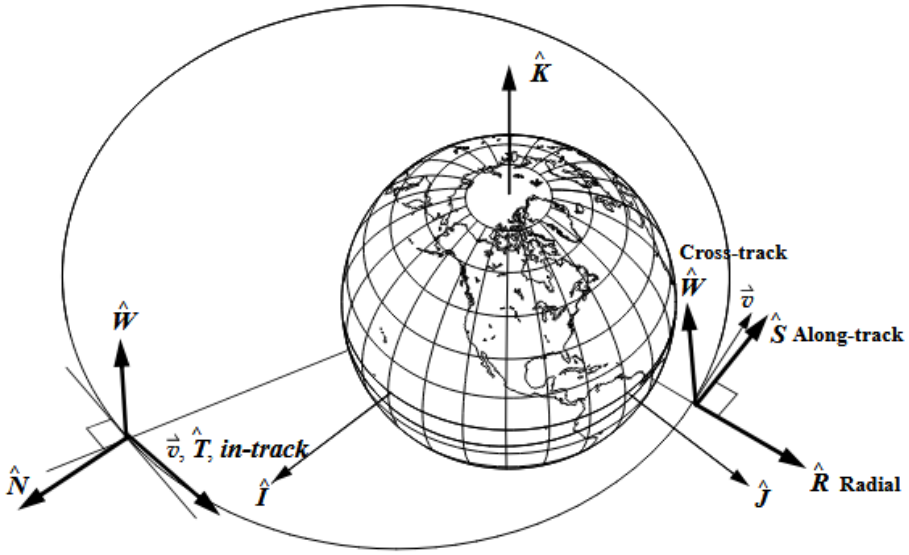

Figure 3.4: Definition of the RSW and TNW reference frames [Vallado 2001]

X-axis aligned with the velocity of the space object, pointing in the same direction (thus the Tangential name), the Y-axis in the orbital plane pointing away from the origin (but not necessarily in the exact direction of the origin except in the special cases mentioned above for the RSW frame), and the Z-axis completing the right-handed system.

It has to be noted that those frames are dependent on the estimated state of the space object, and thus the frames corresponding to the two different solutions will present some differences. In order to assert the effect of those differences on the projection of the error vector, the analysis will include testing using the frames of each solution, in order to check that there are no major variations.

Following this analysis, a first explanation for the position difference between the two estimated trajectories can be investigated. This explanation is the idea that one of the estimated trajectories is ”lagging behind” the other one, thus indicating that the two estimated positions are lying on similar orbits, but located at different points on this orbit. In order to test this possibility, the instantaneous delay between the two estimated positions is computed. This delay is defined as the along-track delay, and thus is computed using the T-component of the position difference, divided by the estimated velocity (which is, by definition of the TNW frame, exclusively along the T- direction). The expression for the instantaneous delay is thus:

$$\Delta t_{inst}(\theta) = \frac{x_T(\theta)}{v(\theta)} \tag{3.2}$$

3.5. Residual analysis

It has been mentioned in subsection 2.3.1 that the observations are not entirely accurate, with multiple effects potentially impacting the measured quantities. This, in addition to the fact that the model used in the estimation process is not perfect, leads to the apparition of differences (or residuals) between the actual observations and the simulated ones. Those residuals give a measure of the performance of the estimation process, and therefore this section presents methods to analyse the residuals and potentially reduce their values.

First, two methods for refining the weighting scheme are presented in subsection 3.5.1. The process of visualising the residuals in the along-track/cross-track coordinates is then described in subsection 3.5.2. Finally, some analyses on the behaviour of the residuals are introduced in subsection 3.5.3.

Table 3.4: Weighting scheme settings

Settings n°	Batch weighting	Right ascension weighting
1	Yes	Yes
2	Yes	No
3	No	No

3.5.1. Weighting schemes

As described in subsection 2.4.1, two corrections to the uniform weighting scheme used in [Witte 2024] are considered: the batch weighting defined in Equation 2.25 and the right ascension weighting defined in Equation 2.26. The best model is expected to be the one where both of these corrections are applied. This is thus the estimation settings that are used as a baseline in this study. In order to investigate the impact of those weighting schemes, two additional settings are defined in Table 3.4. The right ascension weighting is first turned off in setting n° 2, and then the batch weighting is also turned off in setting n° 3.

In order to evaluate the impact of those weighting schemes on the residuals, the Root-Mean-Square (RMS) of the residuals can be computed. This indicator is computed both on the in-sample (IS) residuals and the out-of-sample (OOS) ones. The IS residuals refer to the residuals computed only on the observations within the estimation window, while the OOS residuals are computed on the observations from a 6-month period following the estimation window.

Those analyses are also performed to evaluate the impact of including the observation biases in the estimated parameter vector, as described in section 3.1. However, since the biases are only estimated on the ground stations that provide the in-sample observations, some out-of-sample observations have no bias estimated. For this reason, when estimating the observation biases the residuals are only analysed in sample.

Another processing that can be relevant for making the observations more realistic is to filter out the observations that lead to an excessive value for the residuals. The rationale for doing this is the fact that if an observation that is used for performing the estimation still has a residual of over 0.01° it does not bring satisfying information to the estimation. Indeed, if the Least Squares process is not able to get closer to this observation, two options are possible. The first is that the observation is wrong, likely because of the different sources of error that have been mentioned above, or even because it has been attributed to the wrong space object. In this situation excluding the outlier observations allows to avoid taking wrongful information into account when estimating the trajectory of the space object, which is most likely to lead to better results when validating the trajectory with out-of-sample observations.

The second possibility is that the physical modelling that is currently used is imperfect enough to be unable to accommodate for those observations. In this case, including them in the estimation forces the estimation process to compromise and can potentially lead to a trajectory that performs worse out of sample (i.e. over-fitting). In this situation, excluding the observation allows to improve the trajectory, but it is not completely discarded. Indeed, it is important to know that the model is not able to take all of the observations into account as it could lead to identifying weaknesses in the dynamical model, that can then be solved in future studies.

3.5.2. Along-track/cross-track conversion

Given the sources of errors discussed in subsection 2.3.1, in particular the streak effect, it is expected that the residuals will be larger in the along-track direction. In order verify this, the residuals can be visualised in the along-track/cross-track plane. To do that, the direction of the velocity of the spacecraft has to be determined for each observation. This however can not be done simply by using a rotation matrix from the inertial reference frame to the right ascension/declination frame, because the coordinates in which the observations and residuals are computed are angular ones that are not linearly related to the Cartesian coordinates. The transformation from Cartesian coordinates (x, y, z) to (α, δ) is found in [Montenbruck and Gill 2013] and can be expressed:

$$\alpha = \arctan \frac{y}{x} \qquad \delta = \arctan \frac{z}{\sqrt{x^2 + y^2}} \tag{3.3}$$

In this expression, it is important to chose the adequate quadrant for α depending on the sign of x, taking α between -90° and 90° if $x > 0$, but between 90° and 270° when $x < 0$.

The solution chosen to obtain the velocity in the (α, δ) plane in the present study is therefore to take inspiration from Figure 2.2, on which the direction of the velocity can be clearly seen from the alignment of the observations, and the sense could be easily determined by knowing which observation was done first.

Using series of consecutive observations would allow to recover the observed velocity in the (α, δ) plane, but there are no guarantee that multiple observations are always available, nor that they are close enough to allow to determine the velocity from their alignment. Therefore, instead of the observed velocity, the estimated one is used. The velocity is thus retrieved from the estimated trajectory by simulating a second observation shortly after the real one, and using the difference between the two simulated observations as the velocity vector, as shown in Equation 3.4.

$$\mathbf{v} = \begin{pmatrix} v_\alpha \\ v_\delta \end{pmatrix} = \frac{1}{\Delta t} \left(\begin{pmatrix} \alpha_{\text{sim, 1}} \\ \delta_{\text{sim, 1}} \end{pmatrix} - \begin{pmatrix} \alpha_{\text{sim, 2}} \\ \delta_{\text{sim, 2}} \end{pmatrix} \right) \tag{3.4}$$

Here $\mathbf{v}$ is the velocity vector in the (α, δ) plane, Δt is the time interval between the two simulated observations, and $\alpha_{\text{sim, i}}$ (resp. $\delta_{\text{sim, i}}$) indicates the right ascension (resp. declination) of the i-th simulated observation.

The velocity vector $\mathbf{v}$ gives the along-track direction, and in order to obtain a vector that points in the cross-track direction it is possible to simply rotate $\mathbf{v}$ by 90°, thus yielding $\mathbf{w} = \begin{pmatrix} -v_\delta \\ v_\alpha \end{pmatrix}$, and they both have the same norm: $v = w$.

Once the along- and cross-track directions have been properly computed in the right ascension/declination plane, they can then be used to rotate the residual vector to the new frame by projecting it on its base vectors. The along-track residual is obtained by projecting the residual vector on the unit velocity vector and the cross-track residual by projecting on the unit vector $\hat{\mathbf{w}} = \mathbf{w}/w = \mathbf{w}/v$

$$\rho_{\text{at}} = \boldsymbol{\rho} \cdot \frac{\mathbf{v}}{v} = \frac{1}{v} \begin{pmatrix} \rho_\alpha \\ \rho_\delta \end{pmatrix} \cdot \begin{pmatrix} v_\alpha \\ v_\delta \end{pmatrix} = \frac{\rho_\alpha v_\alpha + \rho_\delta v_\delta}{v} \tag{3.5}$$

$$\rho_{\text{ct}} = \boldsymbol{\rho} \cdot \frac{\mathbf{w}}{v} = \frac{1}{v} \begin{pmatrix} \rho_\alpha \\ \rho_\delta \end{pmatrix} \cdot \begin{pmatrix} -v_\delta \\ v_\alpha \end{pmatrix} = \frac{-\rho_\alpha v_\delta + \rho_\delta v_\alpha}{v} \tag{3.6}$$

Here, ρ_α (resp. ρ_δ, ρ_{at}, ρ_{ct}) is the right ascension (resp. declination, along-track, cross-track) component of the residual vector $\boldsymbol{\rho}$.

The observations for a given arc are then combined in a single analysis to allow for a more global overview of the results.

3.5.3. Spread analysis

Finally, the direction of the largest spread in computed by performing a linear regression on the residuals:

$$\rho_{\text{ct}} = a\rho_{\text{at}} + b \tag{3.7}$$

Such a regression is done to find whether or not the residuals are mostly distributed along-track, cross-track, or if there is not clear trend. Indeed, the value of the slope a provides information on the main direction of the spread of the residuals. If the slope is close to 0, the linear regression is almost flat and the residuals are mostly distributed along-track. A slope of ± 1 indicates that the main direction of the spread is exactly at a 45° angle between along- and cross-track, and a slope value above 10 indicates that the residuals are mostly distributed cross-track.

Finally, in order to have a full overview of the residuals distribution in all the arcs at the same time, the slopes of the linear regression of all the arcs can be analysed. However, the relevance of the slope

should be taken into account in the analysis, as computing a linear regression is not always the most relevant treatment to apply to a cloud of points. For instance, in the case of points that are perfectly distributed along a circle, any direction has the same spread, and therefore the slope computed from a linear regression would be very sensitive to a small variation of a few points.

In order to take this effect into account, the spread ratio is also computed for each arc. The spread ratio r is defined as the ratio of the standard deviation in the along-track direction σ_{at} and the one in the cross-track direction σ_{at}:

$$r = \frac{\sigma_{\text{at}}}{\sigma_{\text{ct}}} \tag{3.8}$$

Due to this definition, a spread ratio of 1 indicates that the data distribution is mostly homogeneous in the two direction, thus meaning that the slope value for this arc should not be considered too highly. On the other hand, a spread ratio above 2 or below 0.5 indicates that the data is likely elongated in one direction, meaning that the slope value is relevant or this arc and should be taken into account for drawing any conclusions.

3.6. Three constant model

In order to improve the accuracy of the orbit determination and propagation of cislunar space debris, a new SRP force model has been investigated. This model has been presented in section 2.2, and the initial guess for the parameters is taken to be $[-C_r A, 0, 0]$. On top of this model for the radiation pressure, the shadowing effect of the Earth is also taken into account, using the expression found in Section 3.4 of [Montenbruck and Gill 2013].

In order to verify the validity of the implementation of the new model for the SRP, it has to be tested before being used in the actual estimation process. In order to do that, a simplified situation is considered, with a reduced dynamical model and individual components being turned on one at a time. Then, a second validation step is taken by comparing the result of a propagation with the cannonball model and another one with the TCM setup to imitate the cannonball model. Finally, in order to validate the implementation of the model in an estimation context, the partials are also tested in the linear regime. The way to validate this is to propagate the trajectory with a small variation of the initial state and then compare the difference in position predicted by the solution of the variational equations and the actual difference that results from the propagation. The results of this process are presented in Appendix C.

Then, the new performance of the estimation process is analysed by first studying the evolution of the in-sample residuals. As this study aims to look at a global improvement over the whole observation period, the residuals are no longer considered per observation, but per arc. The way to do that is to compute the RMS of the residuals for each arc, and to then compare those values with the cannonball model to the ones obtained with the TCM.

In addition to comparing the cannonball model to the TCM, the effect of estimating the parameters is also investigated. Indeed, when including new parameters there is the possibility of giving too much freedom to the estimation process (if the number of observations is too small), and thus it is worth making sure that the residuals actually go down when estimating the parameters compared to using the default values.

Once the IS residuals have been analysed, the out-of-sample residuals also have to be investigated. The reason for that is to make sure that if the IS residuals go down it is not simply due to over-fitting the trajectory. Over-fitting would indeed lead to a decrease in the IS residuals, but the estimated state and parameters would not be representative of the real trajectory and the OOS residuals would then increase. Checking the OOS residuals thus allows to investigate the accuracy of the prediction portion of the process, which is the most relevant part in a real-life application.

4

Results

In this chapter, the main results obtained during this study are presented. First, the results of extending the estimation period to a broader portion of the observation period are discussed in section 4.1. Then, the position difference during the arc overlaps is computed, analysed, and some potential explanations for the observed behaviour are proposed in section 4.2. In section 4.3, the distribution of the post-fit residuals is analysed, and the effects of changing the weighting scheme are investigated. Finally, section 4.4 delves into the impact of replacing the cannonball radiation model with the TCM.

4.1. Full coverage

In this section, the new periods covered by the estimation process are presented, along with the number of external guesses required and their location. The bootstrapping process, described in detail in section 3.3, is applied to the observation data presented in section 3.2. In this process, an external guess is used to initialise the WLS method for the first window. Then, for each new window (or arc), the initial guess is taken from the estimated trajectory obtained with the previous arc. The estimation is performed using the settings n° 1 from Table 3.2, which uses the cannonball SRP model, and estimates only the initial state. This leads to a very efficient estimation where the need for initial guesses has been reduced to only one for the whole period for Chang'e 3, and two for Chang'e 2, as can be seen in Figure 4.1 and Figure 4.2.

For Chang'e 3, the situation is very close to ideal: the only external initial guess that is used dates back approximately ten years before the last observation data. This would be the ideal situation in a real-life scenario. Indeed, when e.g. planning for a future mission, the most relevant information is obtaining trajectory prediction in the future. This matches the Chang'e 3 profile, as almost all the observation period is located after the external guess.

For Chang'e 2 on the other hand, two guesses were needed and even then the whole observation window is not covered. The coverage stops on the 01/02/2014, while the observation data goes back until 11/10/2010. It has been decided that the coverage did not need to be extended over this 3.3 year period. The reason for this choice is a tradeoff between the effort required to be able to properly cover this period versus the benefits from doing it. Indeed, the process of finding an initial guess that covers as much data as possible is not deterministic and relies on a lot of trial and error. Indeed, potential initial guesses are obtained as interpolations from the TLE data provided by the Find_Orb software [Gray 2022], and thus there is an infinite amount of possibilities. Moreover, it can be hard to predict whether including an extra data point will help the convergence of the Least Squares algorithm or hinder it. This can depend on many factors such as the amount by which the additional observation would differ from the otherwise-estimated trajectory, the amount of time between the last used observation and the new one etc. As a conclusion, obtaining an external guess (or several of them) that would allow for a coverage of the initial 3.3 years would involve a lot of manual testing, as the number of possibilities is large, and there is no way to evaluate a guess before actually testing it.

In addition to that, the outcome of extending the coverage have no guarantee to prove useful to this

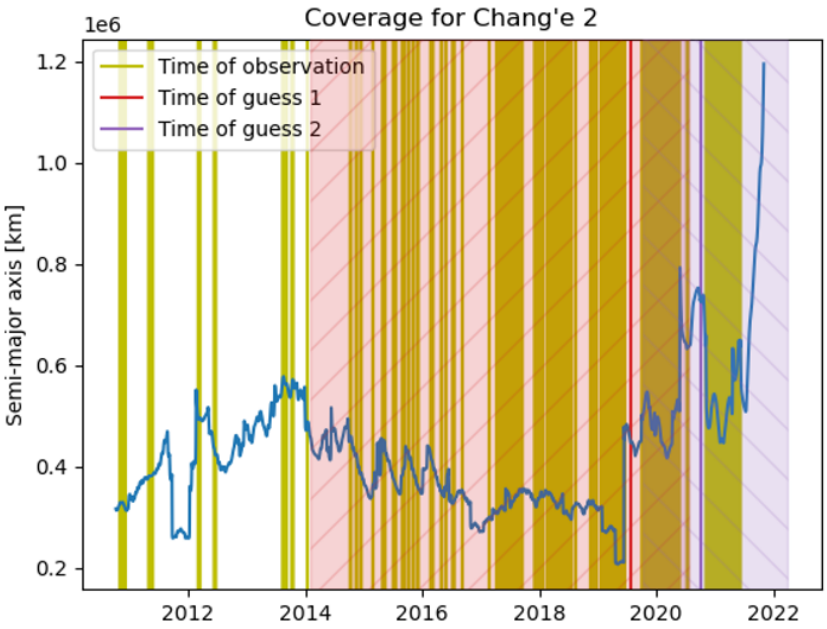

Figure 4.1: Coverage of the observation window for Chang'e 2

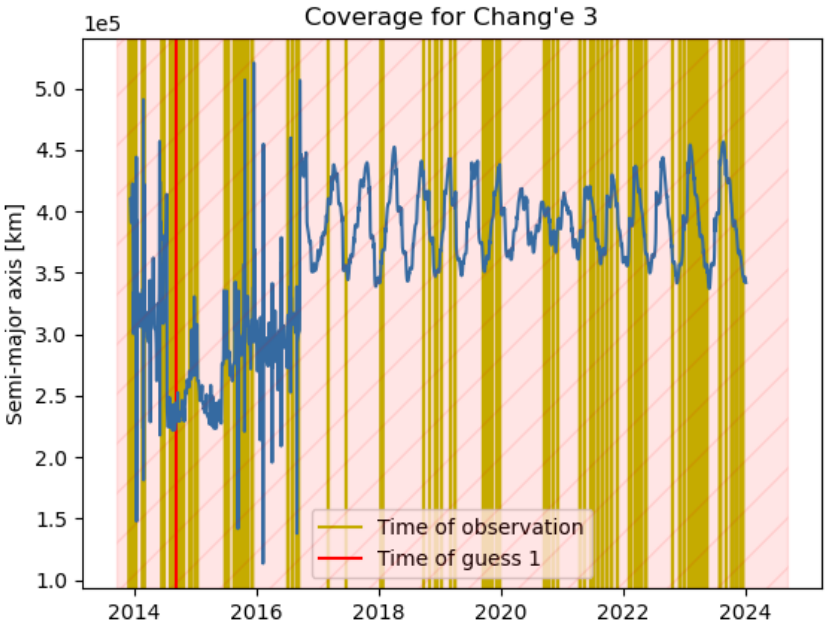

Figure 4.2: Coverage of the observation window for Chang'e 3

study. Indeed, the scarcity of the data in this period means that the convergence of the estimation process is far from assured, which in turn implies that the guess given from one arc could be too far from the real trajectory to be of use for the next arc. From a very quick overview, this could mean that three to five external guesses could be required for these 3.3 years, whereas only 2 guesses are needed for the remaining 8-year period. In addition to making things more difficult, the sparse data also makes the process less relevant to the real-life applications. This is due to the fact that more recent data tends to be more dense, as can be seen later for both Chang'e 2 and Chang'e 3.

Finally, once again comparing the situation to a real-life one, being able to estimate the state of the studied space object eight years in the past is usually not the main focus. It is obviously useful for a better understanding of its history and for improving the ability of the estimation process to handle more "rough" estimating conditions, but it is beyond the scope of the present study, and thus the two guesses covering most of the observation window are deemed satisfying and kept as such for the following.

Those results show that the estimation process implemented in this study is, in some cases, able to provide relevant predictions in a realistic scenario, thus showing its operational validity. It is, however, not always the case, as the Chang'e 2 example showed. From this, it is important to note that the model has shown its capabilities, but that the data distribution is a very important factor in the prediction power, and the framework described in the present study can be affected by the observations. This translates in requiring an external guess from late in the data, and back-propagating it. This is of course not possible when working on the estimation of current data, as back-propagating would require an external guess from the future. In such cases, it is possible to perform an Initial Orbit Determination (IOD) to obtain a rough initial guess, which can then be refined using the process studied in the present work. Several methods for IOD are described and compared in [Schaeperkoetter 2012].

As explained in section 3.3, the estimated states are then saved, with a time interval of 1 week between two entries, as such an interval has been found to limit the amount of data to store, while allowing for almost no stability issues when using the saved states as initial guesses. The very few ones that remain are, once again, located right after the close approaches of the Moon, and they are not always solved with more dense saves, but rather by using the next/previous saved states as an initial guess. Since the arcs considered in the present study have a length of one year, a shift of one week for the initial guess is considered to have a very limited impact on the uncertainty at the ends of the arc, and thus one week is found to be a satisfactory compromise between stability of the estimation and size of the saved states.

4.2. Arc overlap study

In this section, after performing the estimation over the periods shown in Figure 4.1 and Figure 4.2, the process described in section 3.4 is applied to every set of two consecutive arcs. This is done in order to find the lower bound for the true error, and potential explanations as to where it is originating from.

The position difference between the estimated trajectories in the overlap between two successive arcs is computed and analysed. The different components of the position difference in the arc overlaps are analysed in several manners to deduce the underlying sources of error in the estimation. It is found that the difference is almost exclusively in-track and that its behaviour can be well explained by the introduction of an instantaneous delay between the two estimated positions. In addition, some possible explanations for such a delay to be present are given.

The analyses conducted and presented in this section are based on the totality of the arcs considered in section 3.3 and their overlaps. However, for clarity purposes details of only two representative overlaps have been selected and will be presented here. Those overlaps are the overlaps between arcs 1-2 and 3-4 of the Chang'e 3 data. The orbital elements for those two overlaps are presented in Figure 4.3 and Figure 4.4. Several plots summarizing figures of merit for all overlaps of both objects will also be presented, and individual figures for each arc are available in Appendix A for a more exhaustive overview.

4.2.1. Component-wise analysis

The evolution of the magnitude of the position difference in the two overlaps considered can be seen in Figure 4.5. The most prominent observation is the fact that the magnitude of the difference between

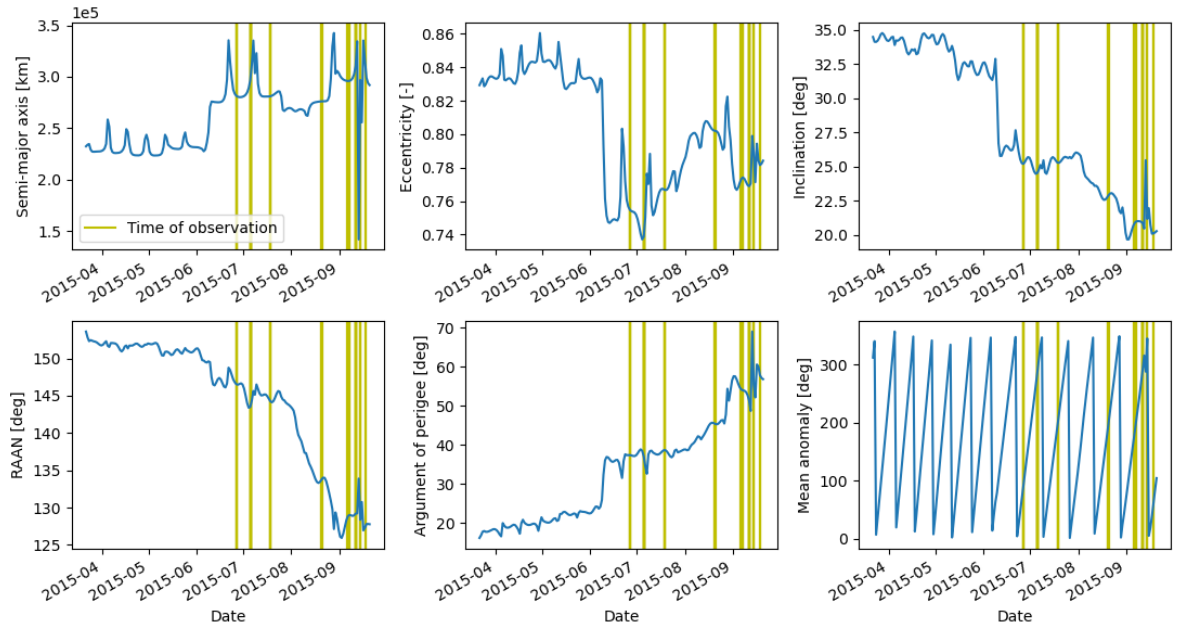

Figure 4.3: Keplerian elements during the overlap between arcs 1-2 for the Chang'e 3 upper stage

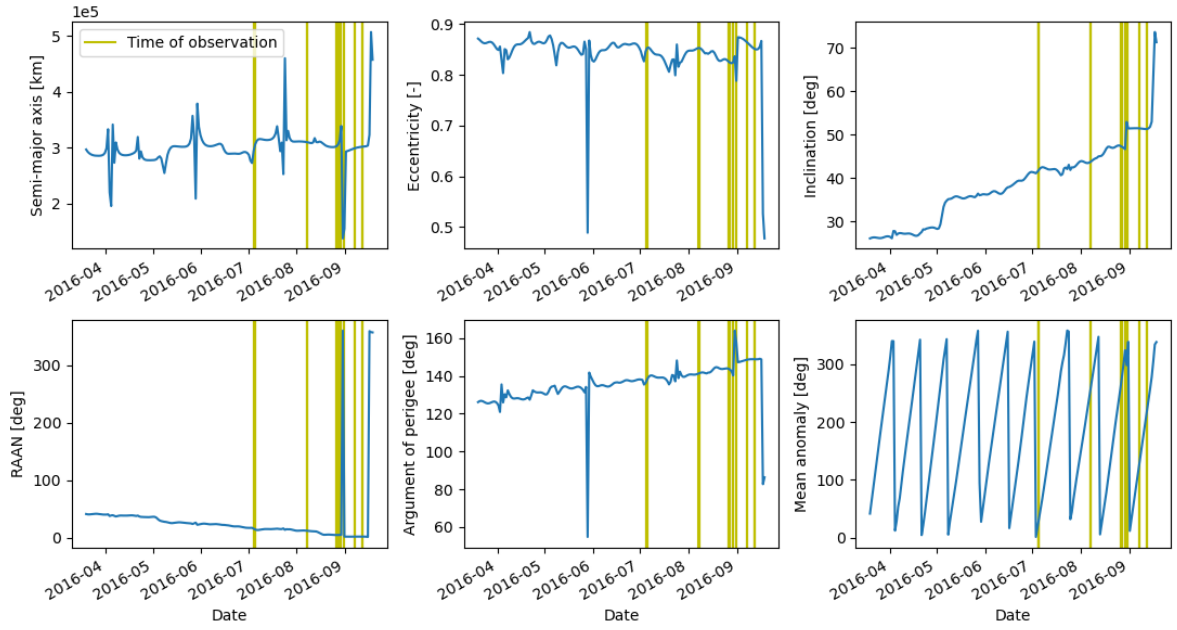

Figure 4.4: Keplerian elements during the overlap between arcs 3-4 for the Chang'e 3 upper stage

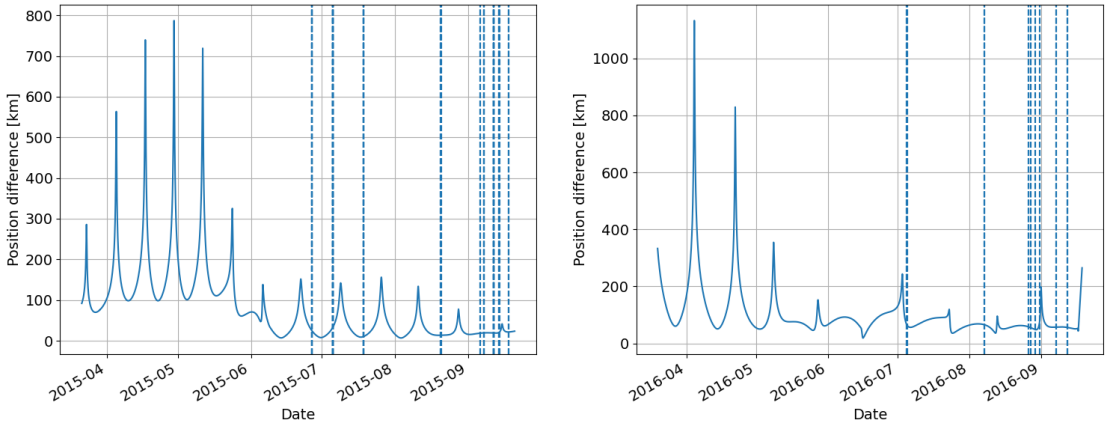

(a) Arcs 1-2 **(b)** Arcs 3-4

Figure 4.5: Absolute position difference between the estimated trajectories from two consecutive arcs. Dashed vertical lines indicate the observation times.

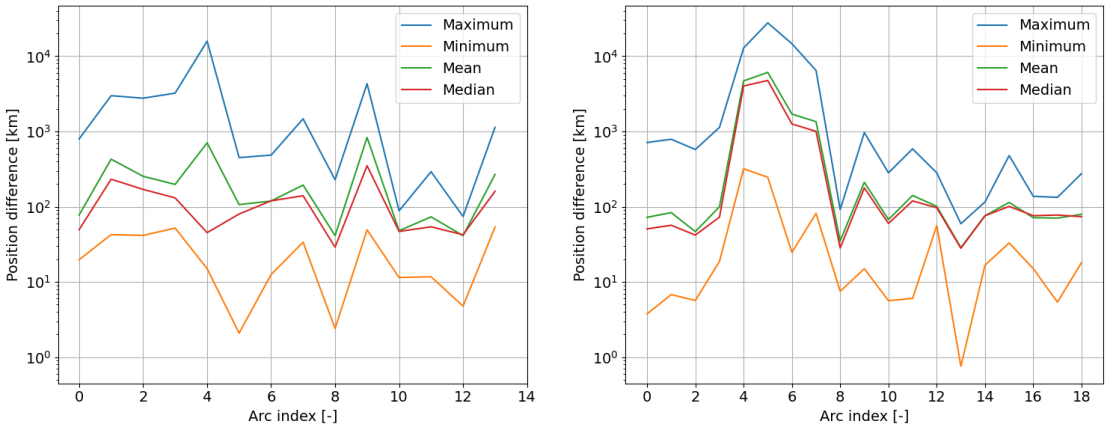

(a) Chang'e 2 **(b)** Chang'e 3

Figure 4.6: Overview of the magnitude of the position difference during the arc overlaps

the two estimated positions varies periodically, with spikes appearing every 12 days in the first case, and every 17 days in the second case. Moreover, the amplitude of the spikes is not constant across the arc overlap, but gets smaller in the second half of both figures. This is likely explained by the fact that the position difference gets smaller near observation data. Indeed, when displaying the times of the observations (dashed lines) on this plot, it appears that the observations are located in the second half of the overlap period, where the magnitude of the spikes is smaller.

In order to be able to get a rapid overview of the behaviour of the position difference over the different arc overlaps, the mean and maximum value of the magnitude of the position difference are computed and plotted in Figure 4.6.

This figure shows that for most of the arc overlaps the behaviour of the maximum, minimum, median and mean of the position difference is comparable. This is not the case however for the overlaps 4-7 of the Chang'e 3 data. The most likely reason for this observation is the fact that the arcs 5 and 6 have much less observation data, along with being located shortly after the lunar close approach of the 16/09/2016, presented in section 3.2. Therefore, it is expected that the error made in those three arcs is significantly larger than in the other ones, and thus the five overlaps in which they are involved also exhibit this behaviour. As for the Chang'e 2 data, the values are less stable, but there are no outliers that show a trend similar to the behaviour seen in the Chang'e 3 case.

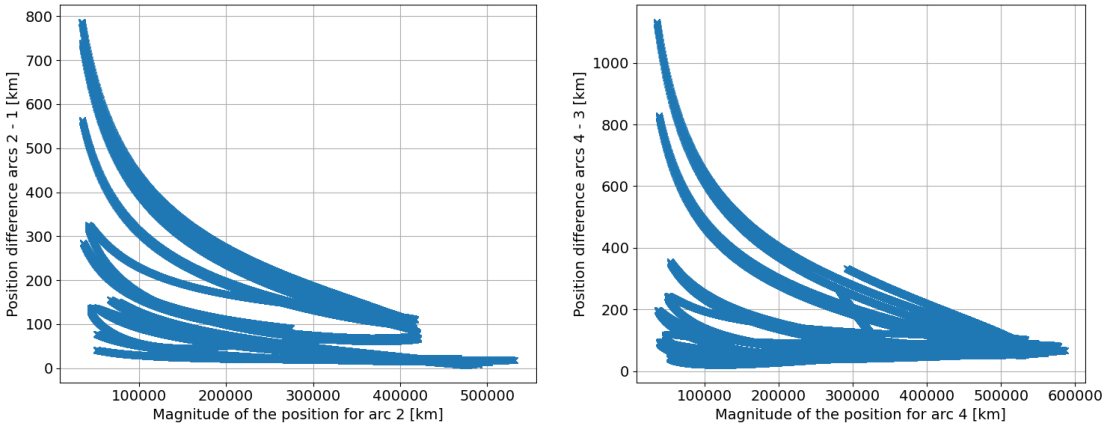

(a) Arcs 1-2 **(b)** Arcs 3-4

Figure 4.7: Magnitude of the position difference in the overlap between two consecutive arcs, plotted against the magnitude of the position of the latter arc.

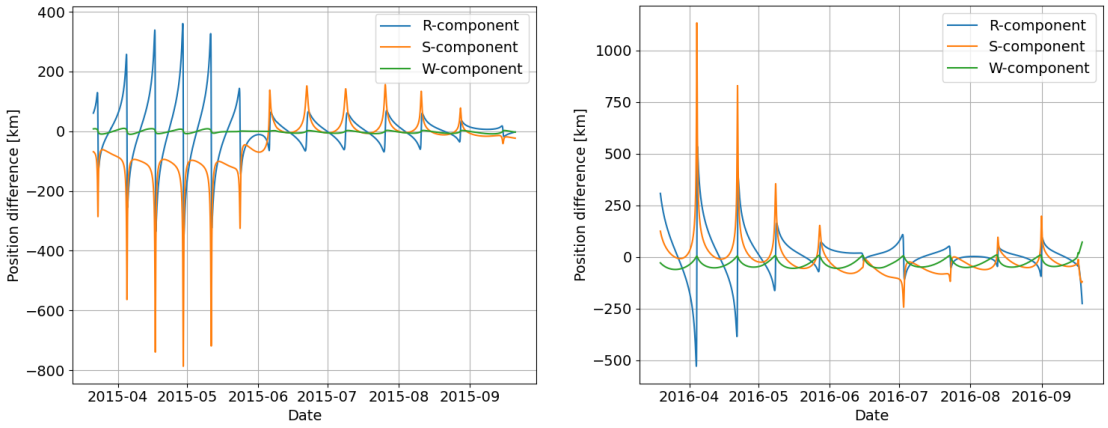

(a) Arcs 1-2 **(b)** Arcs 3-4

Figure 4.8: Position difference in the RSW frame for the overlap between two consecutive arcs

In addition to the trends that can be observed, it is useful to note that the mean and median have almost identical behaviours in the case of Chang'e 3, and very similar ones for Chang'e 2. This indicates that the distribution of the values is rather symmetrical, which in turn shows that the behaviour of the maximum and minimum are not due to extreme outliers, but are indeed a good indicator of the behaviour of the whole distribution. Those two plots thus prove that the behaviour observed in the two overlaps chosen as examples can be generalised to all the overlaps.

In order to gain more information about the position of the spikes in the magnitude of the position difference along the orbit, the magnitude of the position difference is plotted against the magnitude of the position. As the magnitude of the position difference is very small (less than 2%) compared to the magnitude of the position, using the latter for either of the estimated trajectories does not impact the results significantly, and the estimated position from the second arc is used in the plots shown in Figure 4.7. In this figure, it appears very clearly that the points with the largest amplitude for the position difference (i.e. the spikes) are located where the magnitude of the position is the smallest. The conclusion is thus that the spikes in the position difference are located near the periapsis of the orbit.

The position difference is then projected it onto the RSW and TNW frames as described in section 3.4 and the plots presented in Figure 4.8 and Figure 4.9 are obtained. In those figures, it can be seen that the spikes in the magnitude of the difference are still present, but their "repartition" among the three components differs between the RSW and the TNW plot. In particular, the TNW frame allows for a more

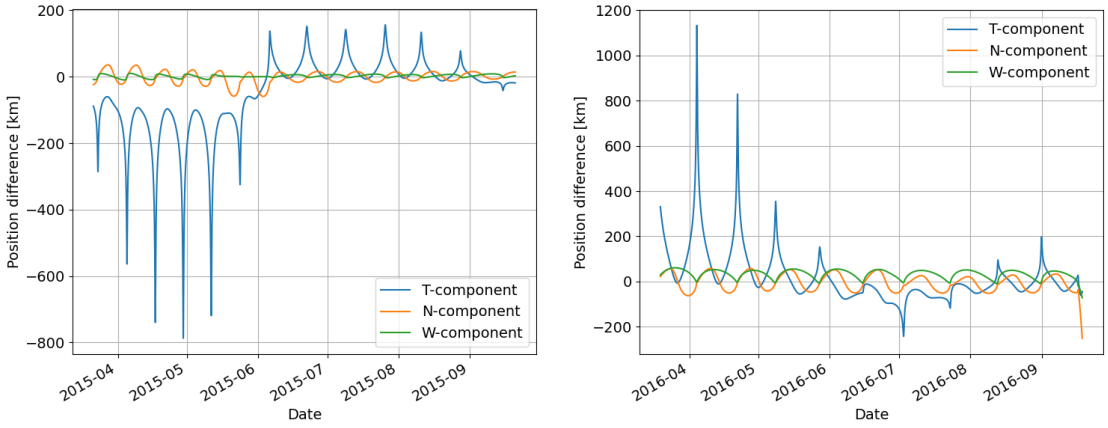

(a) Arcs 1-2 **(b)** Arcs 3-4

Figure 4.9: Position difference in the TNW frame for the overlap between two consecutive arcs

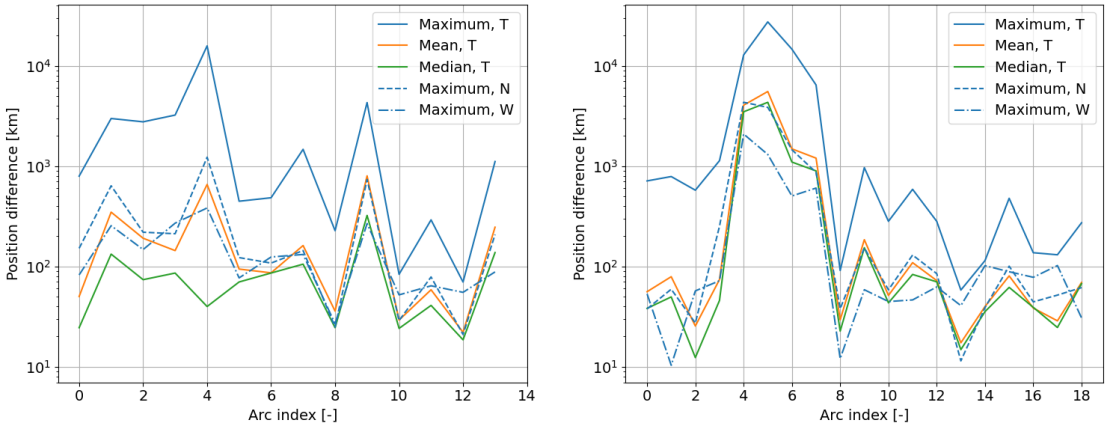

(a) Chang'e 2 **(b)** Chang'e 3

Figure 4.10: Overview of the absolute value of the TNW decomposition of the position difference during the arc overlaps.

convenient decomposition, and further analyses will be conducted on this frame, with more information on the RSW frame being put in Appendix A.

The reason the TNW frame is preferred to the RSW is because only one of the three components exhibits the spikes in its time evolution. In addition to that, the other two components oscillate around zero, but with an amplitude that is smaller than the T component by about one order of magnitude, and with a smooth behaviour. This first indicates that the TNW frame is more adequate for studying the position difference between two consecutive arcs. Indeed, the majority of the difference is manifested in a single direction of the frame, as opposed to two needed in the RSW case. It also represents an additional proof that the difference between the two trajectories is mostly due to an offset in an otherwise very similar trajectory, as the position difference is almost exclusively in the tangential direction. Indeed, a difference in the tangential direction, provided that it is small compared to the scale of the whole trajectory, can be interpreted as one of the estimated positions being ahead of the other, which can also be phrased as an in-track position difference.

In order to ascertain the validity of using the TNW frame for the decomposition of the position difference in the rest of the arc overlaps, the maximum of the absolute value of the three components is plotted for all the overlaps in Figure 4.10, along with the mean and median of the absolute value of the tangential component.

In this figure, it is visible that the maximum of the absolute value of the T component is about one order

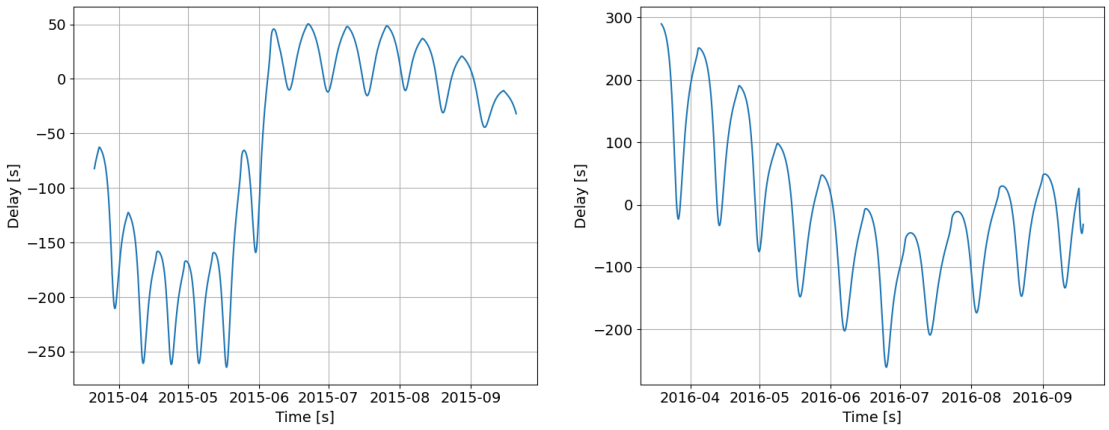

(a) Arcs 1-2

(b) Arcs 3-4

Figure 4.11: Instantaneous delay, computed from the TNW frame of the latter arc

of magnitude above the other two components. In addition to that, the mean and median of the T-component are similar, indicating that the high maximum value is not due to outliers. Those elements put together allow to conclude that the position difference is mostly explained by an in-track difference, and that this result can be generalised to all the arc overlaps considered in this study.

One thing to take into consideration when using the RSW and TNW reference frames is the fact that those frames depend on the Cartesian state of the space object, and thus are different between the two estimated trajectories, as described in section 3.4. However, the impact of using one or the other has been investigated and the results, shown in Appendix A, have proven that this does not have any influence on the conclusions drawn from those plots.

4.2.2. Delay analysis

The next step of this investigation is to look at a possible explanation for the behaviour of the position difference. Therefore, the delay described in section 3.4 is computed and investigated. The reason such a delay bears physical meaning is because the position difference is (almost) exclusively along the tangential component of the TNW frame, and thus the position difference vector is (almost) collinear to the velocity vector. The ratio between the magnitude of the T component of the position difference and the estimated velocity of the object is thus a very good indicator of the time separating the two estimated trajectories. This instantaneous delay is then plotted for the overlap between arcs 1-2 and 3-4, and the resulting plot is shown in Figure 4.11.

In this plot, it can be seen that the instantaneous delay between the two trajectories behaves very differently from the various position differences seen before. Namely, the general behaviour is no longer dominated by large amplitude oscillations (or spikes), but rather seems to be consisting of a general trend with oscillations around the trend. Although the frequency of those secondary oscillations is the same as the one of the spikes present in Figure 4.5 (i.e. the orbital period), the oscillations exhibit a much smoother behaviour compared to the spikes.

Once again, the maximum and the mean of the absolute value of the delay are plotted for all the overlaps, in order to show that the behaviour can be replicated throughout the observation period. The results, shown in Figure 4.12, indicate a similar behaviour as the one seen in Figure 4.6. The metrics are similar over all the overlaps, except for the ones from 4-7 for Chang'e 3 (because of the arcs 5 and 6 that have less data).

This reasoning can be continued further to deduce that the root cause of those variations is likely to be found in the dynamical modelling of the environment. Indeed, whereas the evolution of the position difference is related to orbital effects, with large variations happening near periapsis, the evolution of the instantaneous delay exhibits a different behaviour without any rapid variations in time.

This could for example be explained by a mismodelling of the SRP. Indeed, when using the cannonball

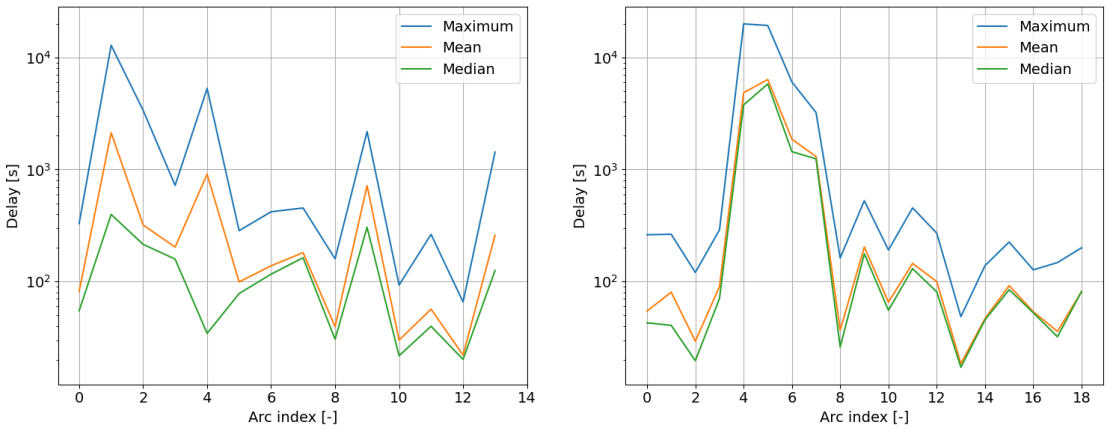

(a) Chang'e 2

(b) Chang'e 3

Figure 4.12: Overview of the absolute value of the instantaneous delay in the arc overlaps

model, over the course of a full orbit the Sun will accelerate the object during the half where it is going away from the Sun, and slow it down during the other half. If two objects are on the same orbit but with a time difference between them, then such a model of the force at the furthest point from the Sun will cause the first object to start slowing down while the other is still accelerated, thus reducing the delay. At the point closest to the Sun, the effect is reversed and the delay increases again, thus explaining the fast oscillations with the same period as the orbit. The slow trend is not as easy to explain, and could arise from various effects in the dynamical model used in this study.

Another potential explanation for this delay can be found when taking into account the fact that the accuracy of the estimation is highly dependent on the quality of the observations, and on the proper treatment of those observations. In particular, timing errors are very common in astronomy observations, and thus a combination of timing errors from different sources could be at play in this situation. Although the observations in the overlap between the two arcs are the same for the two estimations, the rest of the observations differ and could be a part of the explanation for a time shift along the trajectory.

Finally, it is important to keep in mind that this section has investigated the position difference between two trajectories that were fully estimated and propagated using theoretical models, with real observation data used only as an input. As such, the fact that the position difference is in-track indicates that this direction is the least constrained, and the one in which the error is most likely to be concentrated.

Moreover, the behaviour of the delay is completely defined by the simulation settings, with the only external inputs being the estimated initial states. Therefore, if a different force model were to reduce the amplitude of this delay, it would mean that the estimated states are matching each other more closely, which indicates that the force model would be more representative of the reality as it is able to better ”connect the dots”.

4.3. Residual analysis

In this section, the residuals are computed and visualised in the along-track/cross-track plane as described in section 3.5. After discussing the residuals using the most refined weighting scheme presented in section 3.5, the impacts of modifying the settings are discussed. It is found that, despite improving the behaviour of the residuals, the impact of the weighting corrections is minor and other effects are expected to give better results. Finally, two additional methods, observation filtering and bias estimation, are investigated. The estimation setup used throughout this section uses the cannonball radiation pressure model, without including C_r in the estimated parameter vector (settings 1 and 5 of Table 3.2).

The analyses conducted and presented in this section are based on the totality of the arcs considered in section 3.3. However, for clarity purposes details of only two representative arcs have been selected and will be presented here. Those are the arcs 0 and 13 of the Chang'e 3 data. The orbital elements for

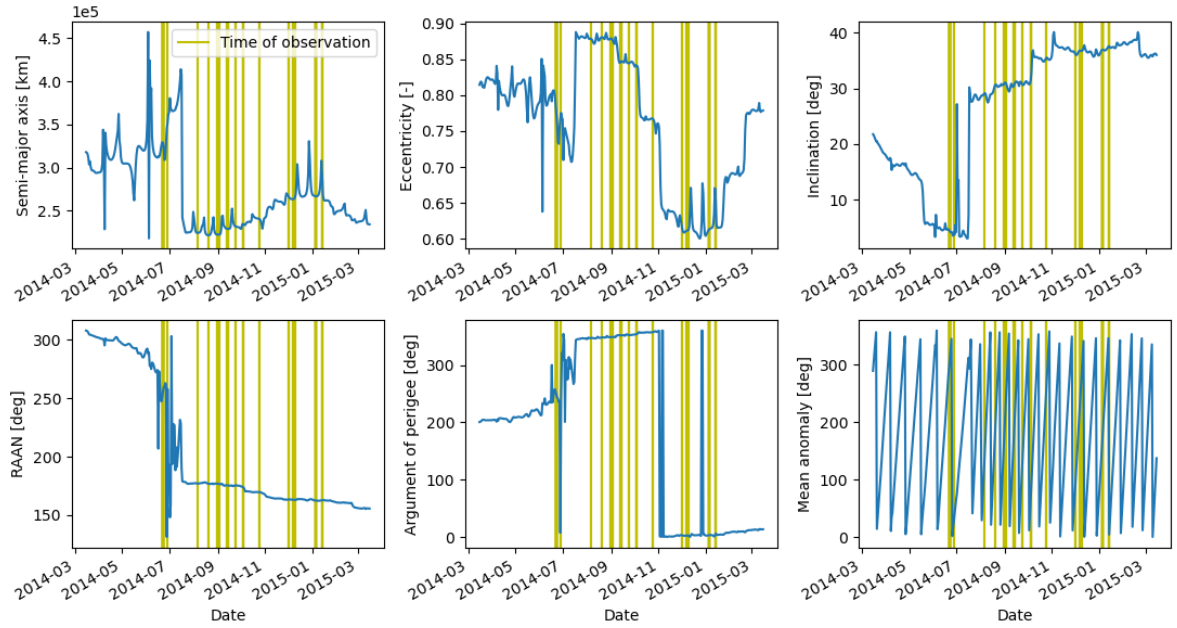

Figure 4.13: Keplerian elements during arc 0 for the Chang'e 3 upper stage

these two arcs can be seen in Figure 4.13 and Figure 4.14. Several plots summarizing figures of merit for all overlaps of both objects will also be presented, and individual figures for each arc are available in Appendix B for a more exhaustive overview.

The residuals are first computed and converted in the along-track/cross-track plane as described in section 3.5. They are computed using setting n° 1 from Table 3.4 and can be found in Figure 4.15. The linear regression used to identify the main direction of the spread, introduced in subsection 3.5.3, is also plotted.

In this figure, it can be seen that there are clusters of residuals belonging to the same ground station (of the same colour). However, the observations of a given station are not all grouped in a single cluster, but rather they are split between different sets of observations. This concurs with the batch weighting of the observations described in subsection 2.4.1.

In addition, it appears that the linear fit is mostly horizontal, thus indicating that the main direction of spread for the residuals is the along-track direction. This confirms that the main biases to take into account have an along-track effect. However, it appears that there are some clusters of observations, such as the green one on the right of the plot for arc 13, that can ”pull” the fit in a way that overvalues the systematic errors of a given ground station, once again showing the importance of adjusting the weights to diminish the relative importance of a large cluster, and indicating that there is potentially more to be done.

4.3.1. Weighting corrections

In order to ascertain the effect of weighting the right ascension observations according to the declination value, as presented in subsection 2.4.1, this weighting correction is turned off (setting n° 2 from Table 3.4). The updated residuals for the two example arcs can be found in Figure 4.16.

On this plot no significant difference can be found when comparing to Figure 4.15. This seems to indicate that, while more realistic and physically accurate, the adjustment of the right ascension weights according to the value of the declination does not have a significant impact on the residual distribution.

Then, the effect of the batch weighting are investigate by turning this correction off (setting n° 3 from Table 3.4) and the residuals are re-computed. The resulting residuals after conversion in the along-track/cross-track plane are shown in Figure 4.17.

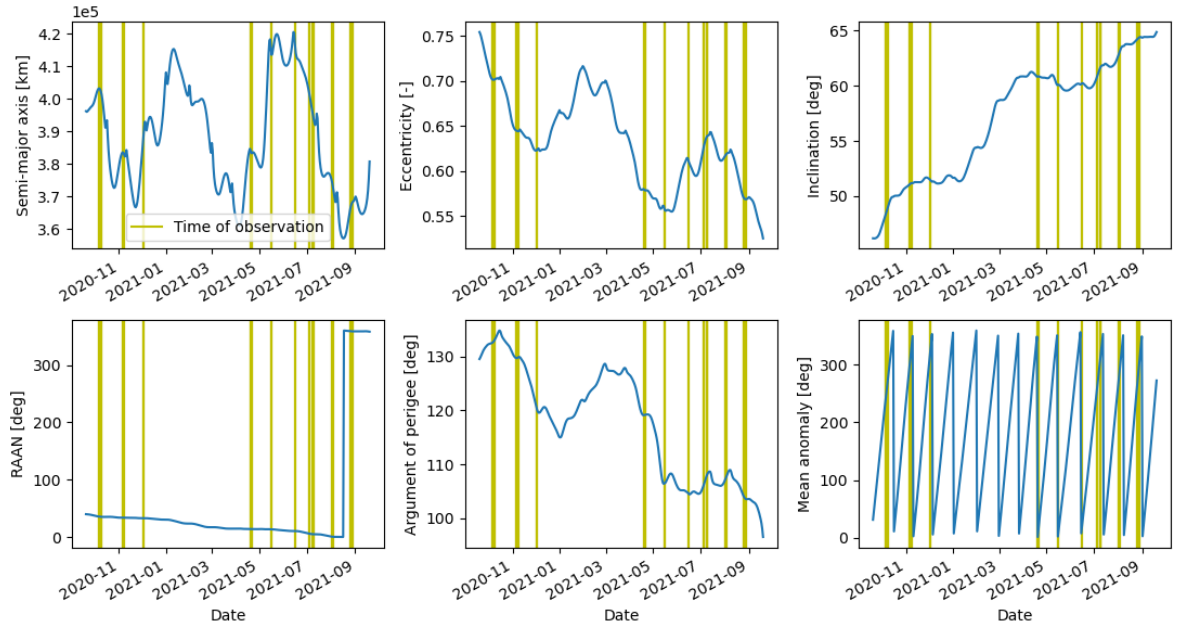

Figure 4.14: Keplerian elements during arc 13 for the Chang'e 3 upper stage

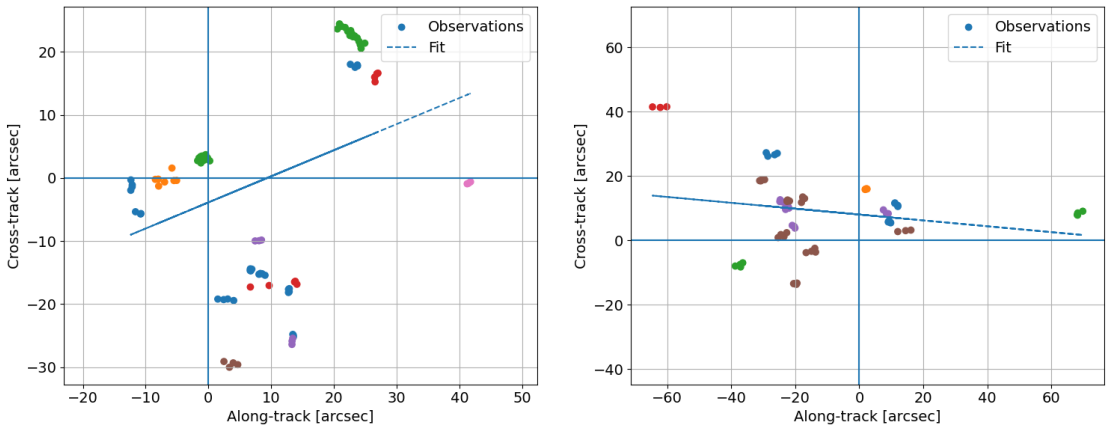

(a) Arc 0 **(b)** Arc 13

Figure 4.15: Residuals computed using setting n° 1 plotted in the along-track/cross-track plane, colours correspond to different ground stations

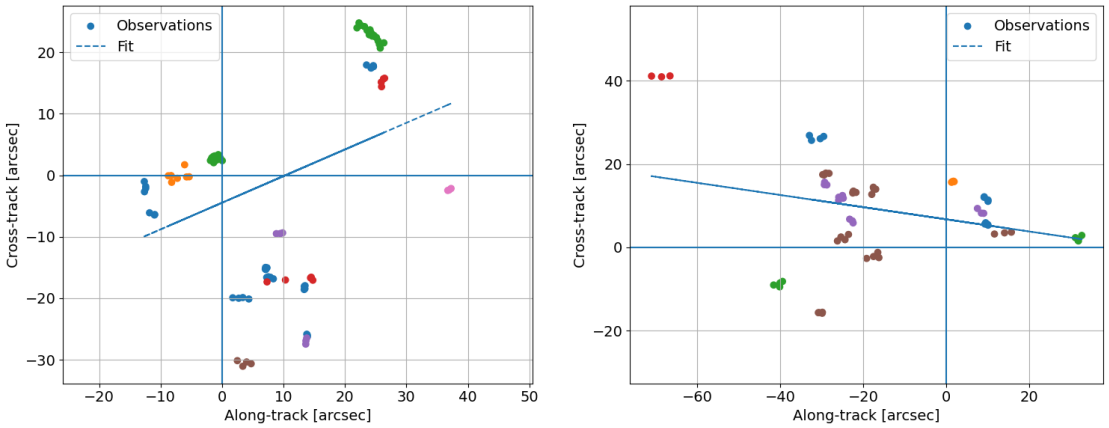

(a) Arc 0 **(b)** Arc 13

Figure 4.16: Residuals computed using setting n° 2 plotted in the along-track/cross-track plane, colours correspond to different ground stations

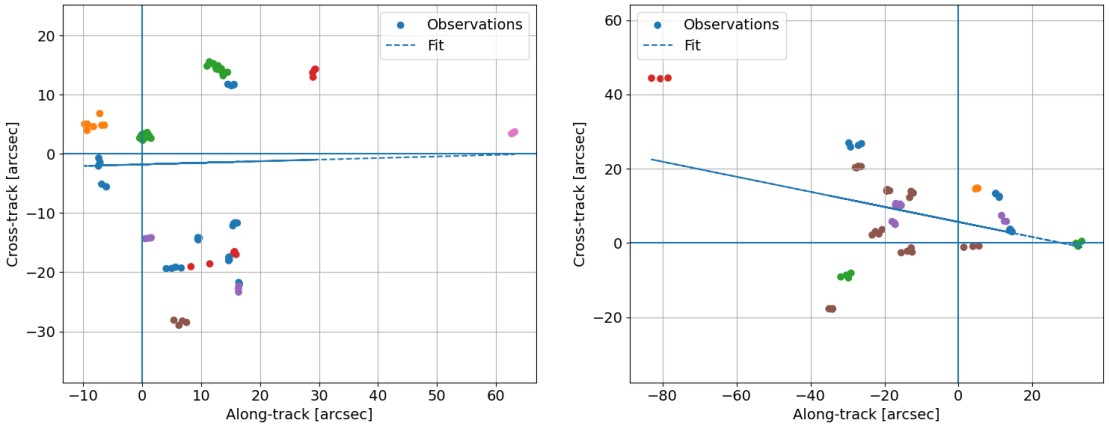

(a) Arc 0 **(b)** Arc 13

Figure 4.17: Residuals computed using setting n° 3 plotted in the along-track/cross-track plane, colours correspond to different ground stations

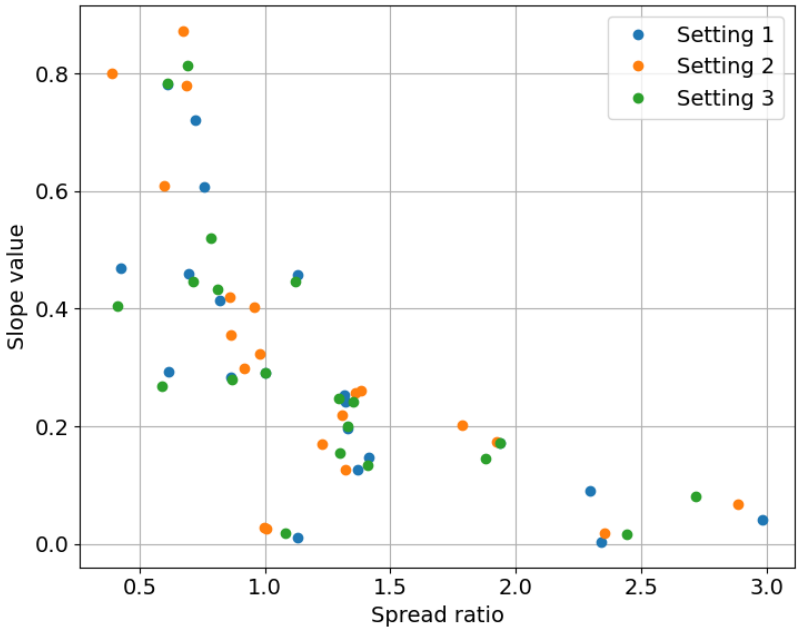

Figure 4.18: Slopes absolute values vs spread ratio

In this figure, two main differences can be seen compared to Figure 4.16. The first is that the linear regression leads to a more horizontal slope, which indicates that the main direction of the residual distribution is getting closer to purely along-track. The second difference is that the overall spread of the residuals is reduced. This can be seen by noticing that the plot in Figure 4.16 is more ”zoomed in” than the one in Figure 4.17. Such a result is, however, not as important for arc 13 as it is for arc 0.

Those results indicate that the batch weighting, as opposed to the right ascension weighting, does impact the residuals. Moreover, this impact is an improvement because it reduces both the overall spread of the residuals, and the discrepancy between the along-track spread and the cross-track one.

One possible explanation for the different effects of the two weighting corrections studied is that the batch weighting process impacted mostly the along-track direction, while the right ascension weighting process affects the trust in the right ascension observation, which does not reflect on a specific direction in the along-track/cross-track plane.

As explained in section 3.5, the comparison of the plots for all the arcs one by one for the three settings used in this study would be a tedious and inaccurate process, considering that visual comparison of two figures by a human is not the most reliable method. Therefore, the slopes of the linear regression presented in subsection 3.5.3 can be plotted, and in order to include their relevance, they are plotted against the spread ratio of the residuals.

The results are computed for each of the three possible weighting settings, and the resulting plot is shown in Figure 4.18. In this figure the most obvious trend is the fact that the absolute value of the slope decrease as the spread ratio increases.

This is logical as a higher spread ratio means that the residuals are more elongated in the along-track direction, and thus the absolute value of the slope is small. Moreover, the absolute values of the slopes are all below 0.8. Since a slope value of 1 or -1 indicates a main spread at an angle of 45°, or exactly between the two directions, the fact that the slopes are all below this threshold shows that the main direction of the spread is always closer to the along-track axis than the cross-track axis. In conclusion, the residuals are overall more spread in the along-track direction, even with the refined weighting scheme.

Finally, in order to extend the comparison between the three weighting settings used in this section, an overview of the RMS of the in- and out-of-sample residuals is presented in Figure 4.19 and Figure 4.20.

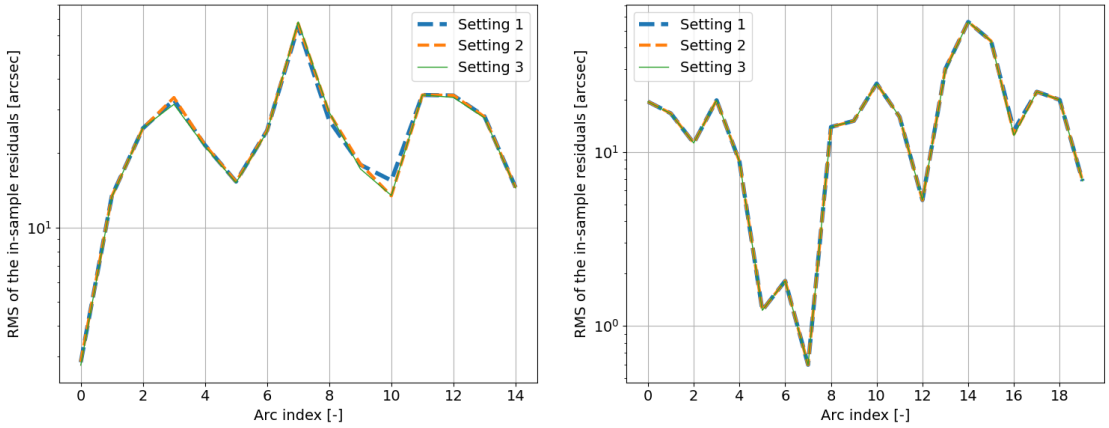

(a) Chang'e 2 **(b)** Chang'e 3

Figure 4.19: RMS of the in-sample residuals

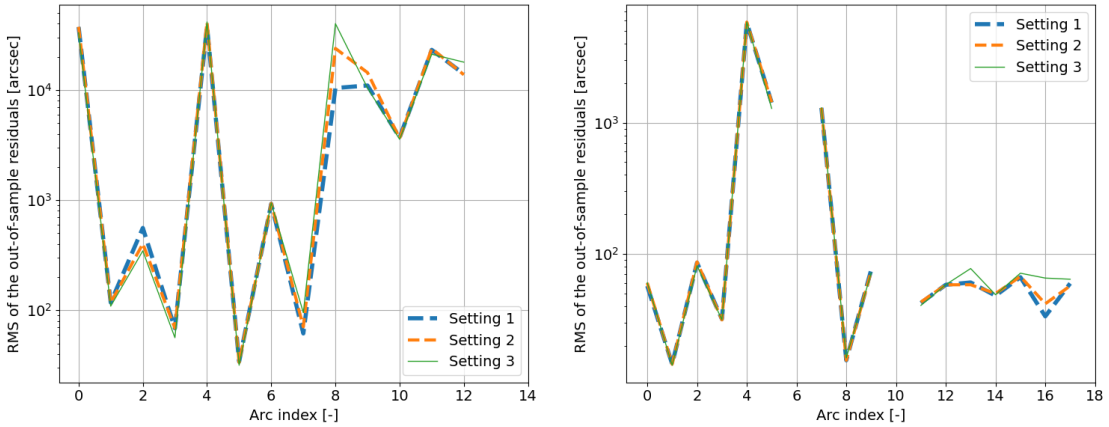

(a) Chang'e 2 **(b)** Chang'e 3

Figure 4.20: RMS of the out-of-sample residuals

In the OOS plot, it can be noted that two arcs for Chang'e 2 (n° 13 and 14) and two for Chang'e 3 (n° 6 and 10) do not have data points. This is caused by the fact that in the 6-month period following the end of their arc there are no observations, which means that no residuals can be computed with this out-of-sample period.

The main conclusion that is drawn from those plots is the fact that the RMS of the residuals is almost identical using the three weighting settings, indicating that the improvements noted earlier are minor. However, for arc 9 of Chang'e 2 and arcs 13 and 16 of Chang'e 3, there is a clear improvement of the OOS residuals when including the batch weighting (setting 2 vs 3), and except for arc 13 of Chang'e 3 the right ascension weighting further reduces the RMS of the OOS residuals (setting 1 vs 2).

An opposite effect can be observed for Chang'e 2 in the IS residuals of arc 10 and the OOS residuals of arc 2. In those cases, the most refined weighting scheme does not perform as well as the other two. This effect is, however, smaller than the improvements noted above.

Those results indicate that the corrections applied to the weighting scheme do allow, in certain conditions, to reduce the values of the residuals. However, this reduction is far from systematic and has a very small amplitude, which indicates that the main origin for the residuals is not the observation weighting, but something else. Both weighting corrections should still be included as they overall reduce the residuals more than they increase them.

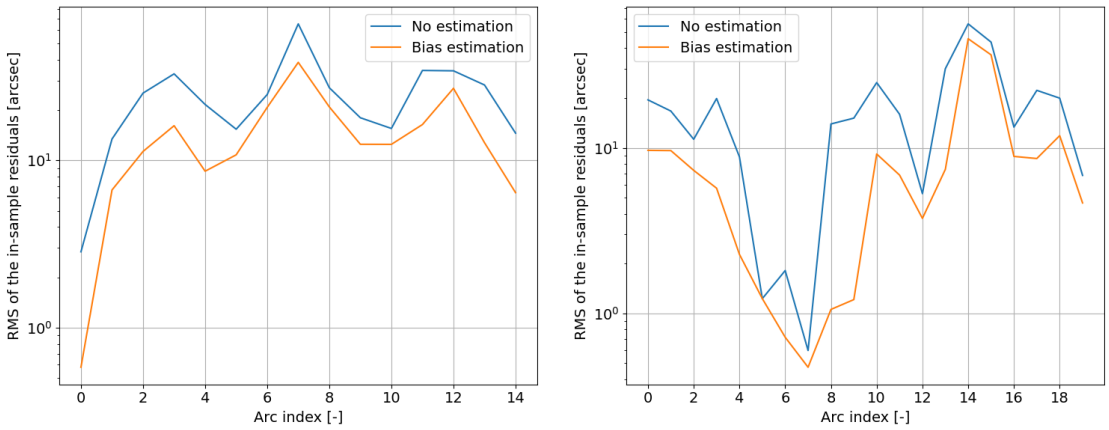

(a) Chang'e 2

(b) Chang'e 3

Figure 4.21: Residuals with the ground station biases included in the estimated parameters

4.3.2. Additional methods

In addition to the new weighting schemes, two other options have been investigated. The first one was to filter the outlier observation as described in section 3.5. This process only led to 9 observations being filtered for the whole 10-year period of the Chang'e 3 observations, and all those observations were during the arcs 14 and 15, that happen right after a gap in the data. No observations were filtered for the Chang'e 2 data. Filtering more points is possible by reducing the threshold of the filter but then the filtered residuals are less outliers, and the estimation process becomes less stable, increasing the OOS residuals.

The second option is to estimate the right ascension and declination biases for each station and for each arc using the settings described in section 3.1 (n° 5 of Table 3.2). The effect of this process on the in-sample residuals is shown in Figure 4.21.

In this figure, the results are very clear: including the observation biases in the estimated parameters does allow for a better fit of the observations over every arc considered in this study. Moreover, this improvement of the residuals is more significant than the differences observed in the weighting scheme corrections. This indicates that the effect of observation biases is larger than the improper weighting, and thus should be higher on the list of effects to correct for.

There is however one important thing to keep in mind, as only the IS sample residuals have been analysed for the bias estimation (as explained in section 3.5). Indeed, including the observation biases in the estimated parameter vector adds a considerable amount of degrees of freedom for the estimator, as there are often at least 5 different ground stations providing observations during a single arc. This means that the number of values to estimate goes from 6 to 16, thus more than doubles. A potential consequence of this high number of adjustment variables is that the estimation process returns a trajectory that over-fits the data in-sample, and diverges very quickly once out-of-sample. Therefore, in order to confirm the added value of estimating the ground station biases, an analysis on the OOS residuals would be required in future studies. As stated before, such an analysis would have to find a way to either compute the residuals for ground stations that have no estimated biases (using default values), or to exclude the observations from those ground stations from both the baseline residual computation and the ”improved” one.

In conclusion, this section has shown that it is possible to slightly improve the residuals on average by using a refined weighting scheme compared to the uniform weighting used in Table 3.4. Filtering the observations has proven to cause only a few excluded data points, and thus is not considered to be significant in this situation. Finally, estimating the observation biases of the ground stations leads to reduced in-sample residuals. The validity of such a process needs to be investigated further to verify if the trajectory is indeed better, or if a high number of parameters allows the estimator to over-fit the data.

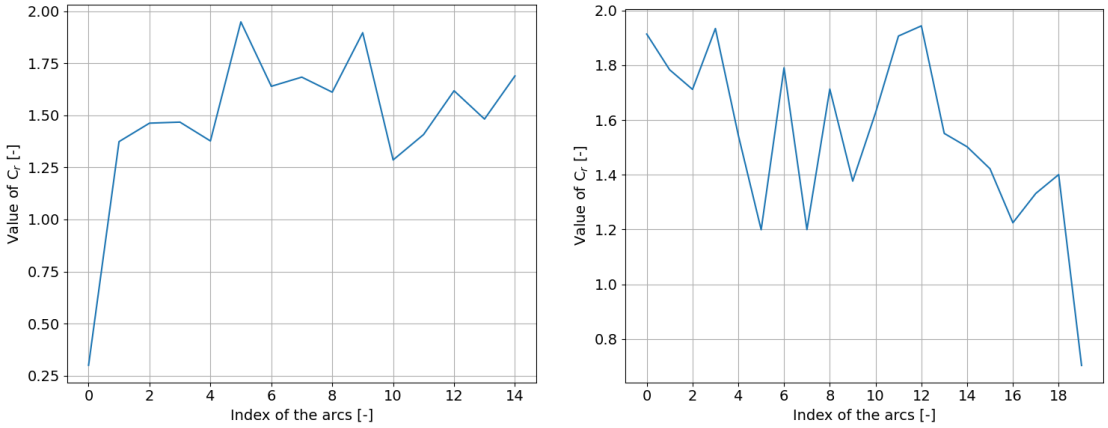

(a) Chang'e 2 **(b)** Chang'e 3

Figure 4.22: Estimated values of the C_r parameter

4.4. Use of the three constant model

After implementing the TCM, it has first been validated and the a priori covariance parameters have been tuned to the values presented in section 3.1. Those values were chosen to prevented the estimated parameters from blowing up to absurd values, as described more in detail in Appendix C. Once these steps have been taken, the first analyses can be performed with the TCM in place. The residuals, both in- and out-of-sample, are compared when implementing the TCM, and the instantaneous delay from section 4.2 is also used to evaluate the performance of this model. Finally, the cumulative impact of estimating the observation biases described in subsection 2.3.1 with the various SRP configurations is studied.

4.4.1. Model results

Four different settings (n° 1-4 from Table 3.2) are used, and the values for the estimated parameters are shown in Figure 4.22 and Figure 4.23. As explained in subsection 2.3.1, the values for the physical characteristics of the Chang'e 2 and 3 upper stages might not be accurate, but the errors in those parameters are absorbed by the estimation process. For instance, in the cannonball model expression given in section 2.2, if the value taken for A is half of the real value, then the estimation process will yield a value for C_r that is twice the real value. This, however, does not change the values of the residuals beyond potential numerical rounding errors.

More specifically, in this study, it can be computed from the numbers given in subsection 2.3.1 that the A/m ratio used in the estimation is smaller than the one using the corrected values. As a result, the estimates for C_r are expected to be above the "correct" estimate. This is coherent, as the values present in Figure 4.22 are mostly above 1.5. Since C_r is expected to be between 1 and 2, real values could very well be lower than the current estimates. However, it is important to note that as no information was acquired regarding the material used, the main conclusion that can be drawn from this figure is the fact that the values are comprised within the physically acceptable range for C_r. There are two exceptions to these boundaries, namely the first arc of Chang'e 2 and the last arc of Chang'e 3. Those arcs are located at the edges of the estimation periods, and thus it is logical that the estimation process leads to less physically meaningful values. Therefore, the conclusion that the C_r estimates are in the correct neighbourhood is not invalidated by those two outliers.

As for the TCM parameters, only the mass of the object experiencing the force appears in Equation 2.13. Therefore the mismodelling of the surface area does not impact the values of the parameters. Given that the mass used in the estimation was likely larger than the real mass of the upper stages, it can be assumed that the actual values of the TCM parameters are lower than the estimated values presented in Figure 4.23. Since those parameters do not, however, convey a direct physical meaning, it is not possible to continue the analysis to verify whether smaller values would be more reasonable.

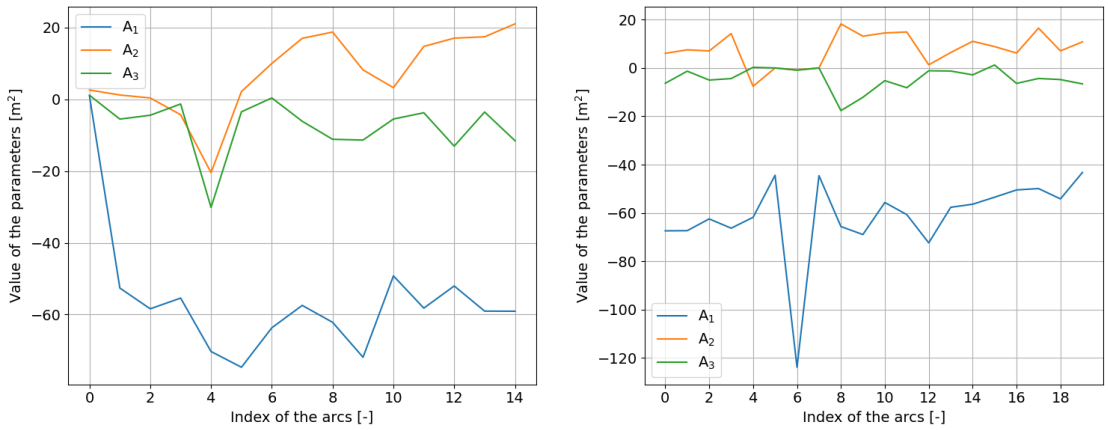

(a) Chang'e 2 **(b)** Chang'e 3

Figure 4.23: Estimated values of the TCM parameters

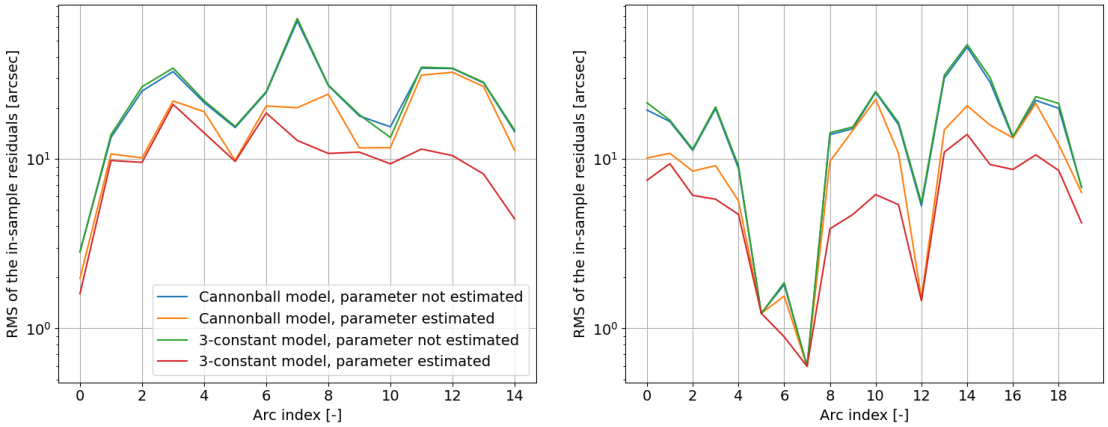

(a) Chang'e 2 **(b)** Chang'e 3

Figure 4.24: RMS of the IS residuals for the different SRP configurations

4.4.2. Model comparison

In order to have a global visualisation of the residuals evolution without comparing the residual plots of all the arcs for all the different settings, the RMS of the IS residuals is computed for each arc, its evolution is plotted over the different arcs. The resulting plots are shown in Figure 4.24.

In this figure, it can first be observed that the curves obtained for both SRP models without estimating the parameter(s) are almost perfectly superimposed. This is an additional proof that not only the TCM implementation is adequate, but also that the default value selected for the parameter manages to imitate the cannonball model very accurately. As a consequence of this result, the cannonball model without estimation will be used as the baseline in the future analyses, while the TCM without estimation will be omitted in order to reduce the amount of information on a single figure.

A second observation is that for all the arcs the order between the three setups (baseline, cannonball estimated, TCM estimated) is the same, with the residuals for the baseline being the largest, then the residuals of the cannonball model with the parameter estimated, and finally the TCM with the parameters estimated with the lowest residuals. This is a very promising result as it indicates that the TCM performs better than the cannonball model inside the estimation window. Moreover, the fact that both models perform better than the baseline when estimating the parameters is coherent, and a good indication that the estimator is working as it should.

In order to verify the performance of the TCM on the prediction part of the orbit determination process,

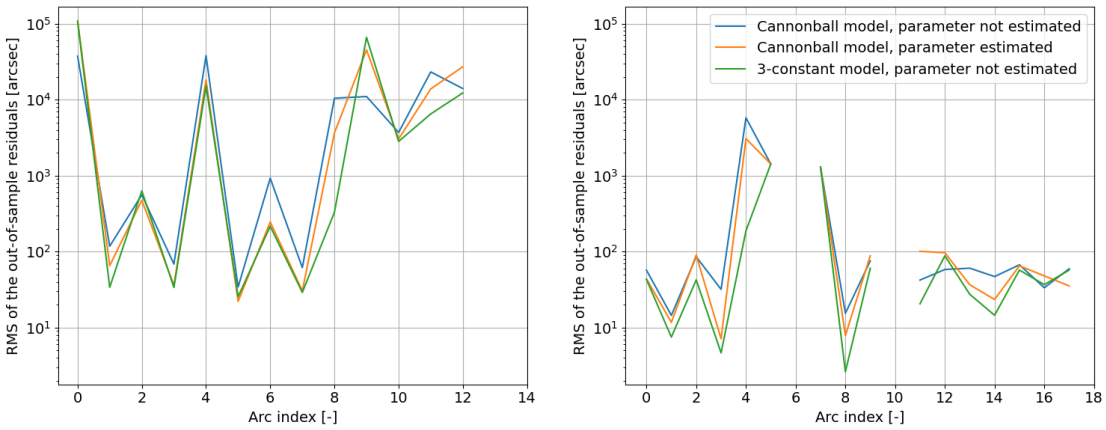

(a) Chang'e 2

(b) Chang'e 3

Figure 4.25: RMS of the OOS residuals for the different SRP configurations

the RMS of the residuals is then computed on a 6-month out-of-sample period, for the three setups, and the results are shown in Figure 4.25. On those plots, four arcs (n° 13 and 14 of Chang'e 2 and n° 6 and 10 of Chang'e 3) do not have data points. This is caused by the fact that in the 6-month period following the end of their arc there are no observations, which means that no residuals can be computed with this out-of-sample period.

This figure shows that once again in almost all the arcs the baseline performs the poorest, then the cannonball model with C_r being estimated, and finally the TCM with its parameters estimated performs the best. The only exceptions are arcs 0, 9 and 12 of Chang'e 2 and 11, 12 and 16 of Chang'e 3. However, in arc 12 of Chang'e 2 and 11 of Chang'e 3 the TCM still has the lowest RMS of the residuals, notably being better than the baseline. In arcs 0 of Chang'e 2 and 12 and 16 of Chang'e 3 it is the baseline that is performing the best, but the difference with respect to the other two configurations is quite small compared to the arcs where the TCM is performing the best. Finally in arc 9 of Chang'e 2 the TCM is performing worse than the baseline, with a difference of the same order as the improved times.

It is however performing almost the same as the estimated cannonball model, which indicates that the issue is probably coming from the fact that arc 9 is ending on the 03/08/2019, at the same time as two lunar close approaches. Indeed, the Chang'e 2 upper stage experiences two lunar close approaches on 19/04 and 12/06/2019 (as seen in section 3.2), and there are no observations between those close approaches and the end of the estimation window for arc 9. As such, the OOS period is significantly harder to predict, due to the perturbing effect of a lunar fly-by on the dynamics. This shows that the TCM is performing better also outside of its training dataset, which shows that the good performance exhibited in Figure 4.24 is not due to over-fitting but indeed to a better modelling of the trajectory, that results in a better predictive power for the evolution of the space object in the future.

Another result to put in regard to the beginning of this study is to compute the instantaneous delay from subsection 4.2.2 with this improved dynamical model. The resulting comparison between the maximum and the mean of the absolute value of the delay for all the arc overlaps considered is shown in Figure 4.26 and Figure 4.27.

In these figures, it can be seen that for Chang'e 2 the instantaneous delay is reduced compared to the baseline model in some of the arcs, but not in all. Mainly, in the final arc overlaps (9-14) the baseline performs better than the refined dynamical model. This is likely due to the fact that this period is the end of the observation window for the Chang'e 2 upper stage. At this time the dynamics are harder to predict, as the two jumps in the orbital elements seen in section 3.2 show. In the rest of the arcs, the TCM performs mostly better than the baseline except in two arcs (1 and 4), but even then the difference is small compared to the arcs where it performs better. For Chang'e 3, the results are clearer, with the TCM results being better than the baseline in every overlap except n° 12 and 17. In the case of overlap 17 it is only worse when looking at the maximum of the delay, but when looking at the mean the TCM

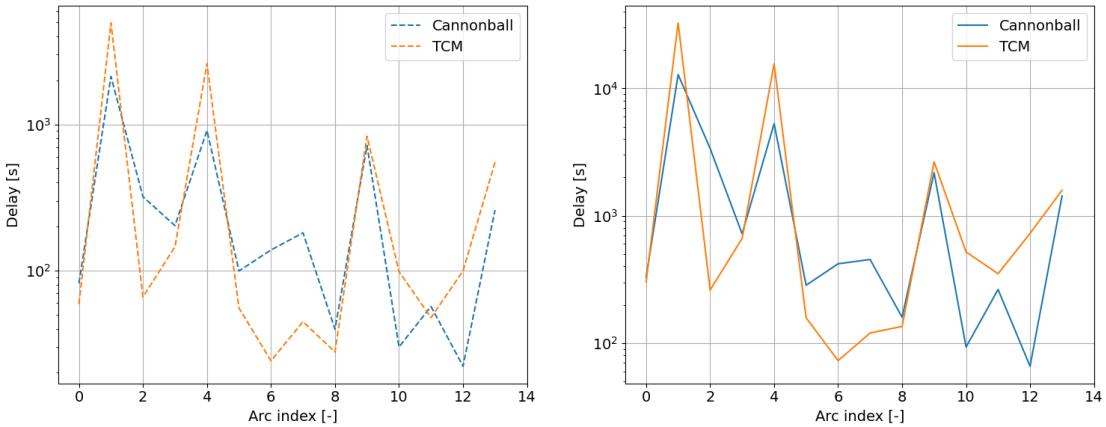

(a) Mean **(b)** Maximum

Figure 4.26: Comparison of the maximum and mean of the absolute value of the instantaneous delay between the baseline and the TCM SRP for Chang'e 2

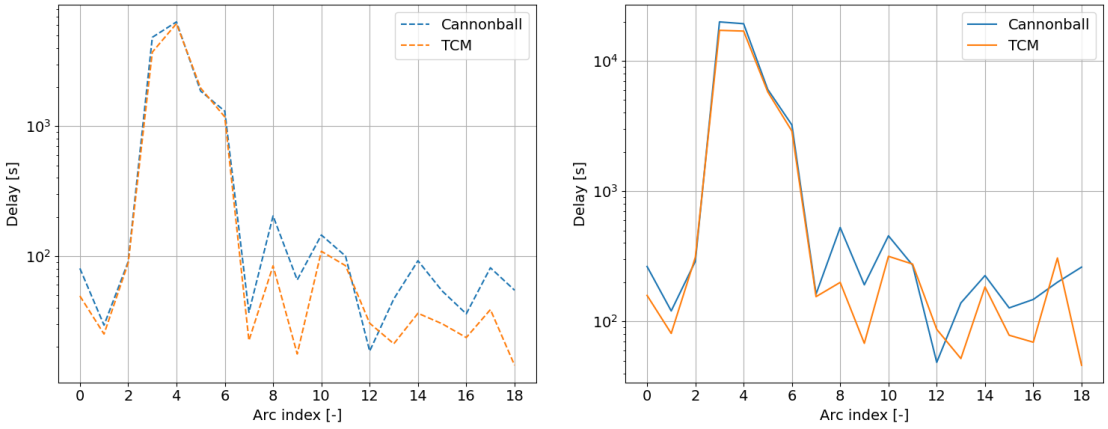

(a) Mean **(b)** Maximum

Figure 4.27: Comparison of the maximum and mean of the absolute value of the instantaneous delay between the baseline and the TCM SRP for Chang'e 3

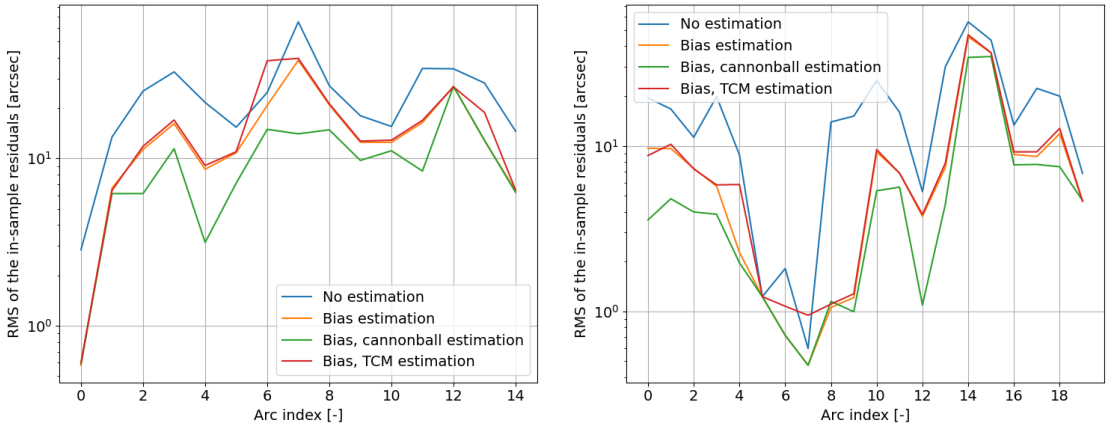

(a) Chang'e 2

(b) Chang'e 3

Figure 4.28: RMS of the IS residuals when estimating the observation biases for the different SRP configurations

performs better. As for overlap 12, the difference w.r.t. the baseline is once again small compared to the times the baseline is worse. Overall, this indicates that using the TCM with parameter estimation is a better default dynamical model than the baseline. It can, however, lead to slightly worse predictions in the case of complicated dynamical changes (e.g. lunar close approaches).

4.4.3. Impact of estimating the observation biases

Finally, the impact of adding the observation biases to the estimation with the three SRP configurations considered (baseline, cannonball with C_r estimated, TCM with parameters estimated) is investigated. The in-sample residuals are computed for the settings 1 (baseline), 5, 6 and 7 of Table 3.2. The results are shown in Figure 4.28.

In this figure, it can first be seen that the baseline (cannonball model, no parameters estimated) almost always performs the worst. Two arcs (6 of Chang'e 2 and 7 of Chang'e 3) do not exhibit this behaviour but the difference is small. However, the settings that perform the best on all the arcs considered without exception is setting 6, where the biases are estimated, but the SRP model used is the cannonball model and not the TCM. This result is quite surprising at first, as the TCM was performing better than the cannonball model previously. Moreover, since the TCM is an extension of the cannonball model, the residuals should always be lower when using the former, as it gives more freedom to the estimator.

There are at least two reasons that can explain the order observed in Figure 4.28. The first is that the residuals that are minimised by the estimator are weighted according to the weights matrix defined in subsection 2.4.1. The RMS on the other hand was computed giving all the residuals the same weight, which means that the residuals that the orbit determination process is minimising are not exactly the same ones that are plotted. This would explain why a setting with more parameters could lead to a higher value for the RMS of the IS residuals. Another possibility is that adding the observation biases to the TCM gives "too much" freedom to the estimator, and the estimated trajectory is in a local minimum of the cost function, but not the global minimum. Such a phenomenon relies on the existence of local minima in the neighbourhood of the "real" trajectory, which is not very typical of orbital dynamics, but the high non-linearity of the dynamics in this study could allow for their existence.

Finally, the same caution that was described in section 4.3 should be observed here, as only the IS residuals were analysed. The risk of over-fitting the trajectory, as described in subsection 2.3.2, is thus quite high with the increased number of parameters. As a consequence, further analyses would be needed before considering that this setting is suitable for determining the orbit of cislunar space object. Those analyses would ideally study both the OOS residuals and the arc overlap (position difference and instantaneous delay) to verify the quality of the estimated orbit.

5

Conclusions and recommendations

5.1. Conclusions

The present study has investigated different ways to improve the performance of an existing framework for the orbit determination and propagation of objects in cislunar space, more specifically upper stages of lunar missions. The framework, originally started and presented in [Witte 2024], has been implemented using the open-source Tudat software, developed in the TU Delft [Dirkx, Marie Fayolle, et al. 2022]. The present study carried out estimations on longer periods of time and with more data points than [Witte 2024], reducing the need for external inputs. Those external inputs are taken from the Find_Orb software, that performs initial orbit determination.

Firstly, a bootstrapping method has been implemented for providing the initial guess required by the orbit determination process. This method has allowed to increase the portion of the total observation window that is covered by the estimation process compared to [Witte 2024]. In addition, the reliance on external guesses has been reduced. This is a progress because it has been concluded in [Witte 2024] that the trajectories provided by Find_Orb are not as accurate as the results of the orbit determination described in the present work.

In order to identify the main source of error in the estimation and prediction process, different estimations of the same period of time were then conducted using partially overlapping datasets. The difference between the estimated trajectories was used as an indicator for the minimum true error that comes from using this estimation framework. The mean values for the magnitude of the position difference were found between 10^2 and 10^4 km. The position difference was then thoroughly analysed in order to partially quantify the error, identify its origin, the cause for its evolution, and potential solutions to reduce it. It was found that the error is mostly along-track, and can be well explained by the presence of a time offset, or delay, between the estimated trajectories. This delay was found to have a mean value between 10^2 and 10^4 s across the different arc overlaps considered in this study. Two main origins for such a delay have been proposed, namely a dynamical origin and an observational origin. In the dynamical origin case, the delay is thought to be caused by an improper modelling of the environment, especially the SRP. This explanation is considered likely because the effects of mismodelling the SRP would lead to similar effects as the ones that are observed. As for the observational origin, the source of the delay is then attributed to the imperfect nature of the observations, especially when it comes to timing errors.

Once this analysis had been performed, a more in-depth investigation of the residuals and astrometric observations was conducted. The typical order of magnitude of the residuals was 10 arcsec. In order to gain insight on the correlation between the orbital behaviour and the residuals, the latter were converted into the along-track/cross-track frame. It was then found that they were mostly spread in the along-track direction. Such a result indicates that the along-track direction is less closely fitted during the orbit estimation process, which is coherent with the delay that was previously found.

In order to improve the treatment of the observations a refined weighting scheme taking into account the

amount of observations produced in a batch, as described in [Farnocchia et al. 2015], was implemented. It also included a correction for the correlation between right ascension and declination observations and a filter for outlier observations. It did not, however, lead to significant improvements in the quality of the estimated trajectories. This result indicates that the main source of uncertainty is not due to the weighting, but that other aspects have a more significant impact.

As a part of the investigation on the treatment of the observations, right ascension and declination biases were estimated for the different ground stations providing observations. The results of including those biases in the estimation were rather positive, leading to significantly reduced residuals in-sample. This should, however, be taken with precaution as the analysis has not been extended to the out-of-sample period. Therefore, it is possible that the trajectory resulting from this new estimation is over-fitting the observation data and would not be useful for prediction purposes.

Finally, another domain of interest for improving the estimation process that was investigated is the dynamical modelling of the environment, and more specifically the solar radiation pressure force. This work has identified and implemented a new model, described in [McMahon and Scheeres 2015], more refined than the cannonball model that was previously used. It was first tested and validated in order to ensure that its implementation matched its theoretical behaviour, and its parameters were tuned so that the default values matched the cannonball model. With this new model, both the estimation (in-sample residuals) and the prediction (out-of-sample residuals) were improved, indicating that it is better suited to the cislunar context than the cannonball model. The RMS values of the IS residuals were reduced by up to a factor 3, while the RMS of the OOS residuals went down by factors 2-20 in most cases. Finally, it was found that the TCM was leading to improvements in the delay previously computed, although those improvements were not as consistent as the decrease in the residuals values.

From all those results, the research questions can now be answered:

1. **How much can the scope be extended, and what external inputs are required for the estimation to be performed?**
   The scope of the estimation has been extended to the major part of the observation period for the Chang'e 2 upper stage, and to the whole extent of the observation period for Chang'e 3. Moreover, the number of external inputs required is drastically reduced, going down to 1 in the case of the Chang'e 3 upper stage, and 2 for the Chang'e 2 one.
2. **What is the main source of error in the estimated trajectories?**
   The true error being, by definition, not obtainable, the position difference in the overlap between two consecutive arcs has been used as a lower bound and an indicator. It has been found that the main direction of the error was the along-track direction, and that the evolution of this error over time was best explained by a time difference between the estimated states. It can thus be safely assumed that the main source of error is also a wrongful positioning of the estimation on the orbit, but that the shape of the orbit is otherwise accurate. Two effects that could cause such an orientation of the error are an improper modelling of the SRP and the presence of timing errors in the observations.
3. **What is the impact of refined treatment of the observations and residuals on the performance of the estimation?**
   The observations modelling and treatment has been refined, through adjusting their weights, filtering outlying observations, and estimating the ground station biases. Although the first two processes did not lead to a significant improvement in the quality of the estimation, the estimation of the biases reduced significantly and consistently the residuals. This result, while promising, should be considered with caution as it could be caused by over-fitting the data.
4. **How does a new solar radiation pressure model impact the quality of the orbit determination process?**
   A new SRP model has been implemented, and it has been found that the TCM is able to perform better than the cannonball model both in-sample and out-of-sample. Moreover, the inclusion of this model reduces the position difference in the arc overlaps and thus improves the overall quality of the estimation. The improved results of this process can reach a factor 20, and are typically between 2-3 times better than the baseline.

5.2. Recommendations

Taking the present work's results into account, some recommendations can be given for future investigations:

- Although this study used multi-arc orbit determination methods to perform analyses over the whole observation periods rather than specific windows, the constrained version of this process was never implemented. Such a method, described in [Lari and Milani 2019], or at least a more global version of the classical multi-arc one, could allow to define global parameters, such as the SRP parameters, to be estimated, thus leading to more physically coherent results.
- The impact of including the ground station biases in the estimated parameters has been shown to reduce the values of the in-sample residuals, but further analyses on the out-of-sample residuals should be performed. Those would allow to evaluate how much of the improvement is due to over-fitting the observation data, and how much is actually resulting in a better trajectory that is suitable for predictions (namely regarding potential collisions).
- In order to bring this work closer to real-life applications, orbit determination and prediction need to be supplemented with an uncertainty propagation method, as it is the required output to determine the probability of collision with a given object during a mission. The Gauss-von-Mises method described in subsection 2.4.3 seems to be a promising solution that should be investigated in future studies.
- Although the use of the TCM has already significantly improved the quality of the orbit estimation, this model is not directly correlated to actual physical phenomenons. Therefore, a further analysis of the SRP behaviour, and of other models that are based on more physical effects could lead to even better results and understanding of the dynamical environment,

References

Achilleas, P. (2010). Regulation of space activities in france. *National Regulation of Space Activities*, 109–122.

Baer, J., Chesley, S. R., & Milani, A. (2011). Development of an observational error model. *Icarus*, *212*(1), 438–447.

Baker-McEvilly, B., Bhadauria, S., Canales, D., & Frueh, C. (2024). A comprehensive review on cislunar expansion and space domain awareness. *Progress in Aerospace Sciences*, *147*, 101019.

Balster, P., Jones, G., Hofer, G., Newsom, D., & Frueh, C. (2023). Object characteristic determination using brightness measurements. *Proceedings of the Advanced Maui Optical and Space Surveillance (AMOS) Technologies Conference*, 72.

Barakat, B. F., & Kezirian, M. T. (2024). Establishing requirements for lunar and cislunar orbital debris tracking. *Journal of Space Safety Engineering*, *11*(3), 446–453.

Bonnal, C., McKnight, D., Phipps, C., Dupont, C., Missonnier, S., Lequette, L., Merle, M., & Rommelaere, S. (2020). Just in time collision avoidance–a review. *Acta Astronautica*, *170*, 637–651.

Braun, V., Lemmens, S., Reihs, B., Krag, H., & Horstmann, A. (2017). Analysis of breakup events. *Proceedings of the 7th European Conference on Space Debris*, *7*.

Byers, M., & Boley, A. (2022). Cis-lunar space and the security dilemma. *Bulletin of the Atomic Scientists*, *78*(1), 17–21.

Cannelli, S., de Veld, F., Gehlot, M., Nugent, T., & Thangavel, K. (2023). Earth's orbits as a unesco world heritage site.

Casanova, D., Petit, A., & Lemaître, A. (2015). Long-term evolution of space debris under the j 2 effect, the solar radiation pressure and the solar and lunar perturbations. *Celestial Mechanics and Dynamical Astronomy*, *123*(2), 223–238.

Celletti, A., Efthymiopoulos, C., Gachet, F., Galeş, C., & Pucacco, G. (2017). Dynamical models and the onset of chaos in space debris. *International Journal of Non-Linear Mechanics*, *90*, 147–163.

Creech, S., Guidi, J., & Elburn, D. (2022). Artemis: An overview of nasa's activities to return humans to the moon. *2022 ieee aerospace conference (aero)*, 1–7.

Denis, G., Alary, D., Pasco, X., Pisot, N., Texier, D., & Toulza, S. (2020). From new space to big space: How commercial space dream is becoming a reality. *Acta Astronautica*, *166*, 431–443.

Dirkx, D. (2025).

Dirkx, D., Fayolle, M. [Marie], Garrett, G., Avillez, M., Cowan, K., Cowan, S., Encarnacao, J., Lombrana, C. F., Gaffarel, J., Hener, J., et al. (2022). The open-source astrodynamics tudatpy software–overview for planetary mission design and science analysis. *EPSC2022*, (EPSC2022-253).

Dirkx, D., Mooij, E., & Root, B. (2019). Propagation and estimation of the dynamical behaviour of gravitationally interacting rigid bodies. *Astrophysics and Space Science*, *364*, 1–22.

Dural, S., Tugcular, U., & Daser, B. (2021). General collision avoidance maneuver decision algorithm. *8th European Conference on Space Debris*, 20–23.

ESA. (2019). Space safety: Esa's planetary defence office [https://www.esa.int/Space_Safety/Space_Safety_ESA_s_Planetary_Defence_Office [Consulted on : 22/10/2024]].

Farnocchia, D., Chesley, S., Chamberlin, A., & Tholen, D. (2015). Star catalog position and proper motion corrections in asteroid astrometry. *Icarus*, *245*, 94–111.

Fayolle, M., Dirkx, D., Lainey, V., Gurvits, L., & Visser, P. (2022). Decoupled and coupled moons' ephemerides estimation strategies application to the juice mission. *Planetary and Space Science*, *219*, 105531.

Fehlberg, E. (1968). *Classical fifth-, sixth-, seventh-, and eighth-order runge-kutta formulas with stepsize control* (tech. rep.). NASA.

Frueh, C., Howell, K., DeMars, K. J., & Bhadauria, S. (2021). Cislunar space situational awareness. *31st AIAA/AAS Space Flight Mechanics Meeting*, 6–7.

Gasparini, G., & Miranda, V. (2010). Space situational awareness: An overview. In W. Rathgeber, K.-U. Schrogl, & R. A. Williamson (Eds.), *The fair and responsible use of space: An international perspective* (pp. 73–87). Springer Vienna. https://doi.org/10.1007/978-3-211-99653-9_7

Godard, B., Budnik, F., Bellei, G., Muñoz, P., & Morley, T. (2017). Multi-arc orbit determination to determine rosetta trajectory and 67p physical parameters. *Proceedings 26th International Symposium on Space Flight Dynamics–26th ISSFD, Matsuyama, Japan*.

Goswami, J. (2010). An overview of the chandrayaan-1 mission. *41st Annual Lunar and Planetary Science Conference*, (1533), 1591.

Gray, B. (2022). Find_orb: Orbit determination from observations. *Astrophysics Source Code Library*, ascl–2202.

Guardabasso, P., Skoulidou, D. K., Bucci, L., Letizia, F., Lemmens, S., Ansart, M., Roser, X., Lizy-Destrez, S., & Casalis, G. (2023). Analysis of accidental spacecraft break-up events in cislunar space. *Advances in Space Research*, *72*(5), 1550–1569.

Guo, R., Hu, X., Tang, B., Huang, Y., Liu, L., Cheng, L., & He, F. (2010). Precise orbit determination for geostationary satellites with multiple tracking techniques. *Chinese Science Bulletin*, *55*, 687–692.

Hobbs, S., Stansbery, G., & de Carvalho, T. M. (2019). Chapter 30 - space waste. In T. M. Letcher & D. A. Vallero (Eds.), *Waste (second edition)* (Second Edition, pp. 567–583). Academic Press. https://doi.org/https://doi.org/10.1016/B978-0-12-815060-3.00030-X

Horwood, J. T., & Poore, A. B. (2014). Gauss von mises distribution for improved uncertainty realism in space situational awareness. *SIAM/ASA Journal on uncertainty Quantification*, *2*(1), 276–304.

Hwang, H., Park, S.-Y., Lee, E., et al. (2019). Angles-only initial orbit determination of low earth orbit (leo) satellites using real observational data. *Journal of Astronomy and Space Sciences*, *36*(3), 187–197.

Jah, M., & Madler, R. A. (2007). Satellite characterization: Angles and light curve data fusion for spacecraft state and parameter estimation. *Proceedings of the advanced Maui optical and space surveillance technologies conference*, *49*.

Kessler, D. J., Johnson, N. L., Liou, J., & Matney, M. (2010). The kessler syndrome: Implications to future space operations. *Advances in the Astronautical Sciences*, *137*(8), 2010.

Kjeldsen, H., & Frandsen, S. (1992). High-precision time-resolved ccd photometry. *Publications of the Astronomical Society of the Pacific*, *104*(676), 413.

Klinkrad, H. (2006). *Space debris: Models and risk analysis*. Springer Science & Business Media.

Lari, G., & Milani, A. (2019). Chaotic orbit determination in the context of the juice mission. *Planetary and Space Science*, *176*, 104679.

Li, C., Liu, J., Ren, X., Zuo, W., Tan, X., Wen, W., Li, H., Mu, L., Su, Y., Zhang, H., et al. (2015). The chang'e 3 mission overview. *Space Science Reviews*, *190*, 85–101.

Luo, Y.-z., & Yang, Z. (2017). A review of uncertainty propagation in orbital mechanics. *Progress in Aerospace Sciences*, *89*, 23–39.

McDowell, J. C. (2020a). *General catalog of artificial space objects, release 1.7.3*. Retrieved July 14, 2025, from https://planet4589.org/space/gcat

McDowell, J. C. (2020b). The low earth orbit satellite population and impacts of the spacex starlink constellation. *The Astrophysical Journal Letters*, *892*(2), L36.

McMahon, J. W., & Scheeres, D. J. (2015). Improving space object catalog maintenance through advances in solar radiation pressure modeling. *Journal of Guidance, Control, and Dynamics*, *38*(8), 1366–1381.

Montenbruck, O., & Gill, E. (2013). Satellite orbits.

Parisi, M., Finocchiaro, S., Iess, L., et al. (2012). Multi-arc and batch-sequential filters for the orbit determination of esa's juice mission. *23rd International Symposium on Space Flight Dynamics*.

Schaeperkoetter, A. V. (2012). *A comprehensive comparison between angles-only initial orbit determination techniques* [Doctoral dissertation].

Stiller, D. (2023). Short-term orbital effects of radiation pressure on the lunar reconnaissance orbiter.

Vallado, D. A. (2001). *Fundamentals of astrodynamics and applications* (Vol. 12). Springer Science & Business Media.

Vereš, P., Farnocchia, D., Chesley, S. R., & Chamberlin, A. B. (2017). Statistical analysis of astrometric errors for the most productive asteroid surveys. *Icarus*, *296*, 139–149.

Wakker, K. F. (2015). Fundamentals of astrodynamics. *TU Delft Repository, Delft*.

Wilmer, A. P., Boone, N. R., & Bettinger, R. A. (2022). Debris propagation and spacecraft survivability assessment for catastrophic mishaps occurring in cislunar periodic orbits. *Journal of Space Safety Engineering*, *9*(2), 207–222.

Witte, D. (2024). A model framework for high-accuracy orbit determination and propagation of cislunar space debris.

Xu, L., & Ouyang, Z. (2014). Scientific progress in china's lunar exploration program. *Chin. J. Space Sci*, *34*(5), 525–534.

A

Arc overlap study

A.1. Full results of the arc overlap study

In this section, the plots for all the overlaps considered (14 for Chang'e 2 and 19 for Chang'e 3) are shown. The plots shown here are the magnitude of the position difference and the evolution of the instantaneous delay over the arc overlap.

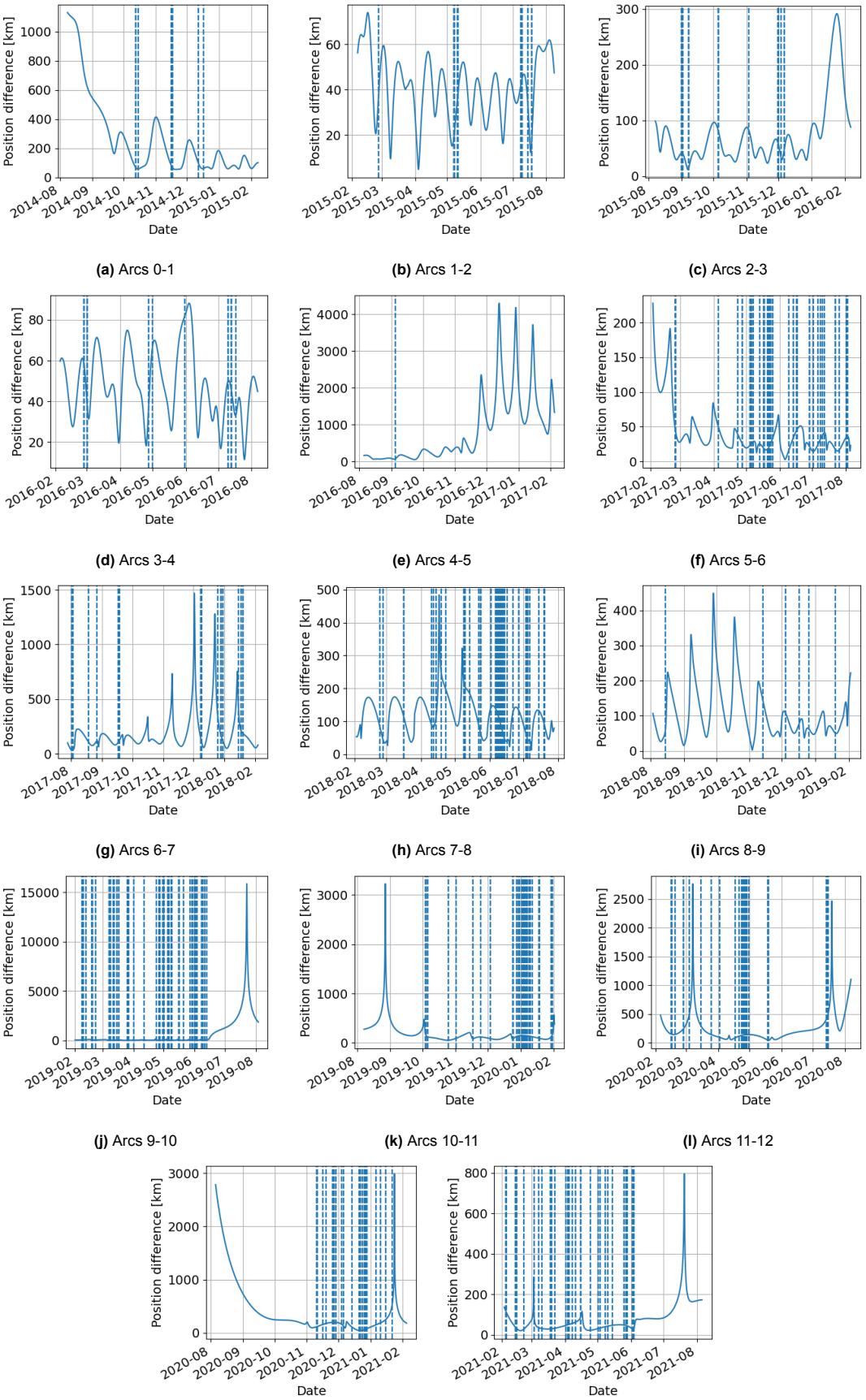

(a) Arcs 0-1 **(b)** Arcs 1-2 **(c)** Arcs 2-3

(d) Arcs 3-4 **(e)** Arcs 4-5 **(f)** Arcs 5-6

(g) Arcs 6-7 **(h)** Arcs 7-8 **(i)** Arcs 8-9

(j) Arcs 9-10 **(k)** Arcs 10-11 **(l)** Arcs 11-12

(m) Arcs 12-13 **(n)** Arcs 13-14

Figure A.1: Position difference magnitude for the Chang'e 2 upper stage

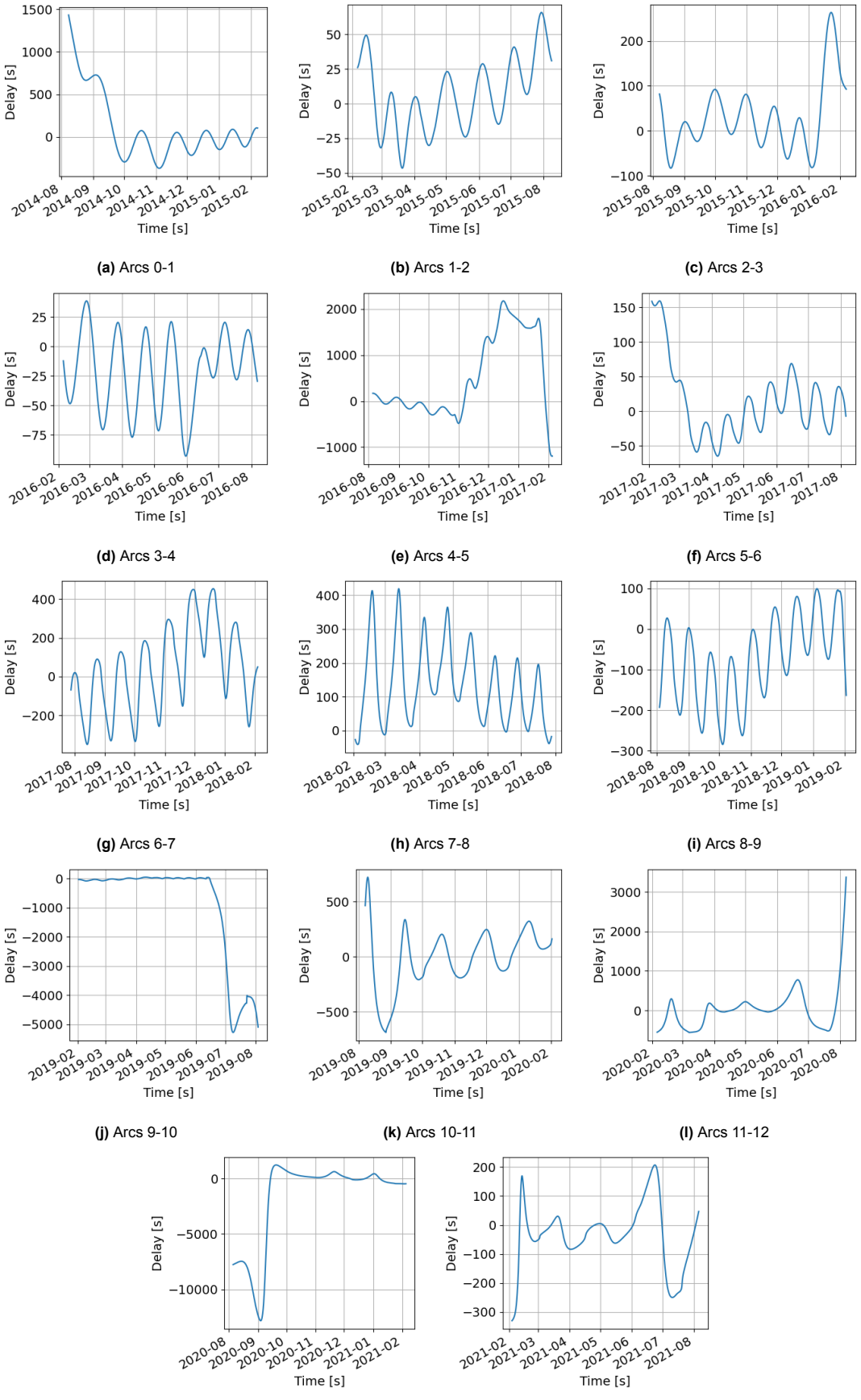

(a) Arcs 0-1 **(b)** Arcs 1-2 **(c)** Arcs 2-3

(d) Arcs 3-4 **(e)** Arcs 4-5 **(f)** Arcs 5-6

(g) Arcs 6-7 **(h)** Arcs 7-8 **(i)** Arcs 8-9

(j) Arcs 9-10 **(k)** Arcs 10-11 **(l)** Arcs 11-12

(m) Arcs 12-13 **(n)** Arcs 13-14

Figure A.2: Instantaneous delay for the Chang'e 2 upper stage

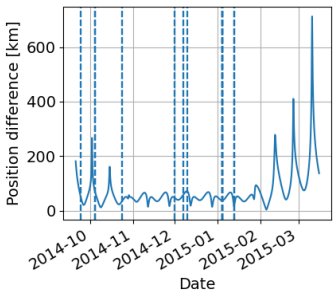

(a) Arcs 0-1

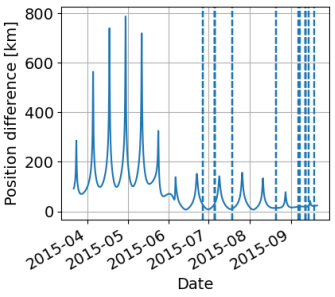

(b) Arcs 1-2

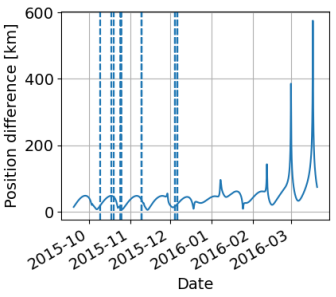

(c) Arcs 2-3

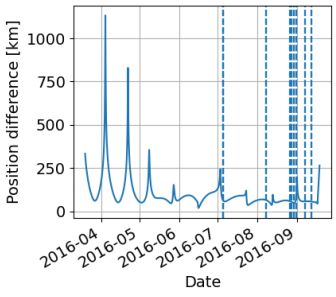

(d) Arcs 3-4

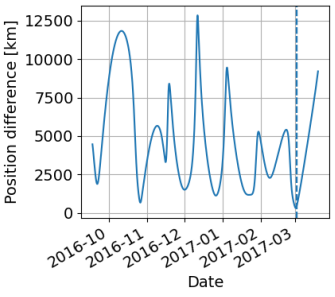

(e) Arcs 4-5

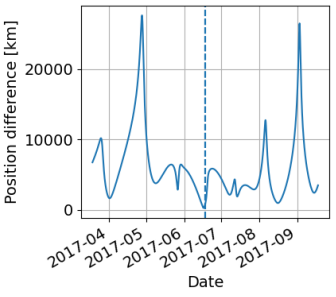

(f) Arcs 5-6

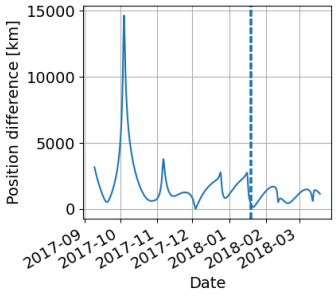

(g) Arcs 6-7

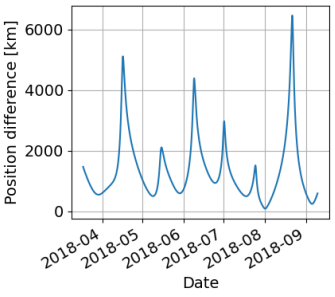

(h) Arcs 7-8

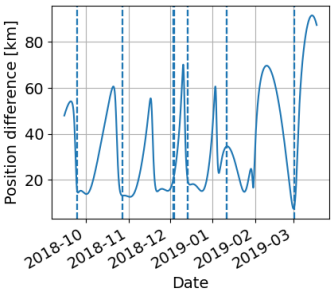

(i) Arcs 8-9

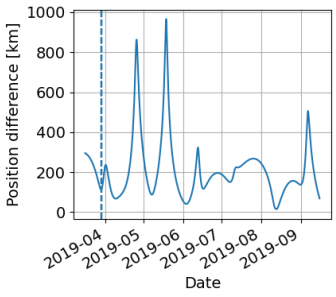

(j) Arcs 9-10

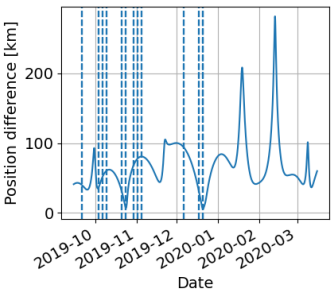

(k) Arcs 10-11

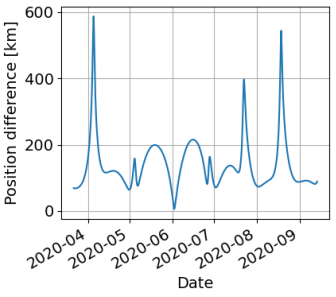

(l) Arcs 11-12

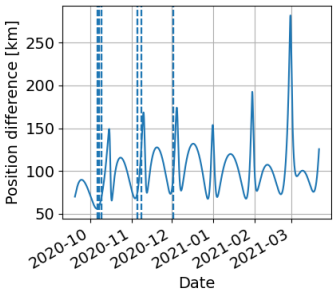

(m) Arcs 12-13

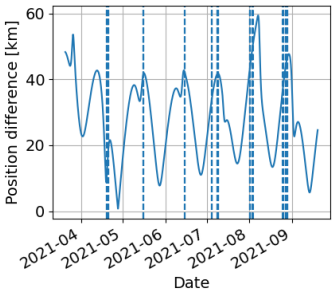

(n) Arcs 13-14

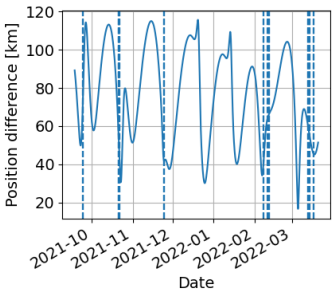

(o) Arcs 14-15

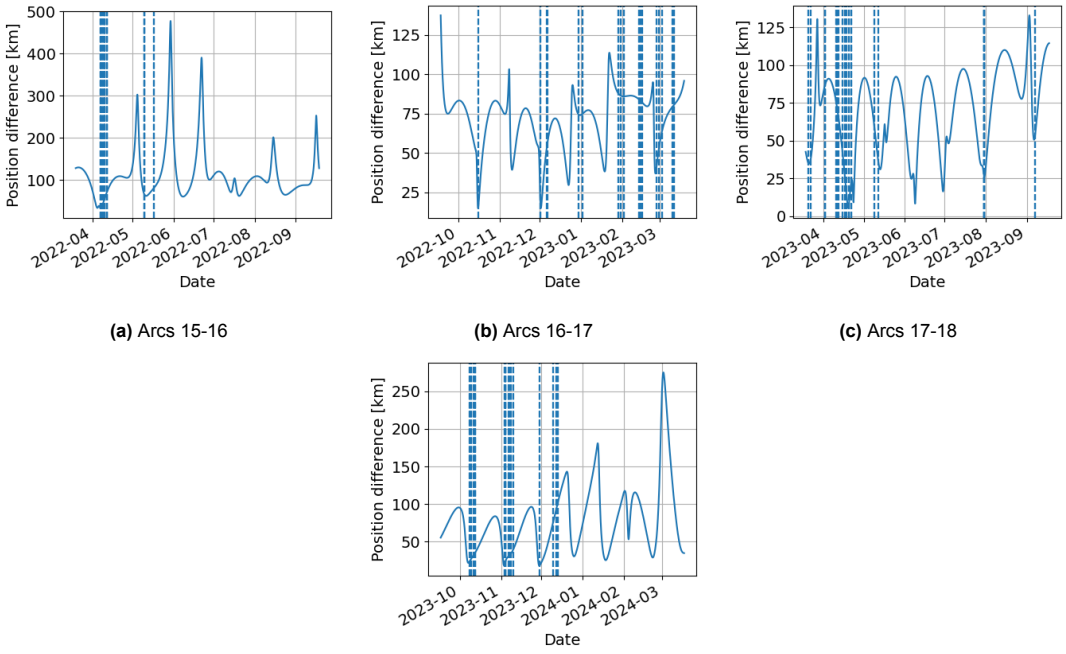

(a) Arcs 15-16

(b) Arcs 16-17

(c) Arcs 17-18

(d) Arcs 18-19

Figure A.4: Position difference magnitude for the Chang'e 3 upper stage

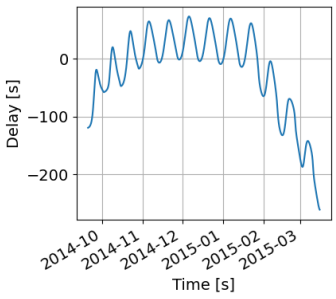

(a) Arcs 0-1

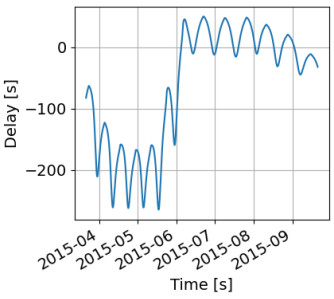

(b) Arcs 1-2

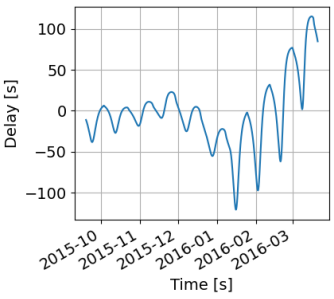

(c) Arcs 2-3

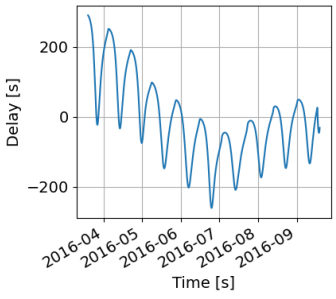

(d) Arcs 3-4

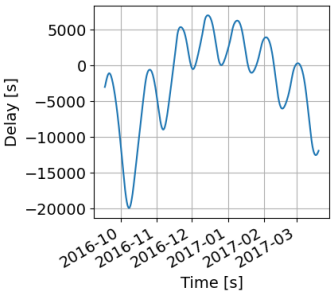

(e) Arcs 4-5

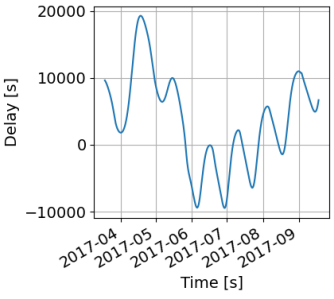

(f) Arcs 5-6

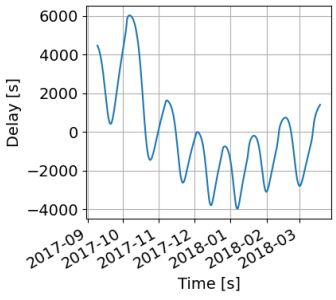

(g) Arcs 6-7

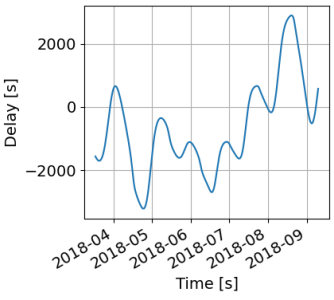

(h) Arcs 7-8

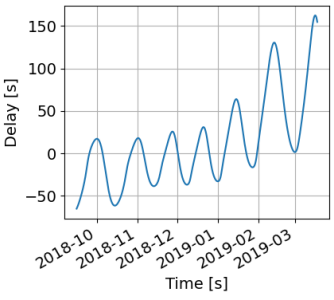

(i) Arcs 8-9

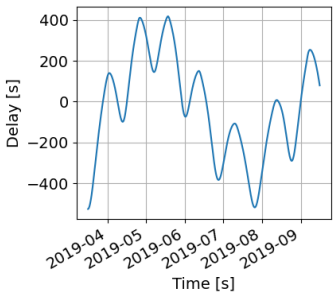

(j) Arcs 9-10

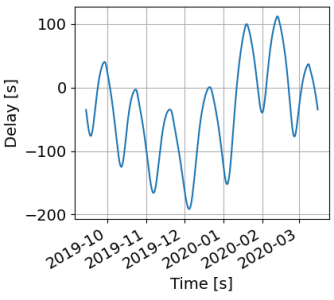

(k) Arcs 10-11

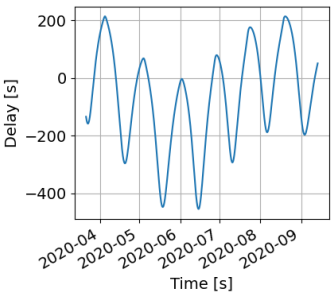

(l) Arcs 11-12

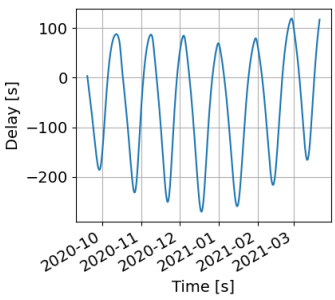

(m) Arcs 12-13

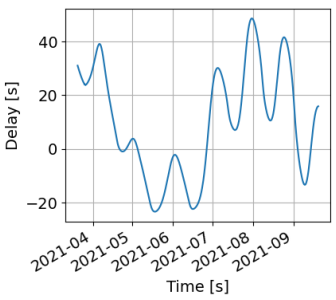

(n) Arcs 13-14

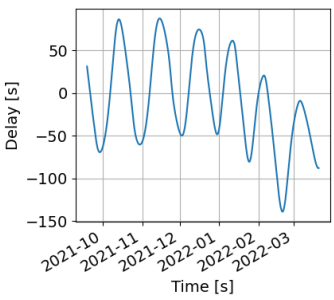

(o) Arcs 14-15

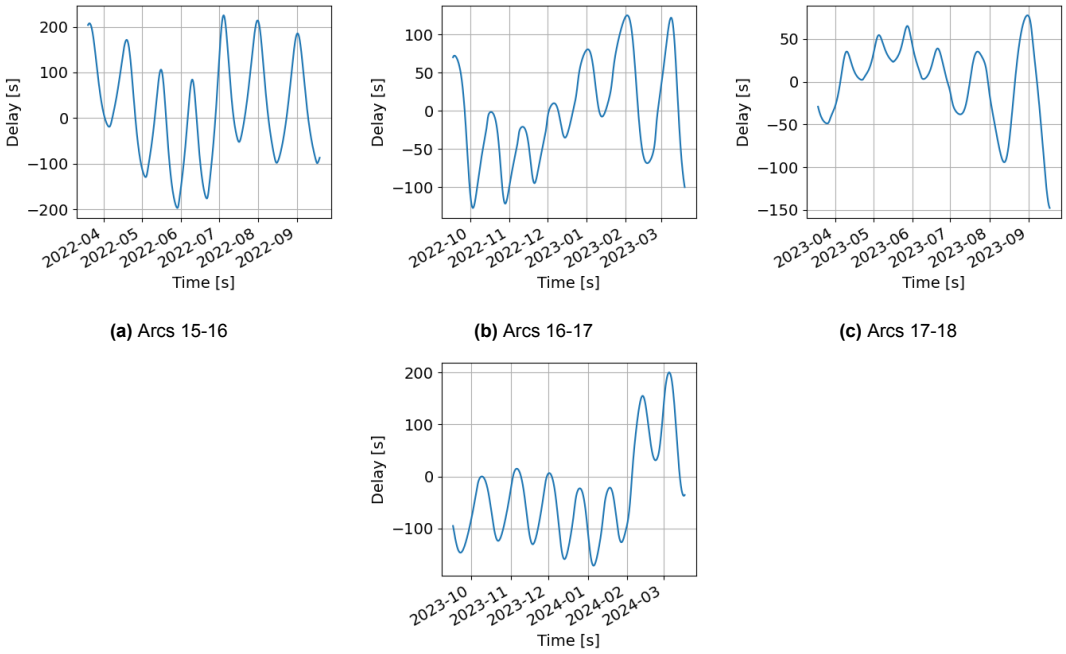

(a) Arcs 15-16

(b) Arcs 16-17

(c) Arcs 17-18

(d) Arcs 18-19

Figure A.6: Instantaneous delay for the Chang'e 3 upper stage

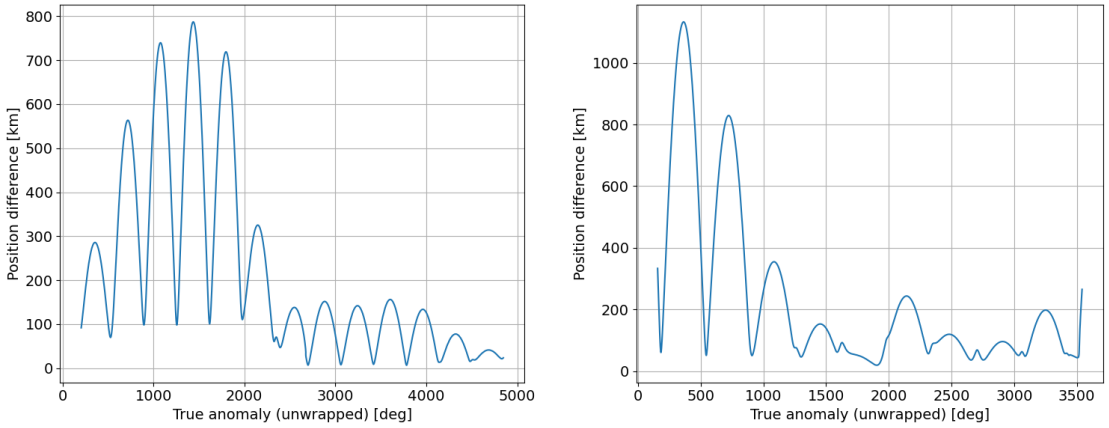

(a) Arcs 1-2 **(b)** Arcs 3-4

Figure A.7: Magnitude of the position difference between arcs 0 and 1, plotted vs the true anomaly as computed from the latter arc

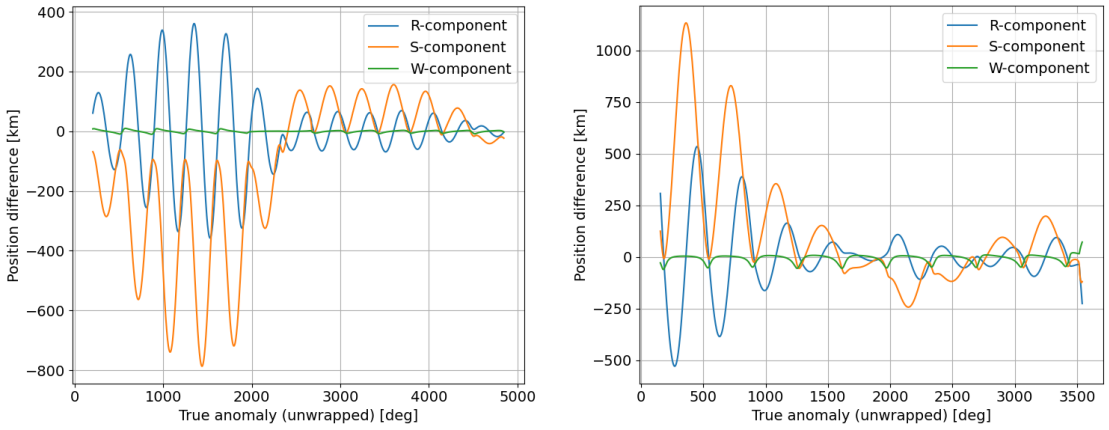

(a) Arcs 1-2 **(b)** Arcs 3-4

Figure A.8: RSW decomposition of the position difference, plotted vs the true anomaly as computed from the latter arc

A.2. True anomaly as a variable

It has been established in section 4.2 that the behaviour of the position difference is well explained by an instantaneous delay between two estimated trajectories. This indicates that the reason the position difference grows larger near periapsis is due to a higher estimated velocity. An alternate option for plotting the position difference can thus be used, by replacing the x-axis with the true anomaly of the estimated position.

This new visualisation is applied to the magnitude of the position difference in Figure A.7, the RSW decomposition of the difference (using the RSW frame of the second trajectory) in Figure A.8 and the TNW decomposition of the difference (using the TNW frame of the second trajectory) in Figure A.9

In these plots it can be seen that the spikes and discontinuities are completely smoothed when plotted with respect to the true anomaly instead of the time. In particular, the TNW plot now exhibits sharper behaviour in the ”dips” between the spikes, i.e. at apoapsis. This is due to the same ”time dilation” phenomenon that rendered the spikes more smooth near periapsis. Indeed, the reason for the spikes to be so concentrated was the fact that over the same period of time, the true anomaly varies much faster near the apoapsis. In a similar way, over a similar difference in true anomaly, time goes by much faster near apoapsis. The RSW plot, however, gives a different insight for this phenomenon, that will be discussed in the following section.

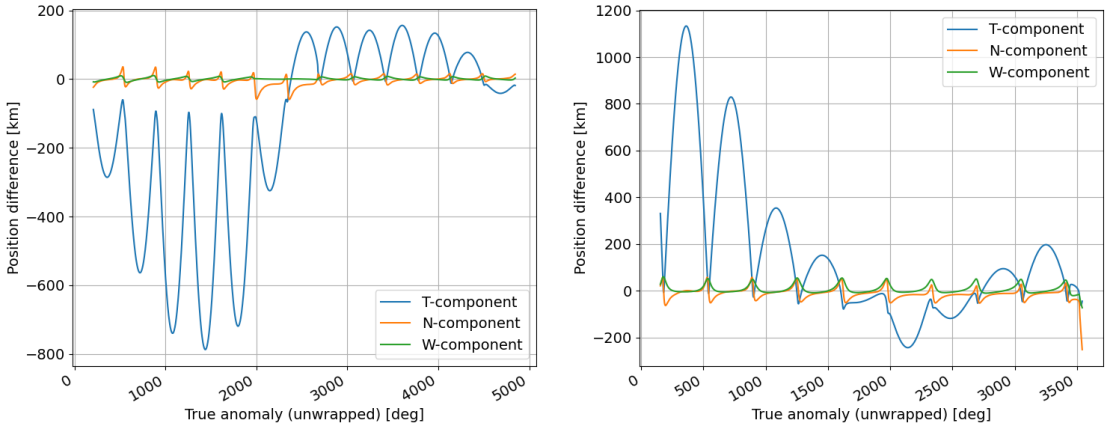

(a) Arcs 1-2

(b) Arcs 3-4

Figure A.9: TNW decomposition of the position difference, plotted vs the true anomaly as computed from the latter arc

A.3. RSW frame results

In the RSW decomposition of the overlap position difference, seen in Figure 4.8, the spikes are mostly present in the R- and S-components, with the S-component presenting the same type of spikes that are seen in the magnitude of the position difference, whereas the radial component shows very sharp variations, almost looking like discontinuities. On the W-component it can be noted that the differences are much smaller and that the curve is significantly smoother than the two other ones, thus indicating that the position difference between the two estimated trajectories is mostly contained in the plane of the orbit, and that the ”spiky” behaviour of this difference is not restricted to only one of the other components.

When plotting the RSW decomposition of the position difference against the true anomaly in Figure A.8, the R and S plots appear to be very smooth, and resemble sine waves, comprised inside an envelope. This provides more insight for the other plots, as it shows two smooth behaviour in two different directions. When those two sine waves are squared and added, then their combination leads to the apparition of the sharper dips in the TNW and magnitude plots. However, there is no easy way of analysing the behaviour of oscillations along those two directions, especially since they are not aligned with the more physically relevant in-track and cross-track directions.

This behaviour can still be seen as an indication that the position difference can be described through analytical equations. Indeed, in a simpler context the equations for the difference in position or the delay can be derived, such as the Clohessy-Wiltshire equations found in [Wakker 2015] for two objects in circular orbits. Those equations give a very similar result to what was obtained in the RSW frame in Figure A.8, with sinusoidal oscillations in two different directions, and thus this situation could potentially be well-explained by such formulas. However, the complexity of the environment for this study makes it significantly harder to derive even an approximation of a mathematical expression that would explain all the effects that are visible here.

A.4. TNW frame analysis

Knowing where the difference between the two estimated trajectories comes from and the mechanism of how it leads to such a behaviour for the position difference is already a very satisfactory result, but it can be improved even further, namely by investigating the reason why two estimations that share half their data points seem to frequently exhibit this type of difference.

In order to perform this investigation, the plot from Figure A.9 is used as a basis. Indeed, this plot shows that most of the position difference is found in the Tangential direction. One possible explanation for the two trajectories being offset specifically in this direction could be that the observations, being two-dimensional, do not allow for a proper sampling of this specific direction. At first glance this seems counter-intuitive, as the sampling is done from the Earth, meaning that the T- and W- directions

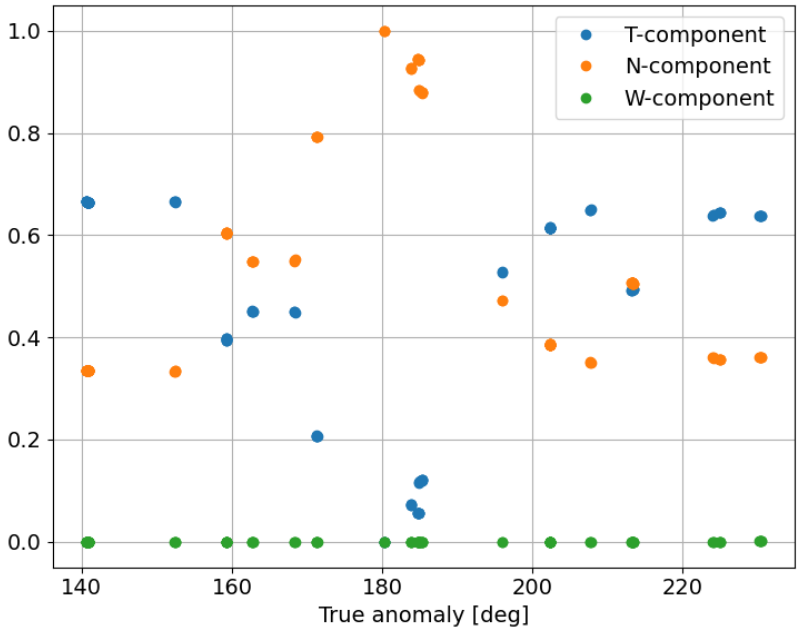

Figure A.10: Unsampled portion of the TNW frame during arc 1

are perfectly sampled while the Normal one is where all the uncertainty is concentrated. However, this reasoning would be more adequate when using the RSW, where the Radial component always points from the Earth to the object. In the case of the TNW frame, and considering the highly elliptical nature of the orbits considered in the present work, the Tangential component can have a non-negligible alignment with the line-of-sight from the ground station, especially if the observations are performed far from the periapsis and the apoapsis. In order to check this theory, the unsampled portion of the TNW frame is computed for each observation.

This computation is done by retrieving the Cartesian position of the ground station that performed the observation, subtracting it from the position of the space object. After dividing the resulting vector by its norm the unit vector that is obtained gives the direction of the space object as seen from the ground station, which is the unsampled direction. The TNW frame is then converted into Cartesian coordinates using the rotation matrix. After that, the dot product of each of the T, N and W unit vectors with the unsampled direction vector is computed, and the result is squared. The reason for squaring the dot products is the fact that projecting a unit vector onto another one gives the cosine of their angle. However, the sum of those cosines is not constant, whereas the sum of the squares of those cosines adds up to 1 regardless of the orientation of the vectors. Therefore, projecting the unsampled direction unit vector on the TNW frame and squaring the results gives the proportion of this vector in each of the three directions. The resulting decomposition of the unsampled direction during the overlap between arcs 1-2 is then plotted versus the true anomaly of the estimated position, and the results are shown in Figure A.10

In this figure, it can first be observed that a significant part of the observations (more than 50%) happen with a line-of-sight oriented so that the unsampled direction is mostly along the T direction. This observation could provide an explanation to why the two estimated trajectories are able to differ mostly along this direction. Moreover, it can be seen that those observations are close to the apoapsis (between 140 and 220°). This concentration can also explain why the position difference takes the form of a delay. Indeed, if all the observations are located at (roughly) the same point on the trajectory its shape is still obtainable by the estimator. This is because the semi-major axis for instance can be found from the orbital period using Kepler's third law, and the observations of an arc over a sufficient number of revolutions allows the estimator to constrain the trajectory to its actual shape. However, the unsampled portion of the T component means that a small error can be made regarding the position of the space object along this orbit. This error, which depends on the specific observation set, can be considered

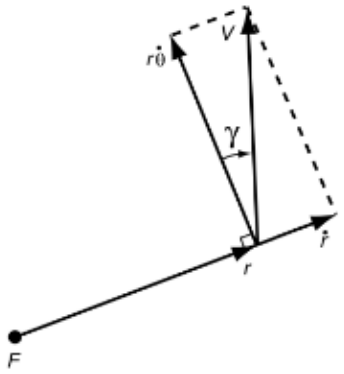

Figure A.11: Flight path angle [Wakker 2015]

random, and thus the difference between two consecutive estimations also presents a random error along the tangential component.

In addition to those conclusions, a validation process is performed to ensure that the calculations of the unsampled direction are done properly. To do that, a theoretical formula giving the portion of each of the component that is unsampled as a function of the true anomaly is derived. For this analytical formula to exist, two assumptions are made. The first one is that the orbit is an ellipse, as this allows to use the existing formulas for the flight path angle to obtain the angle between the T component and the position vector (going from the centre of the Earth to the centre of mass of the object. The second assumption is that the ground stations are all located at the centre of the Earth, thus allowing to use the position vector to obtain the line of sight. Having made those two assumptions, the flight path angle γ as defined in [Wakker 2015] and shown in Figure A.11 can be computed.

The expression for its value as a function of the true anomaly can be found in [Wakker 2015] in the form:

$$\tan\gamma = \frac{e\sin\theta}{1+e\cos\theta} \tag{A.1}$$

This equation can be inverted to obtain

$$\gamma = \arctan\left(\frac{e\sin\theta}{1+e\cos\theta}\right) \tag{A.2}$$

And finally the unsampled portion of the T component, defined as the square of its projection on the unit vector of the line-of-sight, is given by:

$$\epsilon_T(\theta) = \sin^2\gamma = \sin^2\left(\arctan\left(\frac{e\sin\theta}{1+e\cos\theta}\right)\right) \tag{A.3}$$

In this expression, the eccentricity of the orbit is the only parameter that is left to determine, which is logical as a perfectly circular orbit would have the tangential component of the TNW frame be at all times perpendicular to the position unit vector, thus being always perfectly sampled. Since the eccentricity of the trajectory that is the focus of the present study is not constant in time, it is chosen to plot $\epsilon_T(\theta)$ for different values of e, thus allowing to see the variation in the profiles that comes with a varying eccentricity. The resulting plot for the T component can be seen in Figure A.12. The R- and W-components are not shown as the W would be a flat line with a zero value, while the unsampled part of the R component can be expressed as:

$$\epsilon_R(\theta) = 1 - \epsilon_T(\theta) \tag{A.4}$$

thus being directly obtained by flipping the curve for ϵ_T along a horizontal axis.

The first observation that can be made on this plot is the fact that, as expected, the lowest eccentricities lead to lower unsampled portions of the T component. Another expected behaviour is the fact that ϵ_T increases as the true anomaly gets away from 0°, and then gets smaller again when getting close to

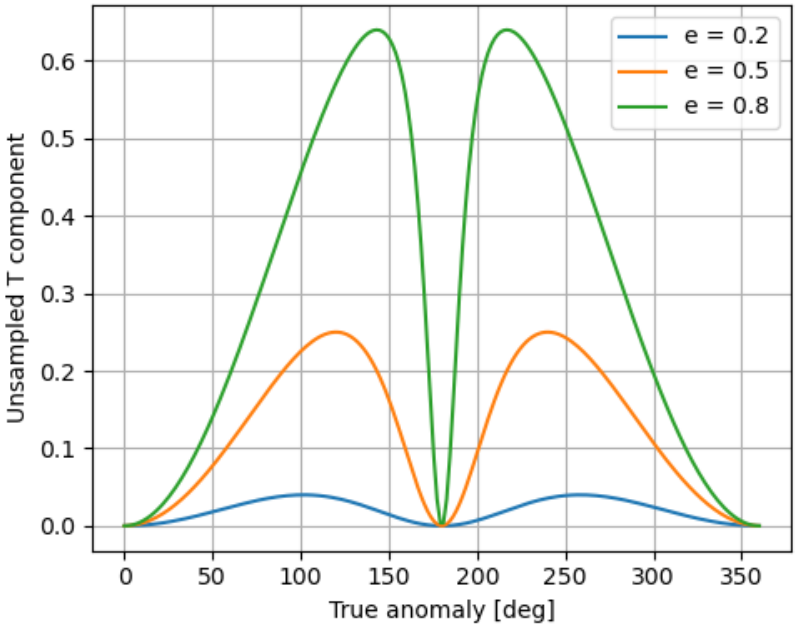

Figure A.12: Theoretical unsampled portion of the T component for different values of the eccentricity

apoapsis at 180°. One additional noteworthy observation is the fact that the width of the gap near 180° is getting lower as the eccentricity of the orbit gets bigger, meaning that more eccentric trajectories not only have an overall larger portion of the T component that is unsampled by the two-dimensional observations, but also that the region where it is properly sampled gets narrower.

Comparing this theoretical plot to the one obtained with the real observation and estimation data in Figure A.10 gives a very good match, which confirms the validity of the analysis

The two assumptions that were made to obtain the theoretical plot make it not directly useful to draw conclusions on the origin of the delay, but it can still be used to validate the way the real observation plot has been made.

Once again, as the velocities for the two virtual objects are not necessarily the same, the one for the second arc (arc 2) is used to compute the delay, under the assumption that the differences between the two velocities are close enough to cause only a minor variation in the delay. This assumption was justified earlier by arguing that a small relative difference in position led to a small relative difference in the reference frames and the position magnitude. Those arguments were very direct, as both the reference frames and the position magnitude are directly related to the position. This is not the case for the velocity, which is only indirectly related to the position through the conservation of energy principle. Therefore, it is also relevant to check that the choice of using the velocity of one arc does not considerably change the results. In order to verify this assumption, the delay is computed in a second manner, using the TNW position difference computed from the arc 2 frame, but with the velocity extracted from arc 1:

$$\Delta t_{inst,bis}(\theta) = \frac{x_{T,2}(\theta)}{v_1(\theta)} \tag{A.5}$$

Although this calculation does not correspond directly to a physical phenomenon, it is helpful to isolate the effect of using one velocity instead of the other. The two versions of the delay are then subtracted to one another, and the delay difference $\Delta_{delay}(\theta) = \Delta t_{inst}(\theta) - \Delta t_{inst,bis}(\theta)$ is plotted against the true anomaly in Figure A.13.

This plot confirms that using the velocity of arc 2 as an approximation leads to at most 4 seconds of error in the instantaneous delay computation, which represents less than 1% of the instantaneous delay, as can be seen in the plot on the right.

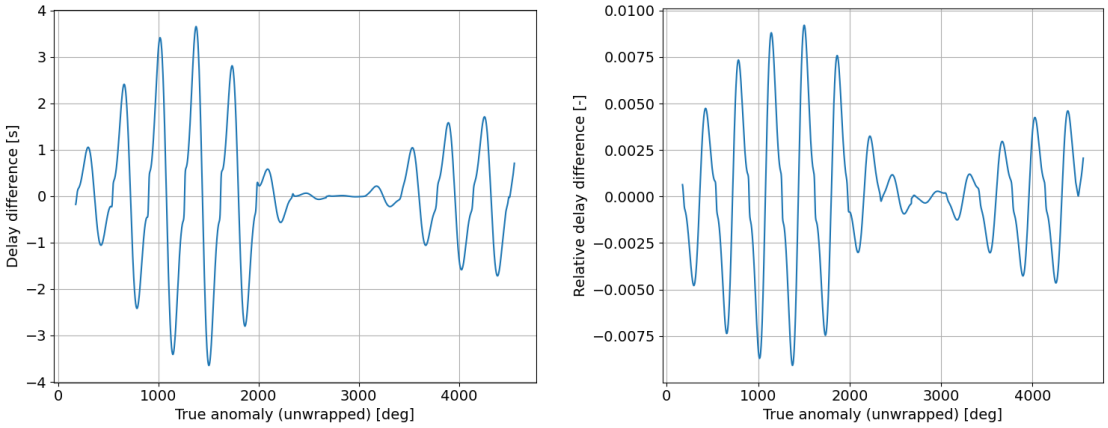

(a) Absolute difference

(b) Relative difference

Figure A.13: Difference in the two instantaneous delay computations for the overlap between arcs 1 and 2

In conclusion, the major part of the position difference between the two virtual objects estimated from two consecutive arcs can be assigned mostly to the tangential direction, i.e. alongside the velocity. This in turn can be converted into an instantaneous delay, thus meaning that the main difference between the two estimated trajectories is a time difference rather than a difference in the shape of the orbit. This is a relevant information for real-life situations as it implies that the uncertainty on the position of the space object is mostly on where it lies on the orbit rather than on the characteristics of the orbit itself. This means that for lunar space mission, even without an accurate and complete knowledge of the position of the object, planning a trajectory (or performing a manoeuvre) that stays away from the estimated orbital path should considerably decrease the risk of collision. It should however be noted that improving the accuracy of the estimation process is still a very important goal, since it is not realistic for a lunar mission to design a trajectory that would avoid all orbits of cislunar space debris, so the work cannot be considered over.

B

Residual analysis

B.1. Full results of the along-track/cross-track residuals

In this section, the plots for all the arcs considered (15 for Chang'e 2 and 20 for Chang'e 3) are shown. The plots shown here are the observation residuals using the baseline weighting setting (n° 1 of Table 3.4), and after the conversion from RA/DEC to along- and cross-track.

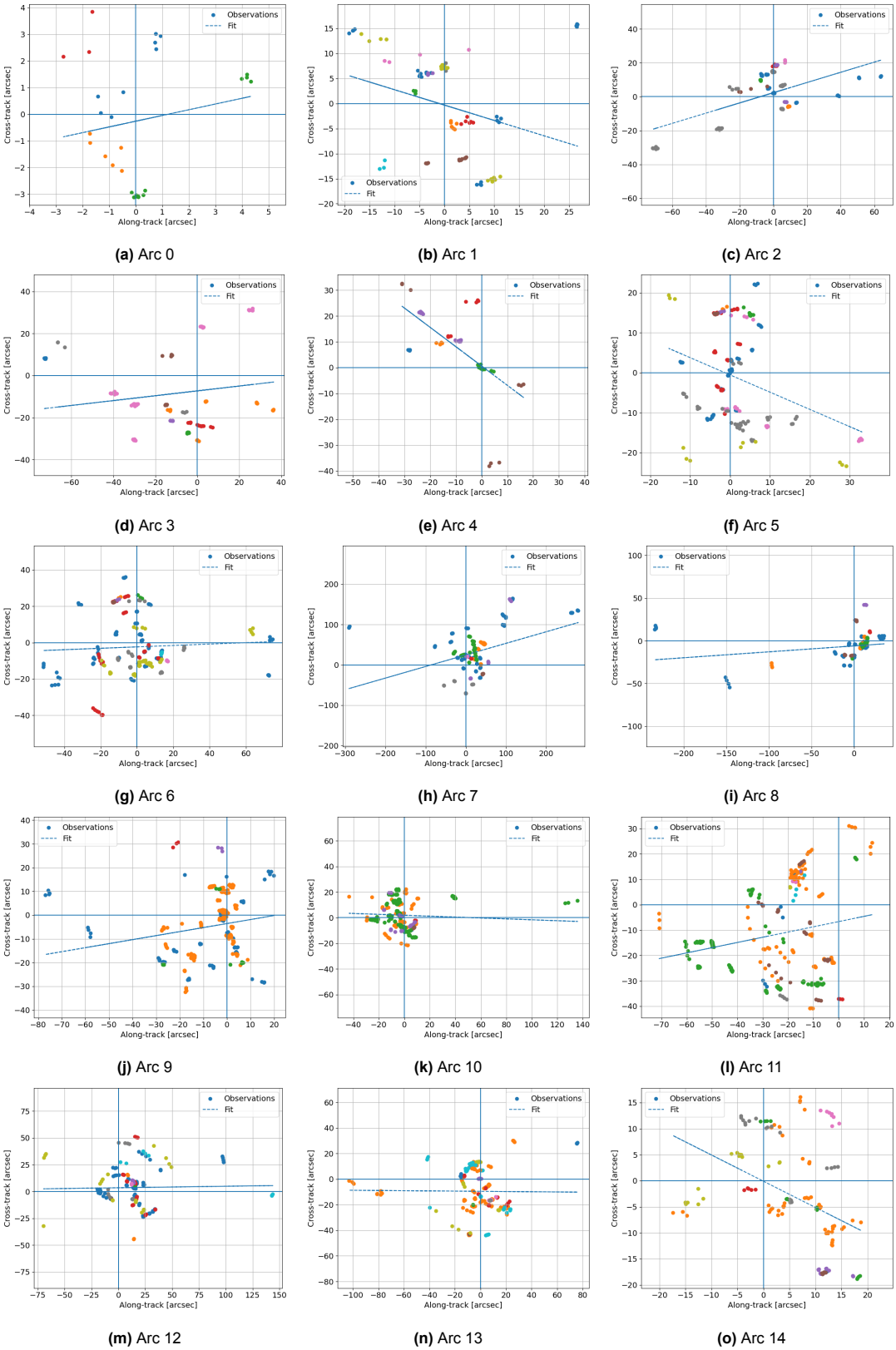

(a) Arc 0 **(b)** Arc 1 **(c)** Arc 2

(d) Arc 3 **(e)** Arc 4 **(f)** Arc 5

(g) Arc 6 **(h)** Arc 7 **(i)** Arc 8

(j) Arc 9 **(k)** Arc 10 **(l)** Arc 11

(m) Arc 12 **(n)** Arc 13 **(o)** Arc 14

Figure B.1: Residuals for the Chang'e 2 upper stage

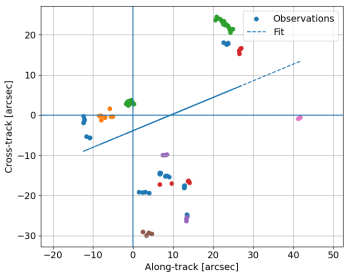

(a) Arc 0

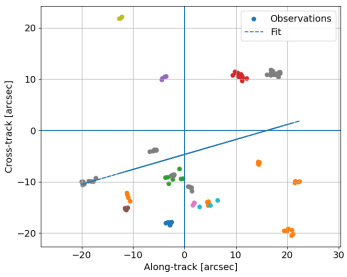

(b) Arc 1

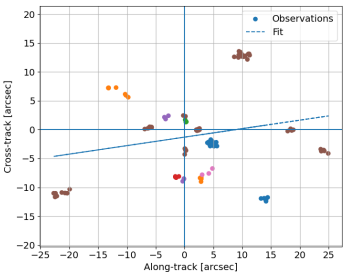

(c) Arc 2

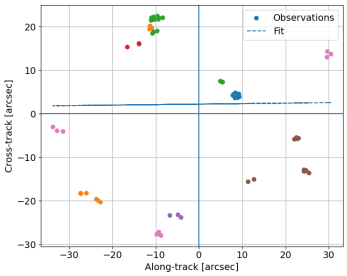

(d) Arc 3

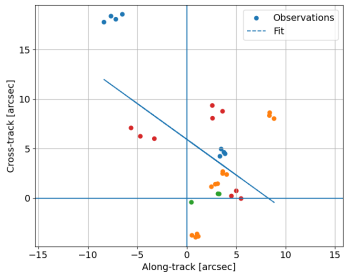

(e) Arc 4

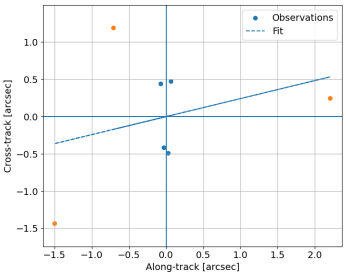

(f) Arc 5

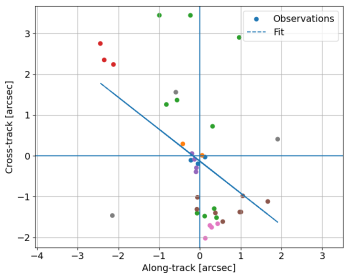

(g) Arc 6

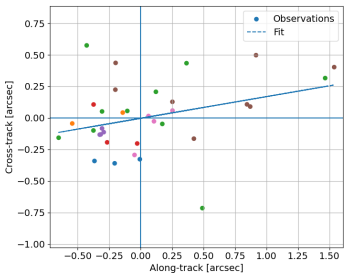

(h) Arc 7

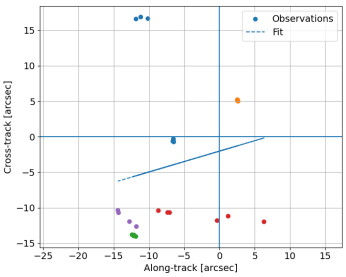

(i) Arc 8

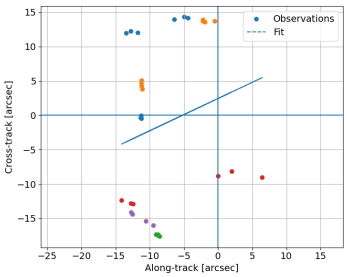

(j) Arc 9

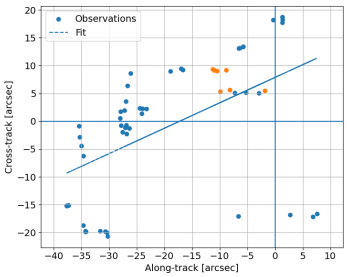

(k) Arc 10

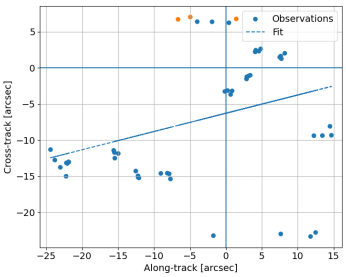

(l) Arc 11

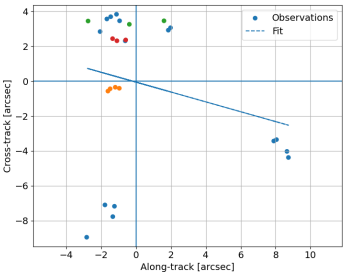

(m) Arc 12

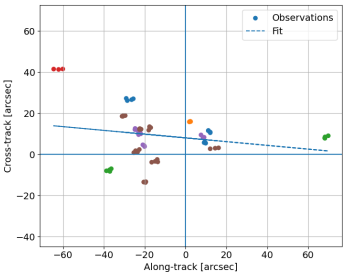

(n) Arc 13

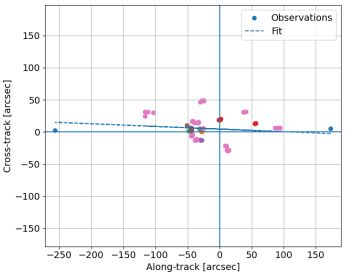

(o) Arc 14

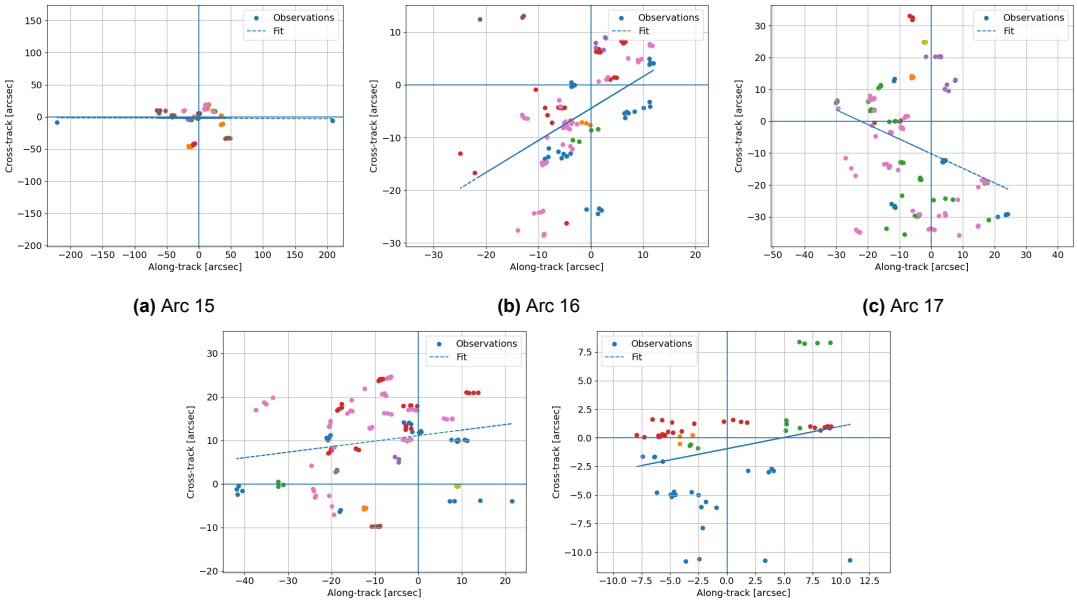

(a) Arc 15 **(b)** Arc 16 **(c)** Arc 17

(d) Arc 18 **(e)** Arc 19

Figure B.3: Residuals for the Chang'e 3 upper stage

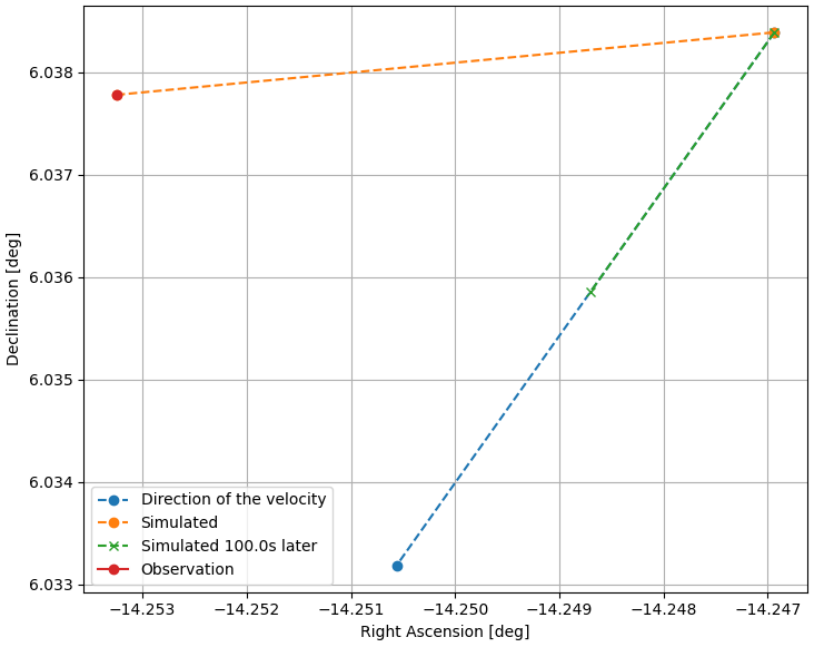

Figure B.4: Obtention of the velocity in the (α, δ) plane

B.2. Residual conversion process

The result of the process described in section 3.5 to obtain the velocity in the along-track/cross-track plane can be seen in Figure B.4, with 100s used as the delay between the two simulated observations.

On this figure, it can be noted that the amount of time chosen before the second simulated observation is adequate compared to the size of the residual. Indeed, it is of the same order of magnitude as the residual, which indicates that the potential error that could be made when assuming that the velocity is constant over this interval of time is smaller than the residual, while still being a time interval large enough to absorb any effects that would arise from numerical inacurracies when simulating the observations.

Moreover, whereas in Figure B.4 the point that was used as an origin for the direction was the simulated observation, in the analyses performed in section 4.3 it is assumed that the velocity obtained from the simulated observations can be used in place of the velocity, and thus the origin of the new reference frame is the actual observation point(s).

C

Use of the 3-constant model

C.1. Validation of the model

In order to validate the model, tests were performed on a controlled environment. This environment included the use of the Delfi-C3 satellite as an object, whose characteristics are better known, and a very simplified acceleration set, comprising only the point mass gravity of the Sun and the Earth, on top of the SRP.

The direction of the acceleration is first tested by setting the parameters to 0 except for one of them, turning off all the other accelerations and checking that the movement of the space object is in the direction that is expected. This first step ensures that the base vectors for the acceleration are properly oriented.

Knowing that the base vectors are correct, the values for the parameters then have to be validated, as far as it makes sense to test them. Indeed, since the second and third parameters do not directly match a physical phenomenon that can be modelled, finding a theoretical value is not considered. For the first one though, it is possible to match the value of the parameter to the corresponding cannonball model value, and then it is found that this parameter should have a value of: $-C_r \times A$. Therefore, it is possible to test the validity of the 3-constant model by propagating a satellite with the cannonball SRP on one side, and the 3-constant model using this theoretical value on the other side. A comparison of the two processes is shown in Figure C.1

In order to obtain this figure, the same initial state is propagated for 10 days, once with the cannonball model and then with the TCM, with a parameter set of $[-C_r A, 0, 0]$. The difference between the two positions is computed and the magnitude of this difference is plotted vs the time elapsed since the beginning of the propagation.

The result of this analysis is the fact that the position difference, while exhibiting fast oscillations, increases linearly in magnitude with the time, reaching a maximum of 1.75 m after 10 days. Such a difference is negligible compared to the other sources of error, even when considered on longer periods of time. Indeed, if this difference was increasing at the same rate over the whole 10 years of the observation window, it would still not reach 1 km of difference between the two models. Such a result indicates that the TCM is able to accurately ”imitate” the cannonball model when restricting it to a simpler version of the model.

Those first steps made sure that the new SRP model was correctly implemented for propagation purposes, but since the objective of this study is to use the new model in an estimation context, some additional tests were performed. The partials of the acceleration with respect to the state and the parameters were also needed, and their expressions were taken from [McMahon and Scheeres 2015]. In order to test the validity of those expressions, the state transition matrix (resp. the sensitivity matrix) is propagated alongside the trajectory. Then, the state is propagated again with a small initial perturbation on the different state (resp. custom parameters) values. The state transition (resp. sensitivity) matrix is then used to predict the position difference Δ_{th} between the reference trajectory and the perturbed

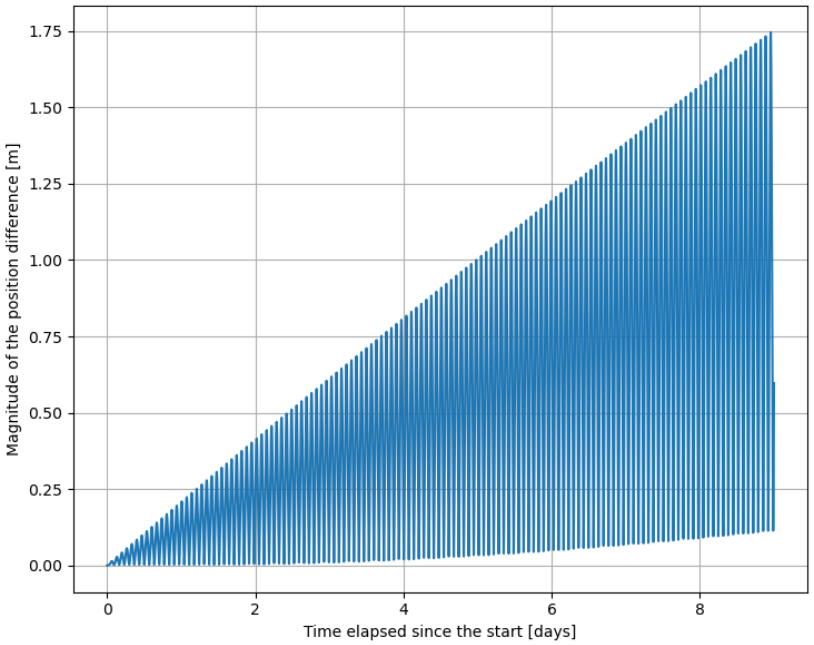

Figure C.1: Magnitude of the position difference using the cannonball radiation pressure or the TCM

one, and the actual position difference Δ_p is saved. Finally, the relative error in the position difference is computed as: $\epsilon_r = \frac{\Delta_{th} - \Delta_p}{\Delta_p}$. Due to the fact that linearization errors are always present, the relative error is not expected to be equal to zero or even in the order of magnitude of the numerical precision of the machine, but values lower that 10^{-3} are considered satisfying enough for the purposes of validating the model. Such values are attained in the current implementation, and the model is therefore validated.

C.2. A priori covariance impact

As has been described in subsection 2.4.1, the a priori covariance matrix can be used to give more weight to the initial guess. This has become highly relevant when implementing the new model for the SRP. Indeed, without using an a priori covariance matrix, the first results for the three estimated parameters can be seen in Figure C.2.

In this figure, most of the results cannot be properly interpreted because of the results of the arcs 5 through 7. In those arcs, the values of the three parameters blow up, and reach absurdly high values. In order to better visualise those results, the logarithms of the absolute values of the parameters are plotted in Figure C.3.

Once plotted in a logarithmic scale, it can be noticed that, except for the arcs 5-7, the value of the main parameter remains almost constant. A similar phenomenon can be observed, although with less stable values, for the two orthogonal parameters.

The reason for the sudden increase of more than one order of magnitude during the arcs 5-7 is likely the fact that during arc 5 there is a lunar close approach that makes the Least Squares method less effective, and the year following this close approach has only sparse data that does not constrain the trajectory enough. This leads to what is very likely to be an over-fitting of the observations inside the observation sample, at the cost of having physically absurd values for the parameters.

In order to moderate the effect of over-fitting, and considering the fact that the observations alone do not provide enough constraints to keep the estimated values of the parameters within reasonable bounds, an a priori covariance matrix is introduced. Since the initial guess for the Cartesian state (position-velocity) has not exhibited any need for constraints, and there is no way to get a proper insight on the confidence on the initial state, the a priori covariance matrix is not applied to these parameters.

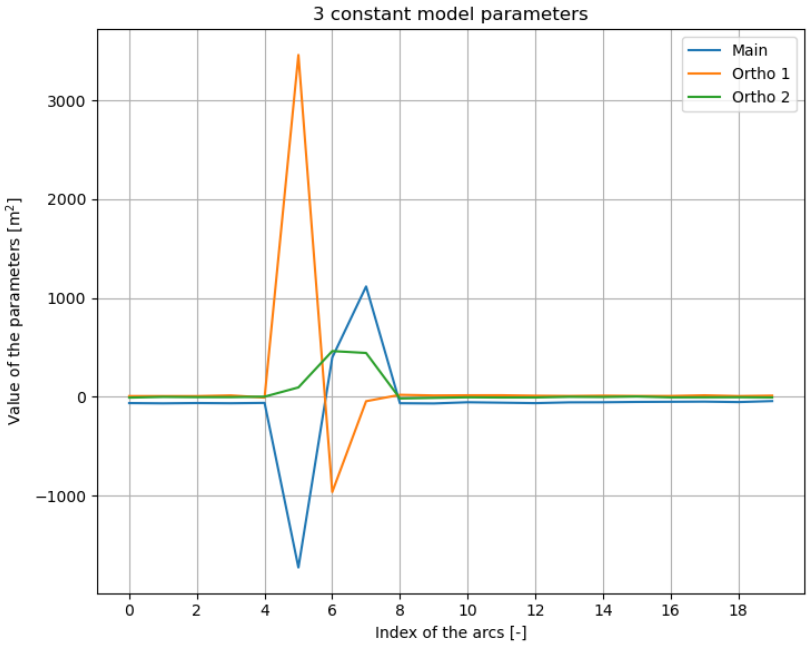

Figure C.2: Values of the estimated parameters of the TCM over the 20 arcs of the Chang'e 3 observation period

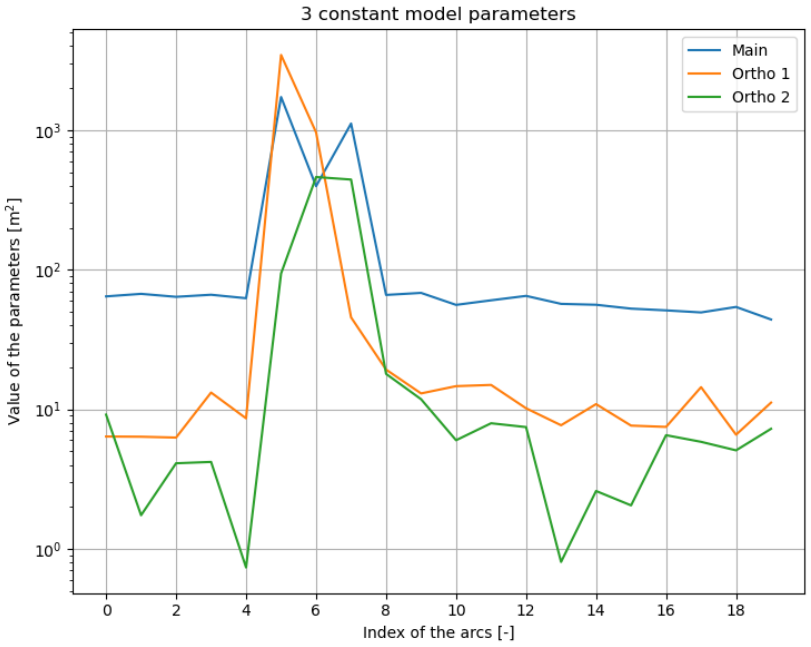

Figure C.3: Logarithmic values of the estimated parameters of the TCM over the 20 arcs of the Chang'e 3 observation period

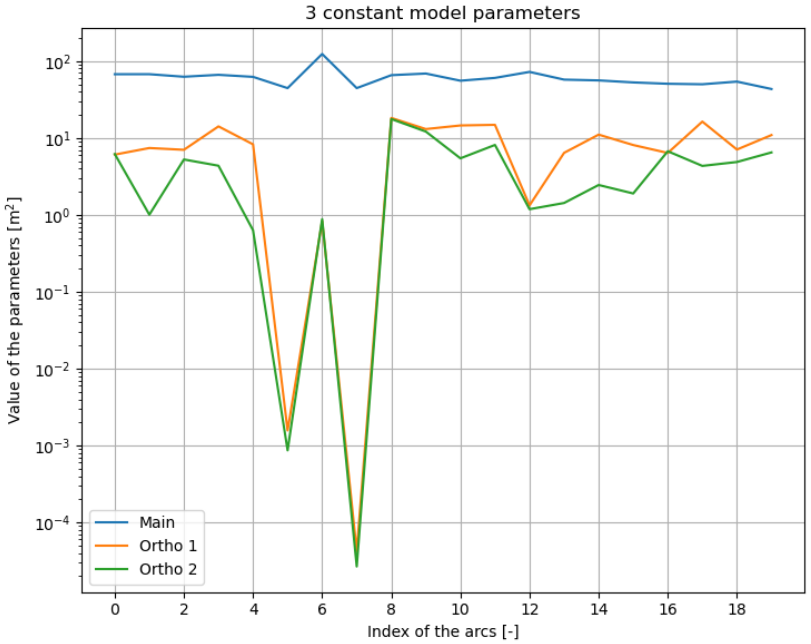

Figure C.4: Logarithmic values of the estimated parameters of the TCM after including an a priori covariance matrix

As for the parameters of the TCM, the a priori covariance matrix is used to prevent them from blowing up but should not be too restrictive and overconfident in the initial guess. As such, it is taken to be one order of magnitude lower than the typical value for the main parameter, i.e. 10, and an order of magnitude lower than that for the other two parameters, i.e. 1. Following this addition of the a priori covariance, the new logarithmic graph of the estimated parameters can be found in Figure C.4.

This time, the parameters are not blowing up to absurdly high values, but the radial (main) parameter is staying very close to all the other estimated values for the other arcs, which is coherent. The two orthogonal parameters go down to very low values (1-5 orders of magnitude lower than the estimates for the other arcs) which is an indicator that the estimation is not as stable as in the other cases. While not ideal, such low values mean that the orthogonal parameters are considered as having almost no influence on the trajectory compared to the radial one, which means that the TCM is almost identical to a cannonball model in this situation. This is preferable to having the orthogonal parameters being predominant (as in Figure C.3), because it is coherent with the physical meaning of this model. Indeed, the radiation pressure exerted by the Sun, even if it can be modelled using orthogonal components, should primarily be directed in the radial direction, pointing away from the Sun.